A Kinetic Study of Novel Gas-Phase Reaction Pathways for Pyruvic Acid and Hydrogen Halides with HO_x Radicals.

by

Jonathan Richard Church

B.A., University of Colorado Denver, 2013

A thesis submitted to the

Faculty of the Graduate School of the

University of Colorado in partial fulfillment

of the requirement for the degree of

Doctor of Philosophy

Department of Chemistry

2018

This thesis entitled:
A Kinetic Study of Novel Gas-Phase Reaction Pathways for Pyruvic Acid and Hydrogen Halides with HO_x Radicals.
written by Jonathan Richard Church
has been approved for the Department of Chemistry

_____
Prof. Rex T. Skodje

_____
Prof. Sandeep Sharma

Date_____

The final copy of this thesis has been examined by the signatories, and we find that both the content and the form meet acceptable presentation standards of scholarly work in the above mentioned discipline.

Church, Jonathan Richard (Ph.D., Chemistry)

A Kinetic Study of Novel Gas-Phase Reaction Pathways for Pyruvic Acid and Hydrogen Halides with HO_x Radicals.

Thesis directed by Prof. Rex T. Skodje

Hydroperoxy (HO_2) and hydroxyl (OH) radicals are known to play important roles in both combustion and atmospheric chemistry. Although less reactive than hydroxyl radicals, HO_2 has been found to be important to the ignition process in combustion systems and has been found in greater concentrations than that of OH in the troposphere. In this work, gas-phase reactions between HO_2 and hydrogen halides (HX, X=F, Cl, Br, I) are examined due to the catalytic effect halides can have in the ozone destruction process, as well as their ability to inhibit flame speeds under combustion settings. During the study of the abstraction reaction, a novel double exchange process between HO_2 and hydrogen halides was discovered. These new exchange reactions were found to have barriers significantly lower than the corresponding abstraction process due to a highly structured transition state which is characterized as a planar ring. The kinetics of the abstraction and the exchange process were also compared. It was found that due to a competition between entropic and energetic effects the abstraction process dominates at high temperatures and the exchange reaction is more significant at low temperatures.

The kinetics of gas-phase reactions between HO_2 and OH with pyruvic acid were also examined. Pyruvic acid is an important keto-acid intermediate formed from the oxidation pathway of isoprene. This molecule is unique due to slow oxidation rates by OH and the ability to absorb in the UV-vis region. These characteristics lead to photolysis being the primary channel for degradation in the troposphere. In this work, accurate rate coefficients are determined for use in

atmospheric models and compared to experimental estimates. Due to the number of possible hydrogen transfer reactions in pyruvic acid, reactions with hydroperoxy radicals were also examined to see if barrier lowering effects could play a role under atmospheric conditions. It was found that although HO_2 mediation produced a catalytic effect on the reactions barriers, the high energy products of the reactions made this effect negligible on the rate constants.

Acknowledgements

Completion of this dissertation would have not been possible without the support of many people. I am indebted to my adviser Prof. Rex T. Skodje for his support and mentorship. Rex guided me towards growing into an independent researcher, while continuing to provide invaluable feedback, perspective, and encouragement.

I gratefully acknowledge my committee members: Prof. Niels Damrauer, Prof. Sandeep Sharma, Prof. Veronica Vaida and Dr. John Orlando. They generously gave their time and energy to provide me with thoughtful feedback towards improving my dissertation work. I also thank Prof. Hai Lin for seeing potential in me as an undergraduate student, setting me on my path to graduate school.

I am also grateful to the teaching faculty in the chemistry department, especially Dr. Kathryn Plath, Dr. Christine Kelly, and Dr. Margaret Asirvatham for their encouragement and support while I worked as a TA for the department.

I also credit the completion of my dissertation to my friends in the doctoral program and from other parts of my life. I am grateful to fellow Skodje group members Shirong Bai and Robert Wells for their comradery, troubleshooting, and entertainment. I thank Hayden Hamby, Alyssa Landin, Jasmine Wallas, and Dave Zywotko for being a reliable source of friendship, support, advice, and comic relief. Hayden in particular has seen me through some of my most challenging moments during graduate school for which I am extremely grateful. I thank Mark Ballock and Abhishek Shetty for helping me keep my grip on the world outside of academia. I could always rely on our weekends playing pool to provide me with a healthy break from work. I thank Lauren Min for her constant support and friendship; her support and counsel in difficult times were invaluable.

I am deeply thankful to my mom for her unconditional support and encouragement, not only during my time in graduate school but throughout my life. Any success I have had can most certainly be attributed to her.

Table of Contents

Tables

Figures

Chapter 1

Introduction

Radical species are known to play important roles in a variety of chemical environments ranging from reactions in the atmosphere to chemical combustion chambers. Although there are many radical species that are important in both atmospheric and combustion chemistry, the present work will primarily focus on gas-phase reactions involving either HO_2 or OH radicals.

Although both of these molecules are unstable radicals, hydroxyl radicals are known to be highly reactive and have much shorter lifetimes in comparison to those of hydroperoxy radicals.[1] Sources of hydroxyl radicals can include the decomposition of hydroperoxides or under atmospheric settings they can be formed photochemically from atomic oxygen reacting with water. [1 2 3] Due to the high reactivity of these radicals, the typical lifetime of an OH molecule is less than one second while in clean air and can be as short as 10 ms while in polluted air. [1 4] This is much lower than the average lifetime of a HO_2 radical which typically has a lifetime of approximately 100 seconds.[1] Current measurements put the average global concentration of OH in the troposphere to be much lower than that of HO_2 radicals due to the increased reactivity and shorter lifetimes than that of HO_2. This difference in relative abundances can be quite large under certain conditions, where HO_2 has been approximated to be 100 times more abundant during the day. [1] In tropospheric chemistry, hydroxyl radicals have been known to play a role in the removal of some pollutants and greenhouse gasses.[5 6] Hydroxyl radicals have also been shown to be responsible for the production of several organic radical precursors from reactions with volatile organic compounds. [1] Hydroxyl radicals are also important in combustion systems, where its interaction with fuel components is known to be an important elementary step in almost all combustion mechanisms.[7]

Although HO_2 radicals are typically less reactive than OH, they are still important in both atmospheric and combustion chemistry. Under atmospheric conditions they are a source of organic peroxy radicals, and they can also react with compounds such as NO to produce hydroxyl radicals.[1] In combustion models, reactions involving HO_2 have often been found to be highly sensitive during sensitivity analysis.[8] [9] In the case of the combustion of methanol and butanol, reactions involving HO_2 have been found to be the most sensitive during sensitivity analysis.[9] It's self-reaction has also been found to be important in combustion models during the ignition process.[9] [10]

The first study of this thesis focuses on two reactions between HO_2 and hydrogen halides. Similar to HO_2 and OH radicals, halides species are known to play roles under both atmospheric and combustion settings. For example, in combustion chemistry certain halides have been shown to act as flame retardants.[11] [12] Whereas, in atmospheric chemistry, halogens have been known to have catalytic cycles that can destroy thousands of ozone molecules per halogen atom.[13]

The abstraction process between HO_2 and HX is one potential source for halide radicals. During the study of the abstraction reaction, a novel double hydrogen exchange process was discovered. The exchange reactions between these chemical species were found to have a barrier lowering effect when compared to the abstraction process. Although novel for these systems, barrier lowering effects from hydrogen exchange have been observed before with other molecules. For example, water has been found to have the ability to mediate concerted H-atom exchange reactions which can provide a much lower barrier pathway compared with direct single H-atom exchange. An influential example of this effect was provided by Morokuma and Muguruma [14] who studied the $SO_3+H_2O \rightarrow H_2SO_4$ reaction. Spurred by experimental observation,[15] [16] [17] these authors found that by adding a single water molecule the transition state barrier was lowered by over 25 kcal mol^{-1}. Skodje and coworkers have also demonstrated a substantial lowering of the TS barrier

via concerted reactions while studying the $CH_2FOH \rightarrow CH_2O + HF$ and $CH_2(OH)_2 \rightarrow CH_2O + H_2O$ reactions for clusters containing up to three water molecules.[18 19] Francisco and coworkers[20 21] have shown that multiple H-atom transfer reactions can be important for a variety of atmospheric reactions. There are also numerous other theoretical studies that show similar TS barrier lowering behavior for reactions in water clusters.[22-27]

These types of concerted H-atom transfer reactions have also been found to occur for the hydroperoxy radical, although they have been studied in less depth than those of water. Karton[28] studied the HO_2 catalyzed tautomerization of vinyl alcohol, $HO_2 + CH_2CHOH \rightarrow HO_2 + CH_3CHO$, and also noted the catalytic power of several other inorganic acids. da Silva[29] investigated a double hydrogen exchange reaction involving glyoxal and HO_2 that ultimately leads to OH formation. Gas phase keto-enol isomerization was shown to occur through a double proton exchange mechanism mediated by carboxylic acids.[30] In this work I will show that HO_2 can mediate hydrogen transfer with a hydrogen halide. While the application of the chemistry itself is less clear, the simplicity of these reactions allows the study of how simple chemical characteristics affect the ability of HO_2 to act as a hydrogen transfer mediator. This can be useful while studying other concerted multiple hydrogen atom transfer reactions involving hydrogen bonded species. It is also important to emphasize that concerted multiple H-atom can occur for such simple halogen containing species.

In the second study of this thesis, the reactions between HO_2 and OH with pyruvic acid are examined. Pyruvic acid, a keto-acid intermediate of the isoprene oxidation channel, has found in the troposphere under a variety of conditions in large mixing ratios. [31 32 33 34 35 36 37] Isoprene is a volatile organic compound (VOC) and these types of organics have been linked to secondary organic aerosol formation (SOA) as well as smog and haze formation when hydroxyl radicals are

available. [38] [39] Pyruvic acid is a unique compound because unlike many VOCs which react readily with OH, photolysis is thought to be the primary degradation pathway with OH merely acting as a secondary sink. [40] [41] Although thought to be slow little research has been done on obtaining good rate constants for atmospheric models, with the work by Mellouki and Mu being the only source of direct experimental measurements.[40] In this work the reactions between OH and pyruvic acid are examined in an attempt to better categorize the reaction. The reactions between HO_2 and pyruvic acid were also studied. It was thought that similar to the work in the first study, HO_2 could help mediate some of the hydrogen transfer reactions.

Chapter 2

Theoretical Methods

2.1 Introduction

In this thesis conventional transition state theory (TST) was employed to obtain thermal rate constants using barriers and frequencies determined from density functional theory (DFT). In the second study, coupled cluster single-double with perturbative triples CCSD(T) is also used for energetic calculations to compare to the DFT results. Density functional theory was used to determine the relative energies, barrier heights and frequencies in the various systems studied due to the balance between accuracy and computational cost in determining reaction energetics. Small-curvature tunneling corrections were obtained from intrinsic reaction coordinates calculated with the Gonzalez-Schlegel 2nd order (GS2) algorithm. Quantum theory of Atoms in Molecules (QTAIM) was also performed in order to explain the relative barrier heights of the halide systems studied in this thesis. The following section will provide relevant background information on the methodology used in this thesis.

2.2 Density Functional Theory

The Hamiltonian for a N-body system interacting via a coulombic potential is given by Equation 2.1.

$$\widehat{H} = \sum_{i=1}^{N}\left(-\frac{\hbar^2}{2m}\nabla_{\mathrm{i}}^2\right) + \frac{1}{2}\sum_{i=1}^{N}\sum_{j\neq i}^{N}\frac{Z_i Z_j}{4\pi\epsilon_o|r_i - r_j|} \tag{2.1}$$

When dealing with a molecular system, both the kinetic energy and coulombic terms can be split into separate electronic and nuclear contributions.

$$\hat{H} = \hat{T}_n + \hat{T}_e + \hat{U}_{ee} + \hat{U}_{en} + \hat{U}_{nn} \tag{2.2}$$

One approximation that is made when solving for the energy of an N-body molecular system is the Born-Oppenheimer approximation. The Born-Oppenheimer approximation states that due to the large relative difference in masses between electrons and nuclei one can separate nuclear and electronic motion and treat the energy of the system as a function of nuclear coordinates. The Born-Oppenheimer Hamiltonian thus has the following form.

$$\hat{H}_e = \hat{T}_e + \hat{U}_{ee} + \hat{U}_{en} + \hat{U}_{nn} \tag{2.3}$$

This electronic Hamiltonian can be used to solve the electronic energy as a function of nuclear coordinates with the electronic wavefunction $\phi(r, R)$.

$$\widehat{H_e}\phi(r, R) = E_{el}(r, R)\phi(r, R) \tag{2.4}$$

Although the exact equations to solve for the electronic energy of a molecular system are known, analytical solutions are impossible for a many-body problem. This is due to the electronic repulsion term and the fact that the electrons in the exact electronic wavefunction are coupled and non-separable. Methods that take the B.O. Hamiltonian and make further approximations have been developed in order to solve for molecular energies. One such method is the Hartree-Fock approximation which treats the electrons of a molecular system as a mean field. Although the Hartree-Fock approximation allows us to solve for the energy of a many-body system, it also fails to consider any electron correlation for the molecular system and additional ab initio methods have been developed which try to take correlation energy into account such as, configuration interaction (CI), coupled cluster (CC), Møller-Plesset perturbation theory (MP), etc.

For large chemical systems these ab initio methods can be very computationally demanding because they scale with the number of electronic coordinates. Density functional theory (DFT) on

the other hand merely uses the electron density as a function of the three cartesian coordinates to solve for the energy of the system and can often yield reasonable results at a much lower computational cost.

Density functional theory (DFT) uses functionals to calculate the energy as a function of electron density. There are two important theorems that were used in the development of DFT which are known as the Hohenberg-Kohn theorems[42] and are as follows:

1. *The external potential is a unique functional of the electron density only. Thus the Hamiltonian, and hence all ground state properties, are determined solely by the electron density.*

2. *The ground state energy may be obtained variationally: the density that minimizes the total energy is the exact ground state density.*

These theorems simply state that ground state expectation values of observables are functionals of the ground state density, and that there must exist some unknown universal functional of the electron density which would yield the ground state energy for an N-body system from its ground state electron density. Although these theorems lay the foundation for DFT they fail to indicate how to solve for the ground state density and thus the energy of the ground state for of an N-body system. To provide a way to use these theorems Kohn and Sham formulated a method to solve for the electron density of a system.[43] Their ansatz is that a N-body system of interacting particles can be solved for by the density of a system of non-interacting particles. This means that the ground state wavefunction of a system can be given exactly by a single slater determinant of single particle orbitals. This procedure allows us to solve for the electron density of a molecular system, because we can now obtain the electron density from the newly created wavefunction.

$$n(r) = \sum_{j=1}^{N} |\psi_j|^2 \tag{2.5}$$

As mentioned by the HK theorems, the total electronic energy of a molecular system is a functional of the ground state electron density. Just like in the Electronic Hamiltonian in Equation 2.3, the electronic energy can be further decomposed into both a kinetic and potential contribution and each of these components are also a function of the electron density.

$$E[n(r)] = T[n(r)] + E_{en}[n(r)] + E_{ee}[n(r)] \tag{2.6}$$

Here there are potential terms for both the electronic-nuclear repulsion and electronic-electronic repulsion. The electron-electron repulsion term can be separated into a coulombic repulsion energy and an exchange-correlation E_{xc} energy term, $E_{ee}[n(r)] = J[\,n(r)] + E_{xc}[n(r)]$. The exact exchange-correlation functional is unknown and presently we can solve for each energetic term exactly except for that of the exchange-correlation. There have been many methods proposed over the years in order to try and approximate this unknown functional. Using an approximated form for this functional, the energy of a molecular system can be solved in a self-consistent iterative process similar to that of a Hartree-Fock SCF calculation. In this work DFT is used for stationary point optimization, frequency calculations and reaction energetics. There are a wide number of existing functionals to choose from with each functional performing well for certain systems. In this work heavy halides are examined as well as many main group elements, and the appropriate functional needs to be selected.

In the literature, certain functionals have been reported to have lower errors in energetic calculations for halide systems, including many of the Minnesota functionals developed by the Truhlar group, BMK, and the ωB97 family.[44] [45] Kozuch *et al.* reported on the effectiveness of different functionals at predicting the properties of halogen bonds by using a wide number of

model systems.[45] These authors found that many of the Minnesota functionals provided both excellent geometries and energetics. The M06-2x functional for example was found to have energetic RSMD errors of approximately 0.43 kcal/mol and a maximum error of 1.58 kcal/mol. Although DFT typically has larger errors associated with predicted energetic values than that of ab initio methods, under certain conditions some functionals have been found to perform as well as the average accuracy of CCSD(T).[46] In the first study of this thesis a group of these functionals will be examined to see which predicts the most accurate energetics for the systems studied when compared to thermodynamic data. This will include the M11 functional, which is a newer member of the Minnesota functional family developed by the Truhlar group. This functional was developed to be more accurate for a wider range of reactions than its predecessors such as the M06 and M05 sets of functionals.[47] [48] [49] [50] A more recent study on the cycloreversion of heterocyclic rings by Yu *et al.* found the M11 functional provided the best performance with a RMSD error of 1.14 kcal/mol from an ab initio benchmark when compared to other functionals designed for main group chemistry.[51] M11 also appears to be accurate at determining the energetics of systems with only main group elements. For example, a study by Friedrich *et al.* found that M11 was very accurate when predicting the energetics for large water clusters. [52]

2.3 Coupled Cluster Methods

In the second study of this thesis many of the reaction barriers were found to be similar in magnitude to the maximum error that can arise from a typical DFT calculation. Because of the small reaction barriers and low temperatures studied both ab initio and DFT methods were used to predict the reaction energetics. In this study Coupled Cluster with perturbative triples CCSD(T) was the ab initio method chosen to calculate the reaction energetics. CCSD(T) is commonly known as the gold standard of single determinant methods in computational

chemistry.[53] [54] [55] Although this method provides both accurate bond energies and geometric structures it is also extremely computationally expensive as it scales as N^7 with the number of basis functions, for comparison DFT is thought to scale as N^3.[53] This large computational cost tends to limit CCSD(T) to energetic calculations for larger systems while using the optimized structures and frequencies from a less computationally expensive method. For systems well suited for single reference methods CCSD(T) typically give energetic errors less than 1 kcal/mol.[56] Multiple studies have also reported errors less than 0.2 to 0.5 kcal/mol when using CCSD(T) to obtain the thermochemical data.[57] [58] [59]

2.4 Basis Set Expansion

In order to solve for the wavefunctions of the systems being studied a basis must first be defined. The most common procedure is to expand the wavefunction into a linear combination of known functions.

$$\psi(r) = \sum_i c_i \, \phi_i \, (r) \tag{2.7}$$

Here ψ is the wavefunction we are interested in solving for, $c_i \, \phi_i$ are the known functions and their respective weighting factors. For gas phase chemistry the basis is usually a combination of contracted gaussian functions which have the form $\phi_i(\mathrm{r}) = c_i \exp(-\zeta_i r^2)$, each of which represent a basis function for the wavefunction in question. John Pople realized a split basis was necessary to describe the valence orbitals to obtain more accurate results.[60] [61] Often there are also more functions added to take any polarization effects of these orbitals into account and for anionic species there are functions added to consider any diffuse effects. Typically, the more functions added into the system to describe the wavefunction will yield more flexibility in the description of

the system and thus results that are closer to the true value. The coefficients of these basis functions are then optimized using a variational self-consistent field approach such as HF or DFT until the energy is self-consistent.

Newer sets of basis functions have been developed which are meant to take electron correlation into account, one of the most widely used would be the set developed by Dunning Jr. and coworkers.[62 63 64 65 66] Dunning's correlation consistent basis functions take the form cc-pVXZ, where X indicates the split of the valance and can be D for double zeta, T for triple zeta, etc. The coefficients of these basis functions were optimized using correlation methods and are meant to give smooth convergence to the complete basis set limit. By solving for the energy of the system with multiple zeta values the energy at the complete basis limit can be approximated. In this work the energy was extrapolated to the complete basis set (CBS) limit using the three basis sets (X=D,T,Q) and an inverse cubic function extrapolation scheme.

$$E(n) = E_{CBS} + An^{-3} \tag{2.10}$$

2.5 Transition State Theory

Transition state theory (TST) was used to determine thermal rate constants of the various bimolecular chemical reactions studied. For reactions that occur from a single conformer the thermal rate constant can be determined from Equation 2.8.

$$k^{TST}(T) = \frac{k_B T}{h} \frac{Q^{\ddagger}/V}{\mathrm{Q_A/V \cdot Q_B}/V} \, \mathrm{e}^{-\frac{\Delta E^{\ddagger}}{k_B T}} \tag{2.8}$$

The canonical partitions functions $Q_{A,j}$, $Q_{B,k}$, and $Q_i^{\ddagger}$, were calculated using the harmonic oscillator-rigid rotor approximation using the parameters at the stationary points of the potential and $\Delta E_0^{\ddagger}$ is taken as the zero-point corrected barrier between the reactants and transition state.

Occasionally a system will contain either a reactant or transition state with multiple conformers. When this occurs a modified expression for the rate constant must be used. Pyruvic acid is examined in the second study of this work and this molecule has two major conformations found in the gas phase. When calculating the rate coefficients for these systems, both conformations were accounted for using multi-path transition state theory with a local harmonic approximation to compute the rate coefficients for each set of reactions.[67 68 69]

$$k(T) = \frac{k_B T}{h} \frac{\sum_i^{All\ TS} \kappa_i(T)\, Q_i^{\ddagger}/V \exp\left(-\frac{\Delta E_i}{k_B T}\right)}{\sum_j^{All\ R_A} Q_{A,j}/V \exp\left(-\frac{\Delta E_j}{k_B T}\right) \sum_k^{All\ R_B} Q_{B,k}/V \exp\left(-\frac{\Delta E_k}{k_B T}\right)} \exp\left(-\frac{\Delta E_0^{\ddagger}}{k_b T}\right) \qquad (2.9)$$

Once again the canonical partitions functions $Q_{A,j}$, $Q_{B,k}$, and $Q_{i^{\ddagger}}$, were calculated using the harmonic oscillator-rigid rotor approximation using the parameters at the stationary points of the potential. Now $\Delta E_0^{\ddagger}$ is taken as the zero-point corrected barrier between the lowest energy conformation of the transition state and the lowest energy conformer of the reactants. ΔE_j, ΔE_k, and ΔE_i are the zero-point corrected energy differences between structures *j*, *k*, and *i* and their respective lowest energy conformer. Quantum mechanical tunneling is included in the rate expression by a transmission coefficient $\kappa_i(T)$ determined using small-curvature tunneling. A transmission factor is included for each transition state conformer by multiplying each transmission coefficient by its respective transition states partition functions.

The canonical partitions functions used in the transitions state theory expressions are a product of the translational, rotational, vibrational and electronic partition functions for that species.

$$Q = q_{trans} q_{rot} q_{vib} q_{el} \qquad (2.10)$$

For a gas phase molecular system with three degrees of translational freedom, the translational partition function of a molecule can be simply calculated from the molecular mass m and the temperature of the system.

$$q_{trans} = \left(\frac{2\pi m k_B T}{h^2}\right)^{\frac{3}{2}} V \tag{2.11}$$

The rotational partition function depends on a symmetry factor σ, the moment of inertia of the molecule in question and the temperature of the system. For a system with three rotational degrees of freedom the rotational partition function has the following form.

$$q_{rot} = \frac{\pi^2}{\sigma}\left(\frac{8\pi I k_B T^3}{h^2}\right)^{\frac{1}{2}} \tag{2.12}$$

For a linear diatomic molecule such as an OH radical, the moment of inertia can simply be determined by the reduced mass of the molecule μ, as well as the molecular bond length r.

$$I = \mu r^2 \tag{2.13}$$

For a non-linear polyatomic molecule the inertia calculation can be more complicated. For these systems the moment of inertia can be split into three components, I_A, I_B and I_c.

$$I = I_A I_B I_C \tag{2.14}$$

In cartesian coordinates these components can be solved for by building an inertia matrix from the cartesian coordinates of the molecule and then diagonalizing the resulting matrix.

$$I_p = \begin{bmatrix} I_{xx} & -I_{yx} & -I_{zx} \\ -I_{xy} & I_{yy} & -I_{zy} \\ -I_{xz} & -I_{yz} & I_{zz} \end{bmatrix} \tag{2.15}$$

$$I_p = \begin{bmatrix} I_A & 0 & 0 \\ 0 & I_B & 0 \\ 0 & 0 & I_C \end{bmatrix} \tag{2.16}$$

Once the three components of the molecular inertia are obtained they can be used to calculate the rotational partition function by substituting in $I_A I_B I_C$ for I .

$$q_{rot} = \frac{\pi^2}{\sigma}\left(\frac{8\pi I_A k_B T}{h^2}\right)^{\frac{1}{2}}\left(\frac{8\pi I_B k_B T}{h^2}\right)^{\frac{1}{2}}\left(\frac{8\pi I_C k_B T}{h^2}\right)^{\frac{1}{2}} \tag{2.17}$$

The vibrational partition function depends on the real eigenvalues of the vibrational modes. These eigenvalues can be obtained by performing normal mode analysis and then mass weighting the resulting force constant matrix. This mass weighted matrix is known as the Hessian whose eigenvalues are the square of the frequencies of the normal modes of the molecule. For a minimum stationary point on the potential there will be either five or six zero frequencies for a diatomic or a polyatomic respectively with either 3N-5 or 3N-6 real frequencies. These zero frequencies result from the translational and rotational motion of the molecule. The vibrational partition function for a minimum has the following form.

$$q_{vib} = \sum_{i}^{3N-6/5} \frac{1}{1 - \exp\left(-\frac{h\nu}{k_B T}\right)} \tag{2.18}$$

To obtain the vibrational partition function one simply sums over this expression for the real vibrational frequencies of the molecule. For a first order saddlepoint on the potential surface there will be six zero frequencies as well a single imaginary frequency and 3N-7 real modes. The vibrational partition function for a saddlepoint has the same form, except the imaginary frequency corresponding to motion along the reaction path is excluded.

$$q_{vib} = \sum_{i}^{3N-7} \frac{1}{1 - \exp\left(-\frac{h\nu_i}{k_B T}\right)} \tag{2.19}$$

The electron partition function of a molecular system is based on the degeneracy of the electronic states available to the molecular system.

$$q_{el} = g_o + \mathrm{g}_1 \exp\left(-\frac{E_2}{k_B T}\right) + \mathrm{g}_2 \exp\left(-\frac{E_3}{k_B T}\right) + \cdots. \tag{2.20}$$

For nonlinear polyatomic molecules the electronic degeneracy is calculated from the spin degeneracy of the molecule, $g_{el} = (2S + 1)$. Usually the energies of excited electronic states are much larger than that of the reference state and the electronic partition function is simply the degeneracy of the reference state, ie for a singlet $q_{el} = 1$ and for a doublet $q_{el} = 2$, and so on. Linear molecules such as hydroxyl radicals have both spatial and spin symmetry which need to be considered when calculating the electronic partition functions. Furthermore, when calculating the electronic partition function of the OH radical the fine splitting of the doublet ground state needs to be taken in account, each of these states differ by 140 cm^{-1} and this must both also be considered for the electronic partition function.[70] [71] [72]

2.6 Intrinsic Reaction Coordinate

Quantum mechanical tunneling was also incorporated into the rate expression using a transmission coefficient $\kappa(T)$.

$$k(T) = \kappa(T) \cdot k^{TST}(T) \tag{2.21}$$

The transmission coefficients were computed using the small-curvature tunneling (SCT) method, which is similar to the zero-curvature tunneling (ZCT) method except the curvature of the reaction path is considered.

In order to determine the tunneling correction for a given system using the SCT method, both the minimum energy path as well as Hessian matrices along the path are required. The intrinsic reaction coordinate (IRC) was defined by Fukui in the 1970's as the mass weighted steepest descent path on the potential energy surface starting from a first order saddle point.[73] Solutions for the IRC can be obtained by solving the following differential equation.

$$\frac{d\overrightarrow{q_m}(s)}{ds} = \vec{n}(s) \tag{2.22}$$

Here $\frac{d\overrightarrow{q_m}(s)}{ds}$ are the mass weighted displacements in cartesian coordinates along the reaction path s and $\vec{n}(s)$ is the unit vector obtained from the gradient at point s on the reaction path. It is convention to state that $s = 0$ as the first order saddle point, $s < 0$ going to the reactants and $s > 0$ going to the products. Although this expression appears to be relatively simple, the function can exhibit stiff character and can also be challenging to integrate when the gradient of the path approaches zero.[74] [75] [76] There are a wide selection of integrators that can be used to solve for the reaction path with each method producing paths with various degrees of accuracy. Some integrators which have been used include simple Euler integration, Runge-Kutta of various orders, Page and McIver's local quadratic approximation (LQA) and the Gonzalez-Schlegel 2nd order algorithm. [77] In this thesis the GS2 algorithm was selected because it is a fairly robust algorithm that allows for a fairly large step size during integration while still yielding accurate results.[74] [75] [76] [78] The method is also quite good at handling the stiffness problem frequently encountered when solving for an IRC.[75] The GS2 algorithm is characterized as a gradient following method coupled with a constrained optimization on a hypersphere of fixed radius. The algorithm first takes a half and full step along the reaction path using a simple Euler approach with a step-size of termed l to

avoid confusion with the true reaction path variable *s*, and these half and full steps are given by equations 2.26 and 2.27 respectively.

$$q^*_{m_k} = q_{m_i} - \frac{1}{2} l\, \vec{n}(s) \tag{2.23}$$

$$q_{m_k} = q_{m_i} - l\, \vec{n}(s) \tag{2.24}$$

Here $q^*_{m_k}$ and q_{m_k} are the mass weighted cartesian coordinates of the half and full step respectively. Next using a quadratic expansion of the potential energy surface at the current location on the reaction path, a constrained optimization on a hypersphere with a fixed radius of $\frac{1}{2} l$ is performed as illustrated in Figure 2.1. The vector between the center point of the hypersphere $q^*_{m_k}$ and points on the surface of that sphere are labeled as $\overrightarrow{p_m}$ and the mass weighted displacements between two points on the hypersphere are labeled $\delta\overrightarrow{q_m}$.

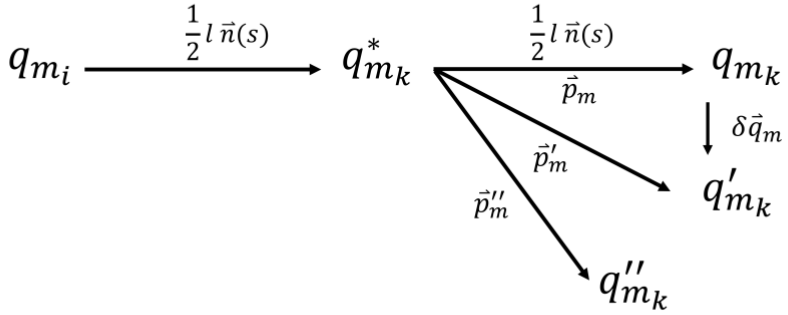

Figure 2.1 Illustration of GS2 path finding algorithm.

The displacement vector $\delta\overrightarrow{q_m}$, must be determined in order to find the next point on the hypersphere during the optimization process. The displacement on the hypersphere in mass weighted coordinates can be defined as the following

$$\delta\vec{q}_m = -(H_m - \lambda I)^{-1}(\vec{g}_m - \lambda\vec{p}_m) \tag{2.25}$$

In order to find $\delta\overrightarrow{q_m}$ with this expression the Lagrange multiplier λ must first be determined, which can be found with the following equation which comes from a quadratic expansion of the energy and imposing the constraint that the hypersphere has a radius of $\frac{1}{2}l$ as shown by Gonzales and Schlegel.[77]

$$[\vec{p}_m - (H_m - \lambda I)^{-1}(\vec{g}_m - \lambda\vec{p}_m)]^T[\vec{p}_m - (H_m - \lambda I)^{-1}(\vec{g}_m - \lambda\vec{p}_m)] - \left(\frac{1}{2}l\right)^2 = 0 \tag{2.26}$$

Here H_m is the Hessian matrix and I is the identity matrix. For each step during the optimization process the Hessian needs to be determined in order to determine the correct multiplier. The Hessian can either be computed from scratch or updated using a numerical method such as the Broyden–Fletcher–Goldfarb–Shanno (BFGS) method. In this work the Hessian at each step along the reaction path was reevaluated as well as for each micro-iteration of the optimization process. Although this procedure can be more expensive for larger systems, recalculating the Hessian at each point can help reduce error in the IRC and should also allow larger step sizes to be taken.

Once the Hessian has been determined at a given point, the Lagrange multiplier can then be solved using a variety of methods, but in this work a simple root search on Equation 2.26 was used. One important thing to note is that λ must be negative and less than the lowest eigenvalue of the Hessian in order to ensure a downhill optimization step. This optimization process is carried out until $\delta\overrightarrow{q_m}$ and the gradient tangent to the hypersphere is less than some predetermined cutoff

preferably as close to zero as possible. Once the optimization process is complete based on the initial criteria, the energy, Hessian, gradient and coordinates at the new point are saved to a file and a new step and half step are taken with Equations 2.26 and 2.27. This process is then repeated until the maximum value of the mass weighted gradient of the potential surface along the path is less than a predetermined cutoff value.

After obtaining the IRC, the adiabatic potential can be determined from the coordinates, energy and Hessian determined at each point. The adiabatic potential along the reaction path is defined as the following.

$$V_a^G(s) = V_{MEP}(s) + \frac{1}{2}\sum_{i}^{3N-7} \hbar\omega_i(s) \tag{2.27}$$

$$V_{MEP}(s) = V(s) - (V_{reactant_1} + V_{reactant_2}) \tag{2.28}$$

Here $V_{MEP}(s)$ is the energy of the path at point s which is then scaled by the potential energies of the reactants at infinite separation and $\omega_i(s)$ are the real non-zero frequencies at point s, determined from the corresponding projected Hessian matrix. The adiabatic path and the projected Hessians along the path can then be used to find the small-curvature tunneling corrections as outlined in the following section.

2.7 Small Curvature Tunneling

The small curvature tunneling method is a semiclassical approximation to find the tunneling through an adiabatic barrier. Similar to WKB theory, the transmission probability through a potential barrier is dependent on the amount of imaginary action.

$$P(E) = \frac{1}{1 + e^{2\theta(E)}} \tag{2.29}$$

Here $P(E)$ is the quantum transmission probability through a one-dimensional barrier and the quantity $\theta(E)$ is the imaginary action integral computed between the classical turning points, $(s_<, s_>)$, of the adiabatic barrier curve $V_a^G(s)$

$$\theta(E) = \frac{2\pi}{h}\int_{s_<}^{s_>} ds\sqrt{2\mu(V_a^G(s) - E)} \tag{2.30}$$

Typically when the reaction path is mass weighted and curvature effects are neglected, such as in the case of the zero-curvature tunneling (ZCT) method, the reduced mass $\mu(s)$ is set to 1 amu. However, in the small-curvature tunneling approximation the curvature of the reaction path is factored into this expression by using an effective reduced mass $\mu_{eff}(s)$ which is a coordinate-dependent expression and is smaller than the collisional reduced mass reflecting the shortened tunneling path. The mass is determined from the adiabatic potential and the normal modes along the reaction path obtained from the GS2 algorithm as explained in Section 2.6, the effective mass is defined as the following

$$\mu_{eff}(s) = \mu \times \min\left[\exp\left(-2a(s) - [a(s)]^2 + \left(\frac{d\vec{\tau}(s)}{ds}\right)^2\right)\right] \tag{2.31}$$
$$1$$

The effective mass is always less than or equal to the normal reduced mass and thus the SCT approximation always has equal or larger transmission coefficients than that of the ZCT method. In this expression $\vec{a}(s)$ is defined at the product of the path curvature, $\kappa(s)$, and turning point of the zero-point energy motion, $\vec{\tau}(s)$.

$$\vec{a}(s) = |\kappa(s) \cdot \vec{\tau}(s)| \tag{2.32}$$

The curvature of the reaction path can be determined directly from the individual curvature coupling components.

$$\kappa(s) = \left(\sum_{i}^{3N-7} |\vec{\kappa}_i(s)|^2 \right)^{\frac{1}{2}} \tag{2.33}$$

These coupling terms can be determined from the unit vector perpendicular to the path and the eigenvectors of the ith vibrational mode.

$$\vec{\kappa}_i(s) = -\sum_{j=1}^{3N} \frac{d\overrightarrow{n_j}(s)}{ds} L_{j,i}(s) \tag{2.34}$$

Similarly the zero-point energy vibrational turning point can be determined from these individual coupling components of the ith mode and the frequency of the ith mode at each point along the reaction coordinate.

$$\vec{\tau}(s) = \kappa(s)^{\frac{1}{2}} \left[\sum_{i}^{3N-7} [\vec{\kappa}_i(s)]^2 \omega_i^2(s) \right]^{-\frac{1}{4}} \tag{2.35}$$

Using the zero-point energy turning point and reaction path curvature the $\vec{a}(s)$ value can be determined and used to solve for the effective reduced mass at point *s* as shown in Equation 2.34.

Using the effective reduced mass obtained for each point along the reaction coordinate and the imaginary action integral $\theta(E)$ can be obtained from Equation 2.30 and then used to solve for the transmission probability as a function of energy. Finally, a thermal transmission coefficient can be obtained by using a normalized Boltzmann average of the small-curvature tunneling transmission probability.

$$\kappa(T) = \frac{\int_{E_o}^{\infty} P(E) e^{-\frac{E}{k_B T}} dE}{\int_{E^{\ddagger}}^{\infty} e^{-\frac{E}{k_B T}} dE} \tag{2.36}$$

Here E_o is the threshold energy of the reaction, $E^{\ddagger}$ is the maximum of the adiabatic barrier and $P(E)$ is the small curvature tunneling transmission probability determined from the imaginary action integral.

2.8 Quantum Theory of Atoms in Molecules

In the first study found in this thesis, the Quantum Theory of Atoms in Molecules (QTAIM) model is used to help explain relative barrier heights for a series of reactions. This model uses molecular electron density to interpret chemical phenomenon. In this theory, the electron density distribution function is used to explain phenomenon such as hydrogen bonds and the aromatic properties of rings. [79] [80] One measure obtained from QTAIM is known as the delocalization index, which is based on the electron exchange-correlation density (XCD). Values of the delocalization index, $\delta(A,B)$, correspond to the number of electrons delocalized between two atoms, A and B.[81] [82] [83] [84] [85] In terms of natural molecular orbitals the delocalization index can be defined as the following.

$$\delta(A,B) = -2 \sum_{l,m} n_l^{\frac{1}{2}} \; n_m^{\frac{1}{2}} \; S_{l,m}(A) \, S_{l,m}(B) \tag{2.37}$$

Here $n_l^{\frac{1}{2}} \; n_m^{\frac{1}{2}}$ are the occupation numbers of orbitals l and m and $S_{l,m}$ are the off diagonal elements of the overlap matrices between these two orbitals which can be defined as the orbital overlap over the atomic domains of atoms A and B.

$$S_{l,m}(A) = \int \phi_{l,A}(r)\phi_{m,A}(r)dr \tag{2.38}$$

The delocalization index has been used to study properties of molecules such as halogen bonds, solvation effects, and aromaticity, [85] [86] [87] [88] [89] including open shell species.[90] In the present work, a wavefunction for the TS was obtained at the M06-2X/DZP level of theory using the GAMESS-US which then serves as input for the computation of the delocalization index via the AIMAll program.[91]

Chapter 3

Abstraction and Exchange Reactions of Hydrogen Halides

3.1 Introduction

Similar to HO_x radicals, halide species have been known to play important roles in both atmospheric and combustion chemistry. For example, in combustion chemistry certain halides have been shown to act as flame retardants.[11 12] Bromine for example has been found to have an effect on both laminar flame speed as well as causing an ignition delay time in combustion systems.[92 93] On the other hand, in atmospheric chemistry, both bromine and chlorine have been known to have catalytic cycles that can destroy thousands of ozone molecules per halogen atom.[13] In more recent research, Saiz-Lopez *et al.* have also suggested that iodine containing species could have catalytic reaction cycles in the troposphere accounting for two to five times more ozone loss than either bromine or chlorine.[94] Raso *et al.* have also suggested that iodine containing compounds could have a significant impacts during ozone depletion events even if these compounds have small mole ratios.[95] Because of the importance of halogens in both combustion and atmospheric systems, accurate rate constants are needed when trying to model these reaction networks. Although the reactions of hydrogen halides with OH have been studied extensively in the literature, reactions with hydroperoxy radicals have been largely ignored, especially for the heavier halides.[96] This chapter of this thesis will focus on hydrogen halide reactions with hydroperoxy radicals in an effort to try and obtain accurate rate constants for chemical models.

The abstraction channel for the reaction of hydrogen halides with peroxy radicals is a potential source of halide radical species, in this work the abstraction process is labeled R1, and is shown in Equation 3.1.

$$R1: \ HO_2 + HX \rightarrow H_2O_2 + X \qquad \text{(X=F, Cl, Br, I)} \tag{3.1}$$

Only the abstraction process with the chlorine and bromine had been studied in any real depth in the literature. In the case of the bromine reaction, the only direct measurement was attempted by Mellouki *et al.* who only provided an upper limit to the rate constant at approximately 3.0×10^{-20} cm^3 molecule/sec at 300K.[97] Several authors have also provided upper limits by using the reverse reaction, but most estimates put the reaction below 10^{-14} cm^3 molecule/sec around room temperature.[98 99 100 101 102] Dixon-Lewis *et al.* performed a kinetic study of the abstraction process of using transition state theory and found that the rate constant at 300K was 3.2×10^{-20} cm^3 molecule /sec.[103] This reported value is approximately three orders of magnitude below the upper bounds set by the direction measurement by Mellouki *et al.* One potential explanation for the discrepancy between theory and experiment could lie with the method used to estimate the tunneling for the rate constant. In the study by Dixon-Lewis *et al.* Wigner tunneling was selected as the method account for tunneling. While the Wigner method is useful due to its simplicity, Wigner tunneling has been shown to underestimate the transmission coefficient, especially for smaller magnitude imaginary frequencies.[104 105 106]

Although no direct measurements of the abstraction process for chlorine had been reported, there are a number of experimental papers who have studied the reverse process, H_2O_2 + Cl → HO_2 + Cl. [107 108 109] A theoretical study by Marouani *et al.* reported a reaction barrier of 3.2 kcal/mol in comparison to an experimental estimate of 1.95 kcal/mol.[110] They also found that their method vastly underestimated the reaction energy -9.5 kcal/mol compared to an experimental value of -17.8 kcal/mol reported by Keyser.[107] Based on literature sources it would appear that the abstraction reactions involving fluorine and iodine have been studied to an even smaller amount than that of chlorine and bromine. Currently there are only two experimental papers on the reverse

reaction of HO_2 with fluorine, and there is currently nothing reported on the HI+HO_2 reaction on the JANAF tables.[111 112]

While investigating this abstraction process a novel double exchange reaction was found which has the following form.

$$R2:\ HO_2 + H'X \rightarrow H'O_2 + HX \qquad \text{(X=F, Cl, Br, I)} \tag{3.2}$$

This double exchange process has been found to proceed through a five-member cyclic ring, as shown in Figure 3.1.

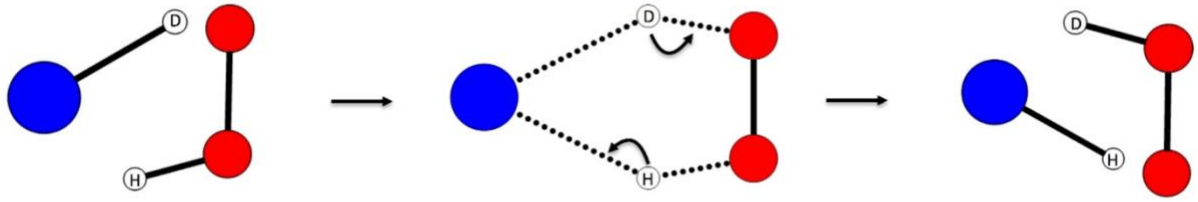

Figure 3.1 Chemical mechanism for the R2 reaction. Here the red circles are oxygen atoms, white are hydrogen and the blue circle represents the halogen.

While the exchange reactions R2 are not chemically observable for H=H′, for other isotopes such reactions may play a role in setting isotope abundances in the atmosphere.

The present combined study of the halogen series, X=F, Cl, Br, and I, for reactions R1 and R2 can provide new insights into the factors that control the barrier lowering effect for multiple H-atom exchange reactions. In the following sections the rate coefficients for the reactions are obtained using TST combined with an accurate determination of the tunneling transmission coefficient discussed previously in Section 2.7. QTAIM results are also presented to explain the barrier lowering effect that is seen between the R1 and R2 reactions for a given halogen. Since multiple H-atom exchange can be a dominant mechanism behind many physical processes,

understanding the factors that influence the barrier lower effect is an important task. In particular, noting the important role of halogen chemistry in the atmosphere and the participation of novel mechanisms in driving the chemistry for atmospheric species possessing long chemical lifetimes.

3.2 Computational Methods

As mentioned previously, DFT was chosen in this study due to the good balance between accuracy and computational cost. The first procedural step for the work in this study was to determine which DFT functional to use. It was important to choose a functional that would yield accurate energetics for use in the transition state theory calculations as well as in determining the intrinsic reaction coordinate. In order to select a functional which would yield reliable results, the reaction energies of the abstraction process for HO_2 + HX, where X=F, Cl, Br, I, were obtained by optimization and CBS extrapolation using several functionals then compared to known energetic values obtained from the JANAF thermochemical tables[113] at 0K. A reaction barrier for HO_2 + HBr reported by Dixon-Lewis *et al.* was also compared to. Several functionals were chosen, including the commonly used B3LYP, several Minnesota functionals, several long-range corrected functionals (wB97, wB97X, wB97X-D), as well as a general purpose functional BMK, which has been developed for high accuracy of reaction barriers.[114] Each functional studied was used to optimize the stationary point structures and obtain their respective normal mode frequencies with DFT/cc-pVQZ. The energy of each species was then obtained by CBS extrapolation using DFT/cc-pVXZ basis where X=(D,T,Q).

Table 3.1 The CBS extrapolated energies of the transition state and products of the R1 reactions from various functionals,as well as the exothermicity of the reaction at 0K determined from the JANAF and ATcT tables.[114 115]The geometry of each stationary point was optimized with the listed functional, and the energy was calculated with the same functional and extrapolated to the CBS limit using a power fit. The results also include harmonic zero point corrections.

$X = F$					$X = Cl$				
Functional	**TS1**	**Product**	ΔE_1	ΔE_2	**Functional**	**TS1**	**Product**	ΔE_1	ΔE_2
M11	N/A	52.00	0.62	2.93	**M11**	19.15	17.89	-0.50	1.88
M06-2X	N/A	48.74	-2.64	-0.33	**M06-2X**	16.01	16.08	-2.31	0.07
B3LYP	N/A	51.54	0.16	2.47	**B3LYP**	10.93	18.50	0.11	2.49
ωb97	N/A	52.42	1.04	3.35	**ωb97**	20.96	20.25	1.86	4.24
ωb97X	N/A	51.49	0.11	2.41	**ωb97X**	18.62	19.90	1.51	3.89
ωb97X-D	N/A	51.48	0.10	2.41	**ωb97X-D**	16.38	19.97	1.58	3.95
BMK	N/A	50.28	-1.10	1.21	**BMK**	16.62	18.61	0.22	2.59
JANAF	N/A	51.38	N/A	2.31	**JANAF**	N/A	18.39	N/A	2.38
ATcT	N/A	49.07	-2.31	N/A	**ATcT**	N/A	16.01	-2.38	N/A
$X = Br$					$X = I$				
Functional	**TS1**	**Product**	ΔE_1	ΔE_2	**Functional**	**TS1**	**Product**	ΔE_1	ΔE_2
M11	10.16	4.07	1.27	3.83	**M11**	5.89	-9.23	4.20	6.57
M06-2X	7.95	-0.74	-3.54	-0.98	**M06-2X**	4.02	-17.00	-3.57	-1.20
B3LYP	5.05	4.88	2.08	4.63	**B3LYP**	2.77	-7.84	5.59	7.96
ωb97	12.49	5.06	2.26	4.82	**ωb97**	8.27	-7.13	6.30	8.67
ωb97X	10.82	4.94	2.14	4.70	**ωb97X**	6.88	-7.70	5.73	8.10
ωb97X-D	8.71	5.22	2.42	4.98	**ωb97X-D**	5.46	-7.52	5.91	8.27
BMK	9.45	2.45	-0.35	2.21	**BMK**	6.41	-10.49	2.94	5.31
JANAF	N/A	2.80	N/A	2.56	**JANAF**	N/A	-13.43	N/A	2.37
ATcT	N/A	0.24	-2.56	N/A	**ATcT**	N/A	-15.80	-2.37	
Dixon-Lewis *et al.*[103]	10.52								

Table 3.1 shows the differences between the reaction energies determined with each functional and the experimental values determined from the JANAF, ΔE_1, and ATcT thermodynamic data, ΔE_2.[114 115] First comparing the values to the JANAF thermochemical data, the B3LYP functional was good at predicting the energy change for the lighter halogen systems X=F, Cl with differences being less than 0.2 kcal/mol for both systems, the functional was less accurate for the heavier halogens X=Br, I. The functional also predicted a

vastly different barrier height for the abstraction barrier of HO_2 + HBr compared to the value reported by Dixon-Lewis *et al.*

Similar to B3LYP, the long-range corrected functionals used in this thesis (wB97, wB97X, wB97X-D) tend to have good agreement for the reaction exo/endo-thermicity for the lighter halogens and bad agreement with the heavy halogens, especially for the iodine system. The M06-2X functional had similar errors for each halogen system studied, with each system having an error of about 2-4 kcal/mol for the reaction energies.

Both the M11 and BMK functionals seemed to perform well at predicting the reaction energies for X=F,Cl, and Br. However, similar to the previously listed functionals both M11 and BMK had large errors in their relative predictions for the exothermicity of the iodine reaction. Despite the large error in the iodine system both M11 and BMK outperformed the other functionals studied in this thesis, with BMK typically having lower errors in the predicted exothermicity than M11. However, the BMK functional predicted a submerged barrier for HCl + HO_2, which is experimentally known to be around 2 kcal/mol greater than the products and the functional also had a larger error than M11 when predicating the barrier height of HBr + HO_2 when compared to the Dixon-Lewis value.

With the exception of M06-2X, all methods studied had worse agreement with the ATcT thermochemical data. The major discrepancy between the JANAF and ATcT thermochemical values was the heat of formation of HO_2 which is 2.42 kcal/mol higher in energy in the ATcT tables.[114 115] Although the M06-2X functional had better agreement with the ATcT tables, it still predicts a submerged barrier for X=Cl, which is known to be higher in energy than the products. The functional also has worse agreement with the previously reported barrier of X=Br. The M11 and BMK functionals were the next best functionals for predicting reaction endo/exo-thermicity

when looking at the ATcT thermochemical data. Thus, for the following study the M11 functional was selected due to its accuracy in determining the exothermicity of several reactions as well as the accuracy in evaluating the barrier heights of the HCl/HBr + HO_2 systems.

3.3 Results

3.3.1 Stationary Point Structures and Energetics

The stationary point structures were optimized using the GAMESS-US computational package. The structures for the R1 and R2 reaction series were obtained using the M11 functional with the cc-pVQZ basis for fluorine and chlorine. For the heavier halogens, bromine and iodine, pseudo-potentials were included for the core electrons and thus the cc-pVQZ-PP basis was used. It was found that at the M11/cc-pVQZ level of theory the $HF+HO_2 \rightarrow H_2O_2+F$ reaction appeared to possess no saddlepoint and the reaction itself was extremely endothermic. Thus, the TS1 "barrier" energy for this reaction was simply set to the zero-point corrected reaction endothermicity and no structure is reported. There were however transition state structures for the R1 reaction where X=Cl, Br and I, as shown in Figure 3.2.

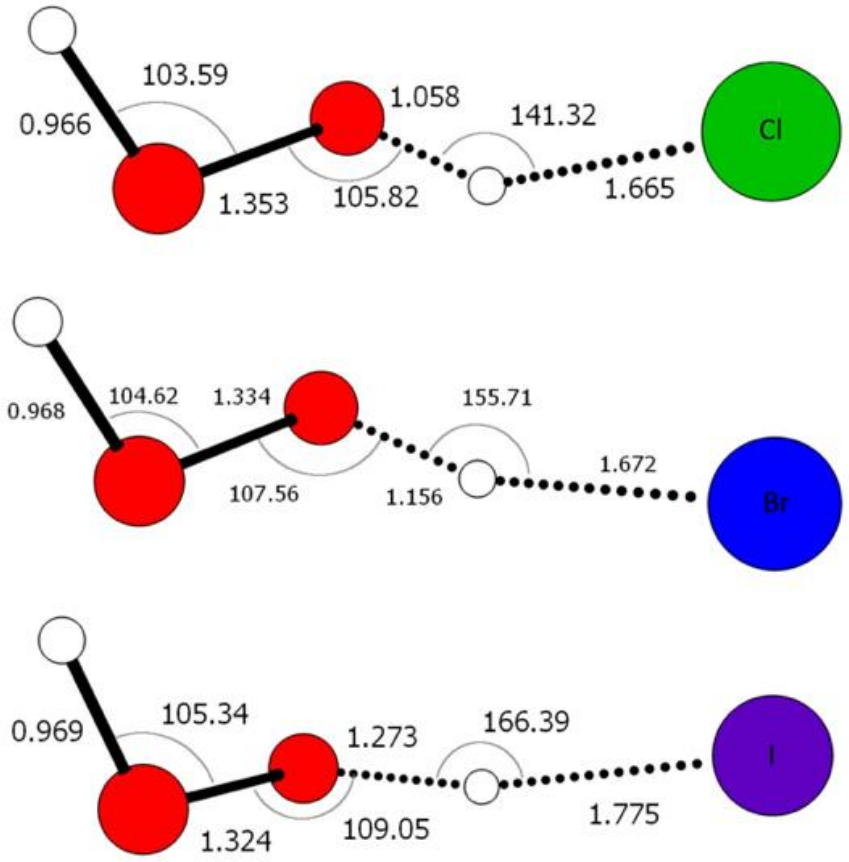

Figure 3.2 The structures of the R1 transition states obtained for the abstraction reactions HX+HO2→X+H2O2. The geometries were optimized using M11/cc-pVQZ-PP (for the X=I, Br) and M11/cc-pVQZ (for X= Cl). Bond distances are in Angstroms and angles are in degrees.

Unlike the R1 series, all four halogens had well defined barriers for the R2 series. The double exchange process of all four halogens were found to proceed through the same type of five membered ring as shown in Figure 3.3, with a pre-reactive complex proceeding the transition state.

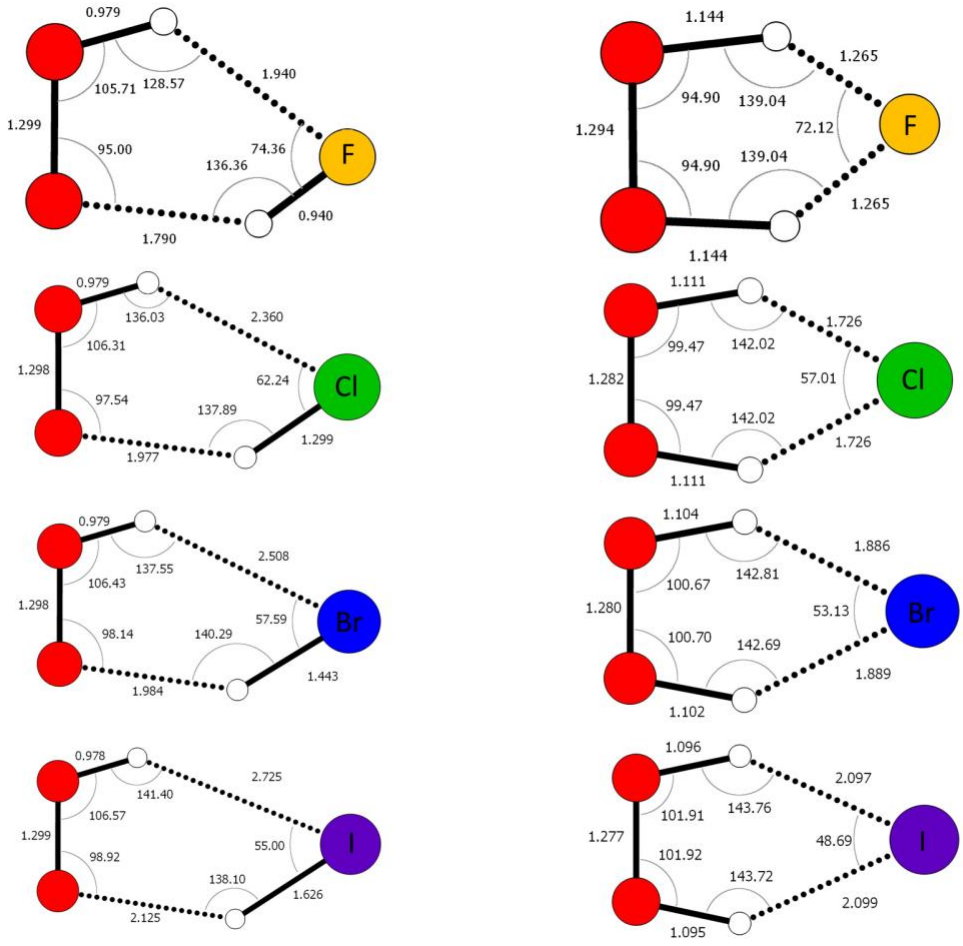

Figure 3.3 The structures of the transition state TS2 (right), and the intermediate complex (left) for the exchange reactions $HX+H'O_2 \rightarrow H'X+HO_2$ with X=F, Cl, Br, I. The geometries were optimized using M11/cc-pVQZ-PP (for the X=I, Br) and M11/cc-pVQZ (for X=F, Cl). Bond distances are in Angstroms and angles are in degrees. The geometry for the X=I case corresponds to the maximum of the adiabatic potential curve which is shifted from the location of the saddlepoint.

Once the optimized structures of the reactants and their corresponding transition state structures were obtained single point energy calculations were performed to obtain the energies of each stationary point at the complete basis set (CBS) limit. The reaction barriers and endo/exothermicities were then calculated relative to the reactants at infinite separation with the CBS limit energies and the frequencies from the M11/cc-pVQZ or M11/cc-pVQZ-PP structures. The reaction energies are tabulated in Table 3.2 and presented in graphical form in Figures 3.4 for R1 and 3.5 for R2.

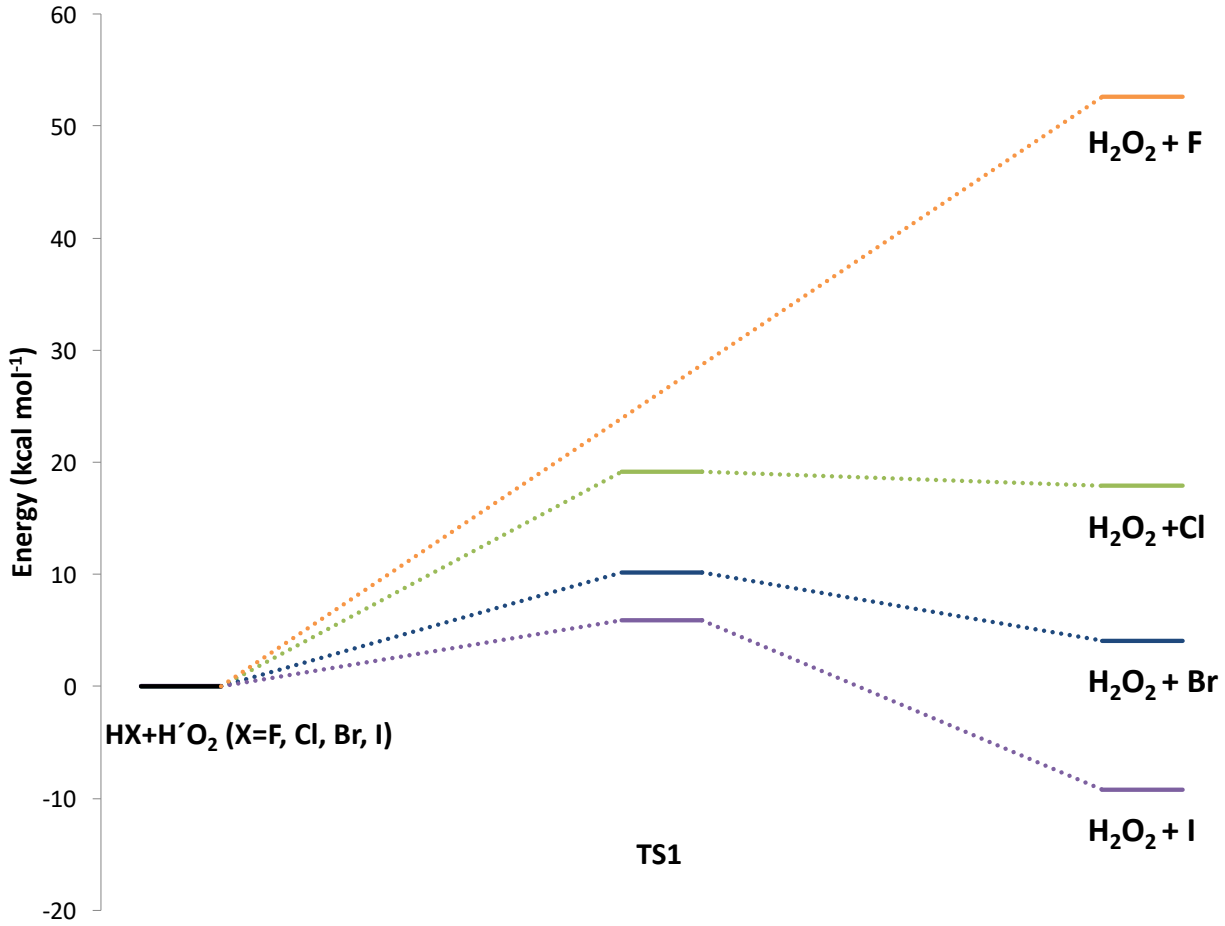

Figure 3.4 Energetics of the abstraction reactions $HX+HO_2 \rightarrow H_2O_2+X$. These energetic values were obtained using M11/CBS/cc-pVQZ-PP (for the X=I, Br) and M11/CBS/cc-pVQZ (for X=F, Cl) employing harmonic zero-point correction.

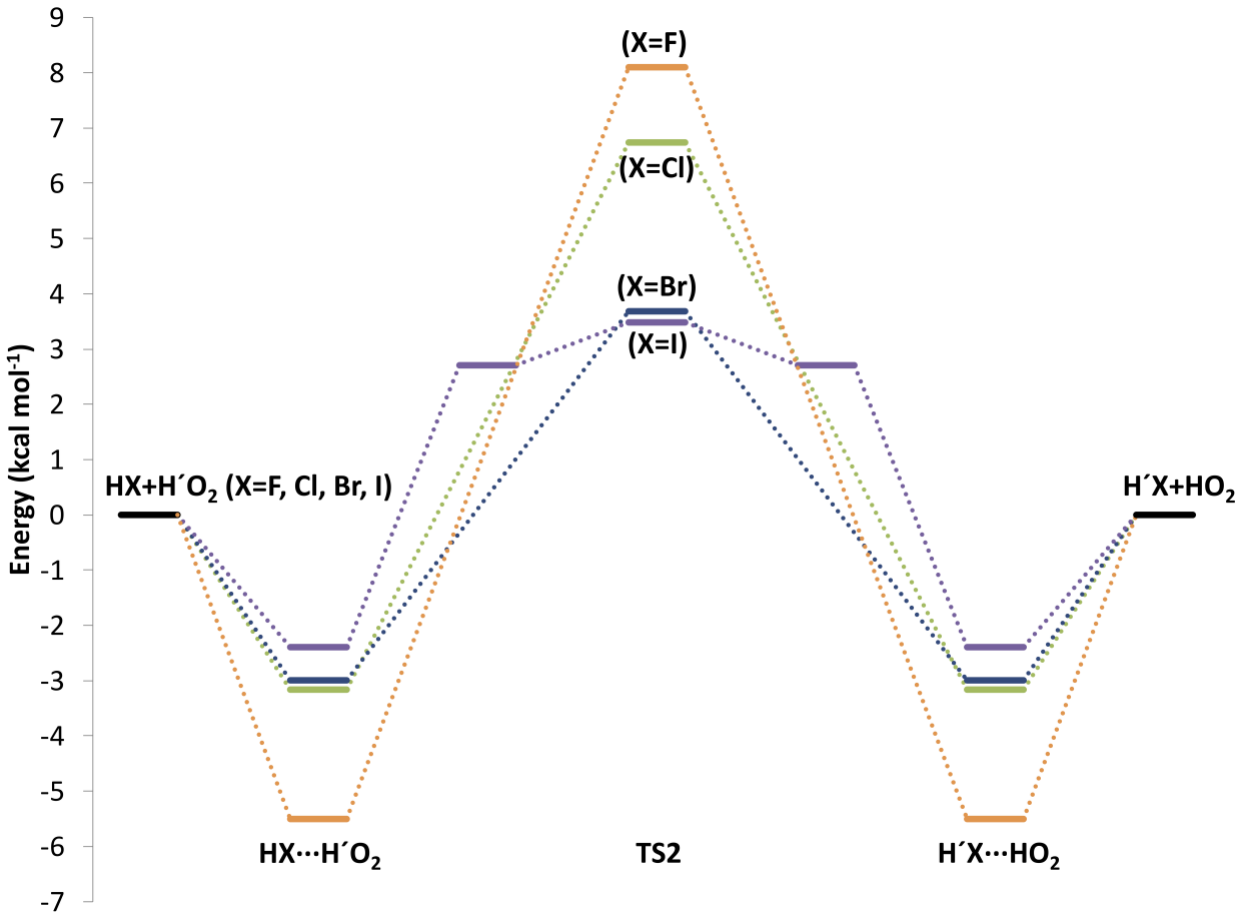

Figure 3.5 Energetics of the exchange reactions $HX+H'O_2 \rightarrow H'X+HO_2$. These energetic values obtained using M11/CBS/cc-pVQZ-PP (for the X=I, Br) and M11/CBS/cc-pVQZ (for X=F, Cl) employing harmonic zero-point correction. Each reaction exhibits stable van der Waals intermediates in the entrance and exit channel.

Table 3.2 The energies of the transition states, TS1(for reaction R1) and TS2 (for reaction R2), and the intermediate complex. These values obtained using the M11/cc-pVTZ structures with a complete basis set extrapolation. The results include harmonic zero point corrections.

ΔE_0(kcal/mol)	Intermediate	TS1	TS2	R1 Products	C_2v Intermediate
HF+HO_2	-5.60	N/A	8.01	52.00	N/A
HF+DO_2	-5.80	N/A	8.32	51.89	N/A
DF+HO_2	-5.96	N/A	7.97	51.55	N/A
DF+DO_2	-6.16	N/A	8.32	51.43	N/A
HCl+HO_2	-3.16	19.15	6.74	17.89	N/A
HCl+DO_2	-3.31	18.98	7.15	17.78	N/A
DCl+HO_2	-3.41	19.15	6.41	17.04	N/A
DCl+DO_2	-3.56	18.98	6.79	16.91	N/A
HBr+HO_2	-2.99	10.16	3.68	4.07	N/A
HBr+DO_2	-3.12	10.00	4.06	3.96	N/A
DBr+HO_2	-3.22	10.44	3.19	3.10	N/A
DBr+DO_2	-3.35	10.28	3.55	2.98	N/A
HI+HO_2	-2.39	5.89	2.71	-9.23	3.48
HI+DO_2	-2.50	5.75	2.81	-9.34	3.83
DI+HO_2	-2.57	6.23	2.66	-10.31	2.87
DI+DO_2	-2.67	6.09	2.76	-10.43	3.20

The TS1 structures for the three halogens with well-defined saddlepoint structures, X=Cl, Br, and I are shown in Figure 3.4. The geometry of the H_2O_2 fragment of TS1 is seen to resemble more closely the nonplanar equilibrium structure of the free H_2O_2 molecule. The HX bond length in the transition state structures was found to elongate with increasing size of the halogen and the weakening of the HX bond. The adiabatic barriers for the R1 abstraction series were found to decrease with the relative strength of the HX bond going from 19.15 kcal/mol for X=Cl to 5.89 kcal/mol for X=I. The enthalpy of the R1 reaction series also changes greatly depending on the halogen, going from being extremely endothermic for X=F to moderately exothermic for X=I. The saddlepoint structures of the R1 series were also chiral with non-superimposable mirror images, which had to be considered when calculating any rate constants.

The saddlepoints of the R2 reaction were found to be highly structured with C_{2V} symmetry. Each of these transition state structures lied in a plane and the X···H···X′ bond angles and lengths were found to be approximately equal. One thing to note is that the saddlepoint of the $HI+HO_2 \rightarrow H_2O_2+I$ reaction was found to bifurcate into twin saddlepoints with a low lying local minimum structure lying between them. On the Born-Oppenheimer surface this structure was found to be 0.23 kcal/mol lower in energy than the twin saddlepoints, however once a zero point correction was included this structure rose 0.78 kcal/mol higher in energy than either saddlepoint and thus acted as the adiabatic barrier for this reaction. Each double exchange reaction also had a pre and post-reactive complex that was formed through hydrogen bonds between the hydrogen halide and hydroperoxy radical. When looking at the transition state structure of the double exchange reactions as the halogen becomes more electronegative, the geometry shifts with the O-H bond elongating and the HOO bond angle decreasing. The barrier energy also increases with electronegativity, with X=F having the largest energy of 8.01 kcal/mol while X=I has the lowest value of 3.48 kcal/mol. The well depth for the pre- and post- reactive complexes likewise become progressively deeper with increasing electronegativity, with the HO_2···HF complex bound most strongly by 5.5 kcal/mol. The HXH bond angle is seen to become quite acute with the heavier halogens with X=I yielding a 49º angle. Normally, one would assume that as the HXH bond angle becomes more acute the resulting strained structure would be less stable and thus have a higher reaction barrier. However the opposite effect was observed, where the system with the most acute bond angle has the lowest reaction barrier.

It is interesting to contrast the reaction barriers obtained for the single H-atom abstraction reactions R1 to those for the double exchange process R2. In Table 3.2 the zero-point corrected barrier heights for TS1 are presented. It is worth noting that the TS1 energies for

$HX+HO_2 \rightarrow H_2O_2+X$ are much higher than the corresponding TS2 values. This is true even for the exothermic X=I case. The exchange TS2 barrier is seen to be lower than the abstraction TS1 barrier even for the endothermic $Br+H_2O_2 \rightarrow HBr+HO_2$ reverse reaction. Clearly the quantum stabilization of the ring shaped TS2 structure promotes the double exchange process compared to the single abstraction reaction.

3.3.2 QTAIM

To help explain the trend in the stabilization of the transition state structures for the exchange reaction the delocalization index was determined using the AIMAll computational program for QTAIM analysis[91], which is reported in Table 5. The $DI(X,A)/2$ value given is half the dissociation index between halogen X and all other atoms of the molecule. $DI(X,A)/2$ can be viewed as the contribution of the halogen to the average number of delocalized electrons between itself and other atoms of the molecule. The sum of each atoms contribution to the average number of delocalized electron $\Sigma DI(A',A)/2$ is also reported. The amount of delocalization, via both measures, for TS2 was found to be greatest for the iodine and bromine systems and follows the trend X = F < Cl < Br ≈ I which is similar to the that for the R2 barrier energies. Thus, even though the larger halogen atoms yield structures with more acute bond angles, the level of electron delocalization actually becomes greater which stabilizes the five-member ring. For comparison, the delocalization index for the R1 reactions were also calculated. Interestingly, there was a trend similar to that of the R2 series with increasing delocalization for larger halogens. The delocalization index for the abstractions reactions, R1, is also reported in Table 3.3. When comparing the amount of delocalization between the R1 and R2 reactions it is clearly seen that the delocalization is greater for the exchange reaction. This result is consistent with the greater

stability of TS2 compared to TS1, and is physically reasonable for a ring shaped structure compared to a linear geometry.

Table 3.3 The delocalization index between the halogen and all other atoms of the molecule, as well as the sum over all atoms for the R1 and R2 reactions. The EA for each halogen atom is reported. The $HF+HO_2 \rightarrow F+H_2O_2$ reaction is not reported since there is no saddlepoint on the M11 PES for that reaction.

		R1		R2	
Species	**Pauling Electronegativity**	$\sum \frac{DI(A',A)}{2}$	$\frac{DI(X,A)}{2}$	$\sum \frac{DI(A',A)}{2}$	$\frac{DI(X,A)}{2}$
F	3.98	N/A	N/A	3.20	0.42
CL	3.16	3.25	0.43	3.51	0.49
BR	2.96	3.46	0.50	3.66	0.53
I	2.66	3.60	0.55	3.67	0.52

Comparisons between and within the R1 and R2 reaction series allowed us to observe how changing the hydrogen donor/acceptor (i.e. the halogen) can affect the relative stability of a transition state as well as role of ring formation. In particular, consider the height of the reaction barriers and amount of electron delocalization as functions of the electronegativity of the halogen. In Figure 3.6 the electron delocalization of the R1 (panel B) and R2 (panel D) versus the Pauling electronegativity (EA) of X is presented. For both reaction series, there is a clear correlation with lower EA halogens giving more delocalization. In panel A and C of Figure 3.6 the barrier heights are also seen to strongly correlate to the EA and the delocalization index, with lower barriers coming from the lower EA halogens. It is possible that similar correlations may be useful in predicting the reactivity of multiple exchange reactions for more general series of homologous reactions.

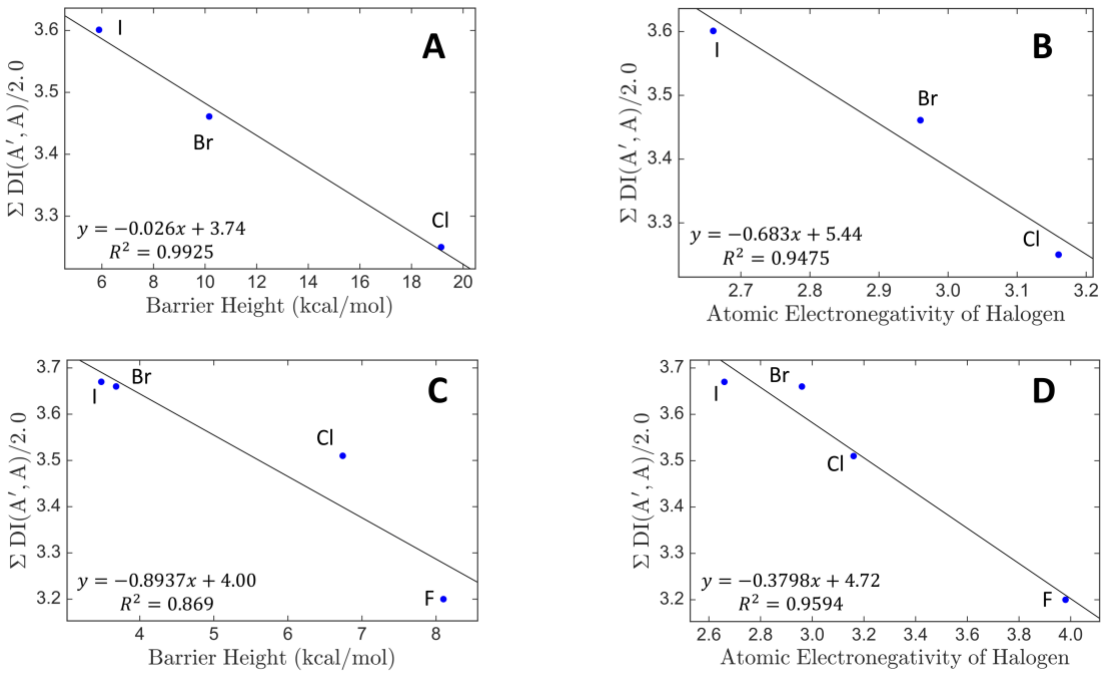

Figure 3.6 Correlation between the total electron delocalization, barrier height and electronegativity. In panels B (R1) and D (R2) the delocalization index is plotted versus EA. In panels A (R1) and C (R2) the delocalization index is plotted versus the barrier height.

3.3.3 Reaction Rate Constants

Thermal rate constants for the R1 and R2 reactions were obtained using transition state theory as described in Section 2.5 with the adiabatic barrier heights presented in Table 3.2. A small-curvature tunneling correction was also calculated using the adiabatic reaction path which was calculated the M11/cc-pVTZ level of theory using the GS2 method described in Section 2.6. The expressions were evaluated over a temperature range of 260-1500K and were fit using a least squares procedure to a sum of two generalized Arrhenius forms.

$$k(T) = A_1 T^{n1} \exp\left(-\frac{E_{A1}}{k_B T}\right) + A_2 T^{n2} \exp\left(-\frac{E_{A2}}{k_B T}\right) \tag{3.3}$$

During this fitting procedure, the data was split in half and each half was fit to a single exponential Arrhenius form, $k(T) = A \exp\left(-\frac{E_A}{k_B T}\right)$. The resulting fitting parameters were then used as initial conditions for fitting to the double exponential form with the *n* factor being set to 1.

The fitting parameters are presented in Tables 3.4 for R1 and 3.5 for R2 are for the SCT tunneling corrected rate coefficients. Only the primary isotope effect for the R1 reaction is considered, whereas for the R2 reaction deuterium labeling on both HO_2 and HX is considered because both hydrogens are involved in the reaction process.

Table 3.4 The least squares fitting of the rate coefficients (including SCT tunneling) for the abstraction reactions R1.

The units are cm^3, kcal/mol, and molecules.

	A_1	n_1	E_{A1}	A_2	n_2	E_{A2}
HCl + HO_2	9.71×10^{-19}	2.00	17.35	3.94×10^{-20}	2.48	20.79
DCl + HO_2	3.14×10^{-17}	1.43	23.58	7.91×10^{-21}	2.64	17.04
HBr + HO_2	9.50×10^{-22}	2.96	7.89	1.64×10^{-22}	3.01	6.11
DBr + HO_2	2.61×10^{-21}	2.81	8.77	1.82×10^{-22}	2.98	6.66
HI + HO_2	4.58×10^{-21}	2.80	4.93	1.25×10^{-21}	2.90	2.98
DI + HO_2	1.18×10^{-20}	2.67	5.49	1.51×10^{-21}	2.82	3.43

Table 3.5 The least squares fitting of the rate coefficients (including SCT tunneling) for the exchange reactions R2.

The units are cm^3, kcal/mol, and molecules.

	A_1	n_1	E_{A1}	A_2	n_2	E_{A2}
HF + HO_2	1.57×10^{-20}	1.83	4.10	1.28×10^{-26}	3.75	0.98
DF + HO_2	2.82×10^{-23}	2.75	3.46	1.22×10^{-28}	4.23	1.07
HF + DO_2	4.19×10^{-22}	2.39	4.10	3.92×10^{-28}	4.13	1.53
HCl + HO_2	3.70×10^{-23}	2.81	2.68	1.14×10^{-09}	-1.77	7.14
DCl + HO_2	1.03×10^{-17}	1.28	12.50	3.04×10^{-21}	2.20	3.48
HCl + DO_2	7.74×10^{-17}	1.05	13.60	1.18×10^{-20}	2.03	4.33
HBr + HO_2	4.01×10^{-19}	1.71	7.49	2.90×10^{-19}	1.60	1.20
DBr + HO_2	2.50×10^{-21}	2.31	3.85	8.73×10^{-18}	1.07	1.57
HBr + DO_2	1.94×10^{-20}	2.07	5.55	7.14×10^{-18}	1.14	2.35
HI + HO_2	1.29×10^{-18}	1.57	7.77	9.52×10^{-19}	1.44	1.38
DI + HO_2	2.25×10^{-21}	2.31	3.86	2.17×10^{-18}	1.27	1.08
HI + DO_2	-1.63×10^{-11}	-0.89	7.81	1.08×10^{-21}	2.37	0.88

The results versus temperature for R1 and R2 reaction series for X=F, Cl, Br, I are illustrated over a wide temperature range in Figures 3.7 and 3.8 and the values for T=298 K are tabulated in Table 3.6.

Table 3.6 The rate coefficients and tunneling transmission coefficients for the R1 and R2 reactions computed at T=298 K.

	R1			**R2**		
Species	κ_{SCT}	k^{TST}	$\kappa_{SCT}k^{TST}$	κ_{SCT}	k^{TST}	$\kappa_{SCT}k^{TST}$
F	N/A	N/A	N/A	28.09	1.89×10^{-19}	5.30×10^{-18}
Cl	1.80	9.62×10^{-27}	1.73×10^{-26}	3.69	1.07×10^{-18}	3.94×10^{-18}
Br	6.00	3.22×10^{-20}	1.93×10^{-19}	2.21	1.55×10^{-16}	3.42×10^{-16}
I	3.05	4.45×10^{-17}	1.36×10^{-16}	1.75	1.97×10^{-16}	3.45×10^{-16}

In Figures 3.7 and 3.8 the role of tunneling is emphasized by plotting both the NT and SCT result for each case. For the abstraction process the role of tunneling is seen to be proportional to the imaginary frequency of the barrier where the frequencies for X=Cl, Br and I were 1120.2 cm^-

[1], 1867.6 cm^{-1}, and 1536.3 respectively. The rates constants for the R1 reaction series were also found to increase for the heavier halogens due to the decreasing height of the reaction barrier. For the R2 reactions, it is seen that the reactions for X=Br and I proceed at a modest rate of 3.5 x 10^{-16} cm^3/sec at T=298 K. The reactions for X=Cl and F are roughly two orders of magnitude slower due to the higher barrier height. However, it is worth noting that the tunneling coefficient for the HO_2+HF case is quite large, $\kappa_{SCT}(T)$=28.09 at 298K. At higher temperatures the exchange reaction becomes facile in all cases.

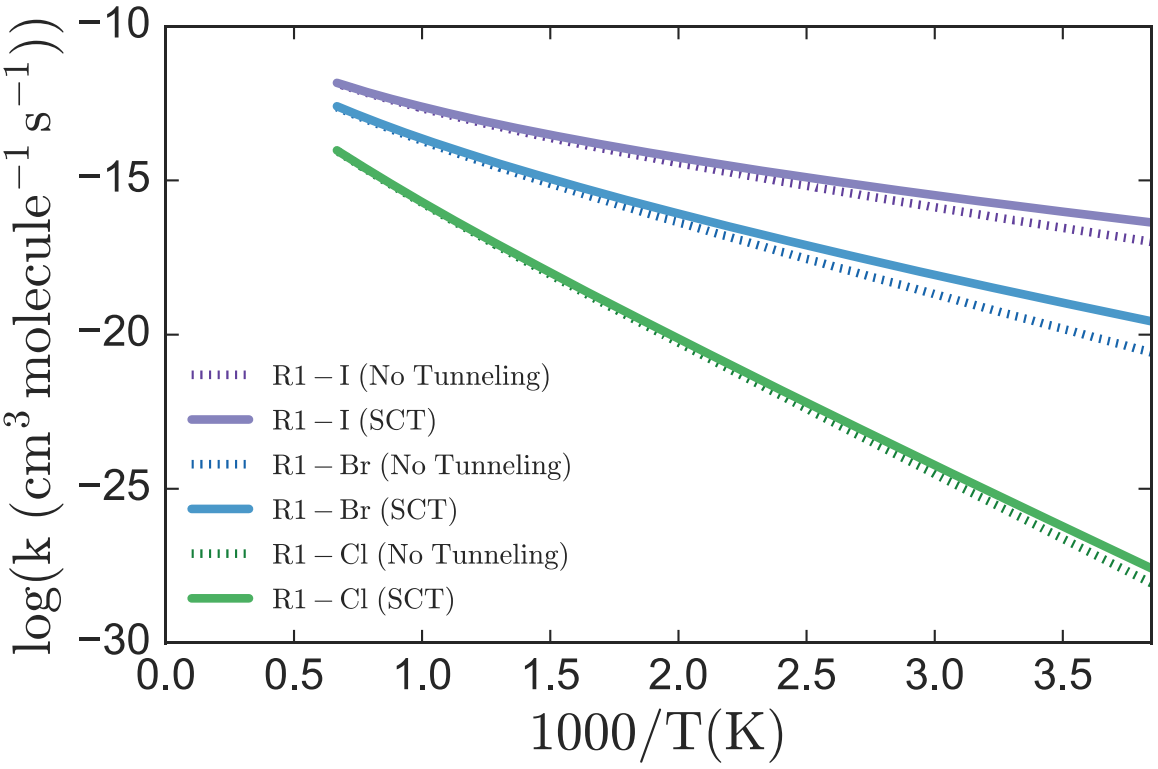

Figure 3.7 The rate coefficient versus temperature for the abstraction reaction HX+H'O2→H_2O_2+X for X=Cl, Br, I. The results obtained using the NT approximation, κ=1, and the SCT approximation, κ_{SCT}, are both shown for each case in order to emphasize the role of quantum tunneling.

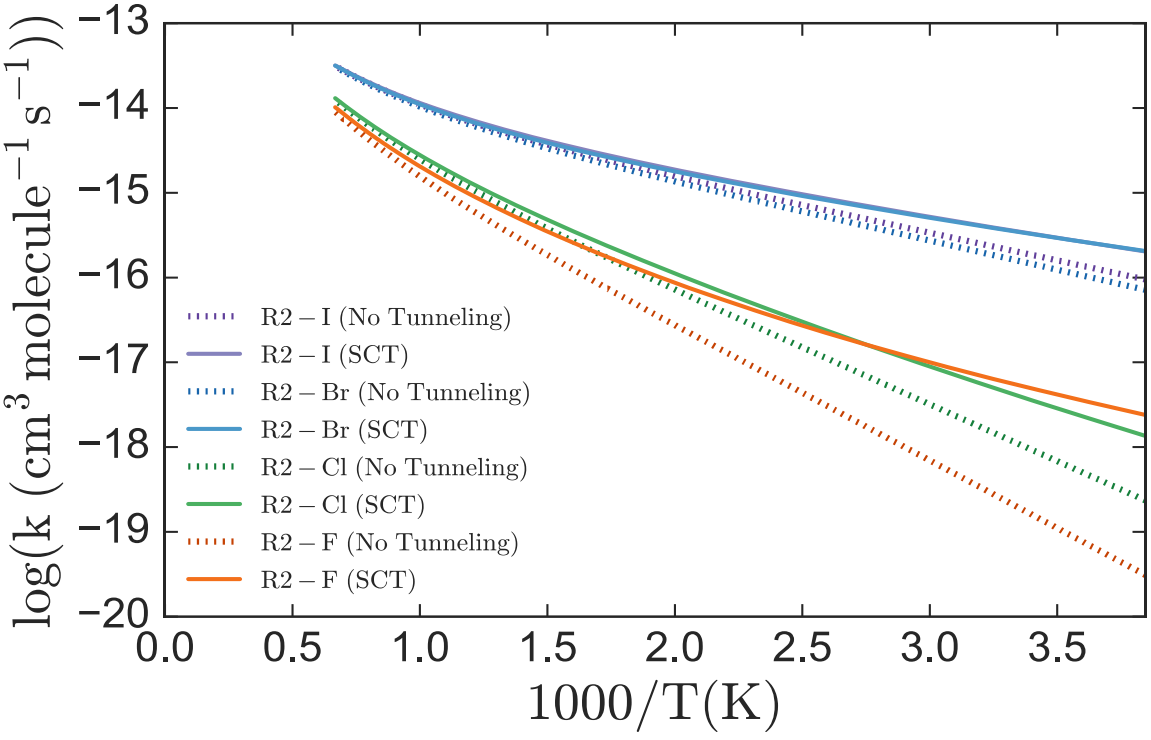

Figure 3.8 The rate coefficient versus temperature for the exchange reaction HX+H'O_2→H'X+HO_2 for X=F, Cl, Br, I. The results obtained using the NT approximation, κ=1, and the SCT approximation, κ_{SCT}, are both shown for each case in order to emphasize the role of quantum tunneling.

While the lower barrier energies clearly favor the double exchange process, the less constrained geometry of the R1 transition state tends to enhance the abstraction process through a higher entropy of activation. The normal mode frequencies for the stationary points are presented in Appendix C.1. When considering the X=Br case as an example, the lowest TS1 normal mode frequencies are 139.6, 297.5, and 350.1 cm^{-1} while those for TS2 are 337.8, 776.3, and 994.7 cm^{-1}. In addition to TS1 being a looser transition state, the rotational constant for TS1 is also smaller due to the extended geometry. Thus, there is roughly an order of magnitude difference in the pre-exponential factors between reactions R1 and R2 due to the entropic effects. To illustrate the

competition between energetic and entropic effects, the rate coefficients for R1 and R2 plotted together for X=I, Br, and Cl in Figure 3.9. At low temperatures the exchange processes are strongly favored due to the lower transition state barrier. However, at higher temperatures the entropic effects take over and abstraction reactions begin to dominate in all cases. The crossover temperature between when the abstraction and exchange reactions dominate is found to trend with the barrier height of the reaction. For example, in the case of X=I where the reaction barriers for R1 and R2 are similar in magnitude the crossover temperature is much lower than that of X=Cl which has a large difference in the reaction barrier energies.

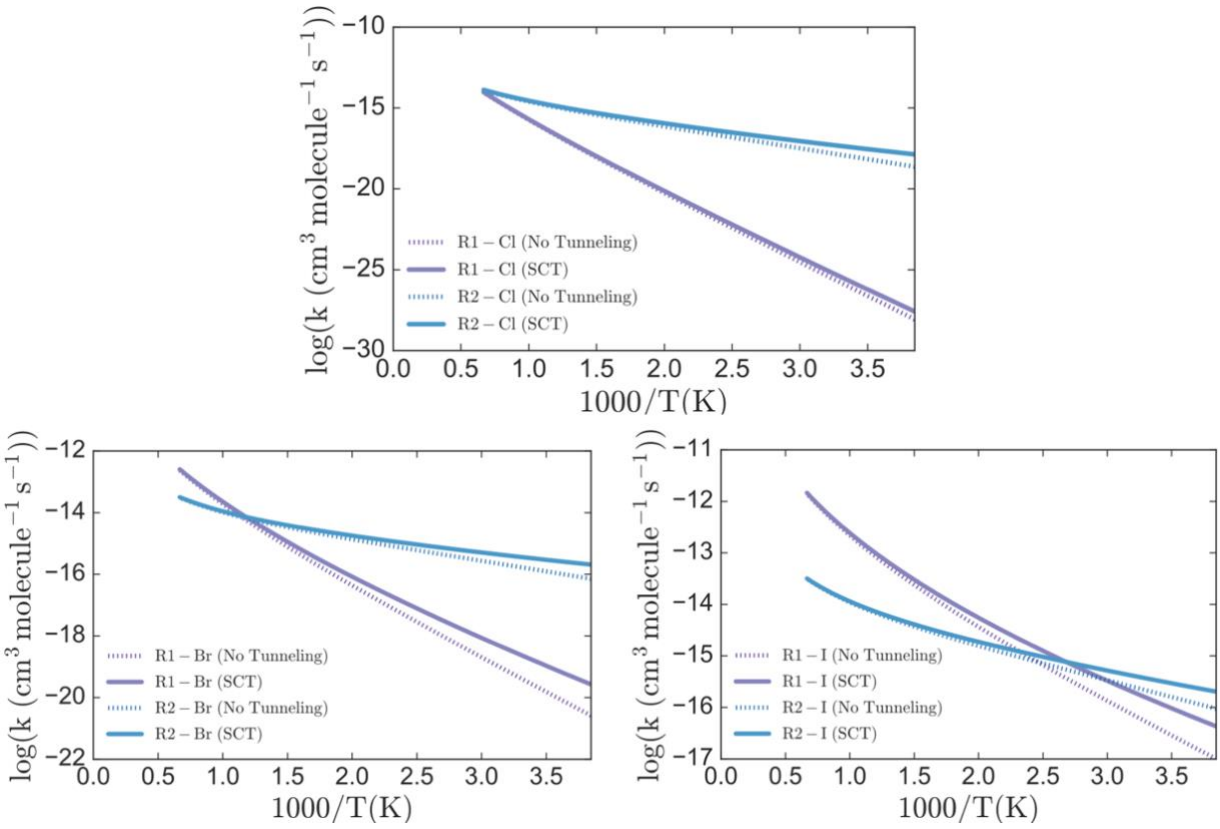

Figure 3.9 The rate coefficients for reactions R1 and R2 for X=I, Br, and Cl. The tunneling was included using the SCT method in each case. It is seen that reaction R2 dominates at low temperature due to its lower activation barrier, but that reaction R1 becomes progressively more important at higher temperatures due to entropic effects.

It is worth noting that although the HI+HO_2 abstraction process is faster than the reactions of X=Cl,Br each of these reactions are slower than their hydroxide radical counterparts of OH+HX. Experimental estimates for the OH+HX rate constants at T=298K where X=Cl,Br, and I are $7.86x10^{-13}$ molecule cm^3 s^{-1}, 1.1 $x10^{-11}$ molecule cm^3 s^{-1} and $7.00x10^{-11}$ molecule cm^3 s^{-1}, respectively.[96] In the presence of OH, the chlorine and bromine abstraction reactions with HO_2 are unlikely to play a significant role at low temperatures. However, because HO_2 is more abundant in the troposphere than that of OH, the faster HI+HO_2 abstraction process could play a small role as a secondary source in halide production. Under combustion settings reactions with both radicals are likely to play roles in the production of halides in the presence of HX. Ultimately these reaction coefficients can be useful in modeling halide reactions in both atmospheric and combustion settings.

3.3.4 Kinetic Isotope Effect

Using the small-curvature rate coefficients obtained for both the abstraction and exchange reactions the kinetic isotope effect (KIE) from deuterium substitution was computed.

$$KIE = \frac{k^{SCT}(\mathrm{H'X + HO_2})}{k^{SCT}(\mathrm{DX + HO_2})} \tag{3.4}$$

The value of the KIE for the R1 and R2 reactions are plotted versus temperature in Figures 3.10 and 3.11, and values at T=298 K are tabulated in Table 3.7. In the R2 reaction series, except for the case of X=F, the KIE is seen to be quite modest. The substitution H→D lowers the TS2 barriers by a small amount thus tending to decrease KIE slightly. On the other hand, the substitution has a larger impact on the tunneling coefficient. Since only for the X=F case does tunneling play a large role in the reaction, it is understandable that the KIE is largest for this halogen.

Unlike the R2 reactions, the KIE was found to be significant for each reaction of the R1 reaction series. The largest impact from deuterium substitution on the hydrogen halide was from the thermal rate constants which were found to decrease due to larger reaction barriers. The increased barrier heights were found to decrease the thermal rate constant for each reaction by a factor of 2-3 with the effect increasing from X=Cl to X=I. The change in the tunneling factors for the R1 series were found to be small upon deuterium substation with virtually no difference between the effect found for X=Cl and X=Br. However, it is worth noting that due to the slowly increasing barrier height upon deuterium substation going from X=Cl to X=I, the iodine system was found to have slight increase in tunneling when substituted despite the heavier isotope.

Table 3.7 Kinetic isotope effect at 298K for the R1 and R2 reactions. The contribution from both the conventional rate constant as well as the transmission coefficient are presented.

	R1			**R2**		
$\frac{HX}{DX}$	$\frac{\kappa_H}{\kappa_D}$	$\frac{k_H^{TST}}{k_D^{TST}}$	$\frac{k_H^{SCT}}{k_D^{SCT}}$	$\frac{\kappa_H}{\kappa_D}$	$\frac{k_H^{TST}}{k_D^{TST}}$	$\frac{k_H^{SCT}}{k_D^{SCT}}$
F	N/A	N/A	N/A	2.61	1.79	4.67
Cl	1.07	1.87	2.00	1.59	1.06	1.69
Br	1.06	2.84	3.00	1.52	0.81	1.22
I	0.96	2.93	2.80	1.09	0.64	0.70

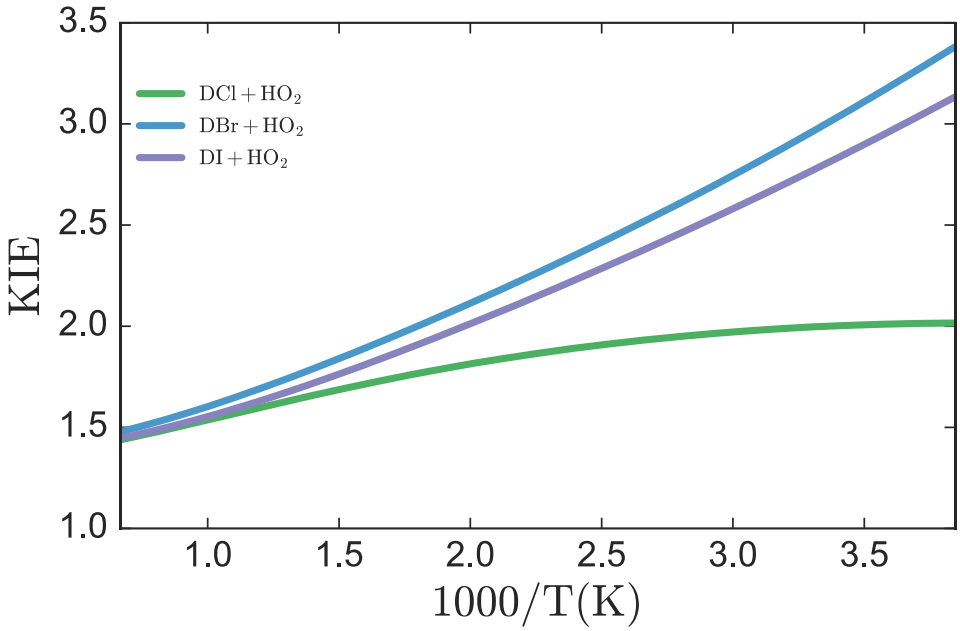

Figure 3.10 The kinetic isotope effect (KIE) for the R1 reaction. Each systems system exhibits a modest isotope effect with the effect being largest for X=I due to the increased reaction barrier.

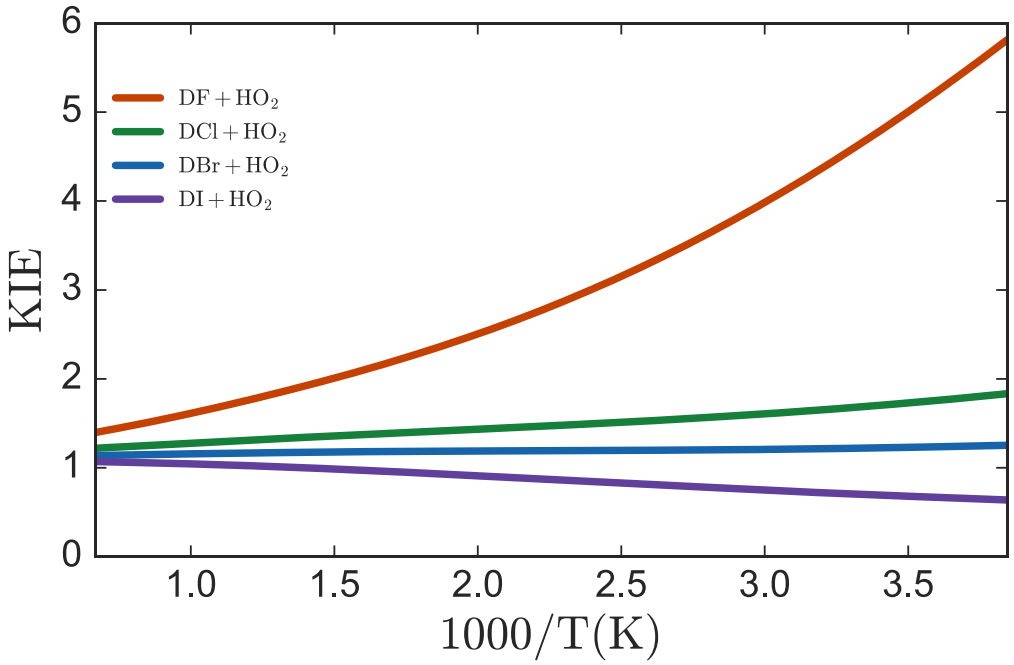

Figure 3.11 The kinetic isotope effect (KIE) for the R2 reaction. The fluorine system exhibits the greatest isotope effect in the halogen series due largely to the suppression of tunneling for the heavier D-atom.

3.4 Conclusion

In this work, a novel double exchange reaction between hydrogen halides and HO_2 radicals was found and characterized. This work shows that HO_2 radicals can serve as catalysts for these double hydrogen exchange reactions. This extends previous studies of da Silva[30] and Karton[28] who observed similar behavior for other reaction classes. In the present study, the concerted exchange reactions occur through five-member cyclic transition states and exhibited much lower activation barriers than the single H-atom abstraction reactions. However, the abstraction reactions have looser transition states and thus possess pre-exponential factors in the rate coefficients which are approximately an order of magnitude larger than those for the exchange reactions. As a result of this competition between energetic and entropic effects, the exchange rates dominate at low temperatures and the abstraction reactions can become larger at high temperatures. The stabilization of the cyclic TS2 transition state is consistent with similar effects observed in other multiple H-atom transfer reactions.

One interesting effect noted was the somewhat anomalous role of ring strain. The progression of exchange reactions with X=F, Cl, Br, I showed TS2 structures with more acute HXH bond angles. This would naively suggest more ring strain and higher barrier heights. However, the barriers actually become progressively more stabilized in this series. To rationalize this behavior, the role of electron delocalization was investigated. It was found that the electron delocalization index progressively increased through the series X=F, Cl, Br, I. This delocalization effectively stabilized the TS2 even though the geometry was unfavorable. The degree of electron delocalization was found to track well with the electronegativity of the halogen species. It is possible that more general multiple exchange reactions may follow a similar pattern. This could have general significance since it important to understand the factors that control barrier lowering

for these concerted processes. Finally, the role of tunneling was assessed using the SCT method. The tunneling proved to be a dominate effect only for the X=F exchange reaction where $\kappa_{SCT}(298K)$ =28.09. Although one might expect that tunneling would be more prominent for the heavier species X=I or X=Br since they possess a more extreme heavy-light-heavy mass ratio, this effect is negated by their much wider adiabatic potential barriers. Also, although the R1 reactions are slower than their counterparts of HX with OH, the HO_2+HI reaction could still act as a secondary source of halides in the troposphere. These rate coefficients will be also useful for accurate modeling of atmospheric and combustion systems.

Chapter 4

Abstraction and Exchange Reactions of Pyruvic Acid

4.1 Introduction

4.1.1 Pyruvic acid and OH

Organic molecules have been found to play large roles in atmosphere chemistry, especially in regard to pollutants and aerosols. [116] [117] [118] [119] [120] Volatile organic compounds (VOC) are a specific class of organics which have been found in large concentrations in the troposphere. These organics have been linked to secondary organic aerosol formation (SOA) as well as smog and haze formation when hydroxyl radicals are available.[38] [39]

These organic aerosols have also been shown to be a potential health hazard to people, with the aerosols negatively affecting the cardiovascular and respiratory systems in humans.[121] [122] Many VOCs are removed from the atmosphere primarily through reactions involving hydroxyl radicals. However, there are cases where direct photolysis is the primary reaction pathway for removal of a VOC in the atmosphere. Photolysis typically acts as the primary path when VOC compounds have both a poor oxidation rate by OH as well as strong absorption features in the UV-vis region, as is the case for some carbonyl containing compounds.[123] [124] [125] For these types of systems, reactions with OH merely act as a secondary sink. Pyruvic acid displays both of these characteristics and is also one of the most abundant keto-acids found in the troposphere. Pyruvic acid is formed as an intermediate molecule in the isoprene oxidation pathway.[31] [32] Isoprene is a biologically produced VOC, which has an estimated emission rate of 500 Tg carbon per year out of the approximate 1300 Tg of carbon produced each year by worldwide.[126] [127] [128] [129] Pyruvic acid has been found in the troposphere over several different types of climates such as mid-latitude, tropical and marine

environments with large gas phase mixing ratios up to 100 ppt.[33 34 35 36 37] It has also been found in several different mediums, including the gas phase, rainwater, aerosols, and snow.[130 131 132 133 134 135 136] Experimental studies on the molecule have suggested that direct photolysis is the primary pathway for degradation in the troposphere rather than that of OH oxidation. Reed Harris *et al.* have obtained experimental photolysis rate coefficients for both gas and aqueous phases of the molecule.[38 39] These authors found that the loss through OH oxidation was not competitive with that of photolysis and by using the experimental work by Mellouki and Mu, they suggest that loss through OH oxidation was up to two orders of magnitude slower than that of photolysis.[40 41]

4.1.2 Pyruvic acid and HO_2

Experimental studies performed by Reed Harris *et al.* have suggested that the primary channel for the photolysis of pyruvic acid proceeds through a decarboxylation pathway forming methylhydroxycarbene and CO_2 initiated by hydrogen transfer between the carboxylic acid and central carbonyl oxygen.[38 39 40] This high energy carbene product eventually leads to acetaldehyde through isomerization. This reaction pathway has also been studied on the ground state surface by da Silva and Takahashi *et al.*

Takahashi *et al.* studied the effect of vibrational OH overtone pumping on the formation of the carbene product. [137] da Silva on the other hand studied many of the possible unimolecular reaction pathways for pyruvic acid on the ground state. [138] Many of these unimolecular reactions studied by da Silva and Takahashi *et al.* involve hydrogen transfer. It was thought that HO_2 would be able to mediate the hydrogen transfer process and lower the reaction barriers, similar to the reactions of HO_2+HX (X=F, Cl, Br, and I) presented in Chapter 3 of this thesis.

4.2 Computational Methods

The zero point and CBS limit energies were used to calculate the zero point corrected (i.e. adiabatic) barrier and the exo/endo-thermicity for each reaction. The CBS limit energies were obtained using both M11/cc-pVnZ as well as CCSD(T)/cc-pVnZ where n=(D,T,Q) with optimized structures and frequencies obtained using M11/cc-pVTZ.

In order to test the validity of the methodology used to study pyruvic acid, both the M11/CBS and CCSD(T)/CBS methods were used to study the abstraction reactions of acetic acid. There are two major conformers of pyruvic acid in the gas phase, a trans-cis (Tc) conformer where the acid hydrogen is cis to the central carbonyl oxygen and a trans-trans (Tt) conformer where the hydrogen is trans to the central carbonyl oxygen. Acetic acid was chosen because it has similar structural characteristics with the Tt conformer of pyruvic acid, where the hydrogen of the carboxylic acid function group points toward the carbonyl oxygen of the acid. All three of these structures are presented in Figure 4.1.

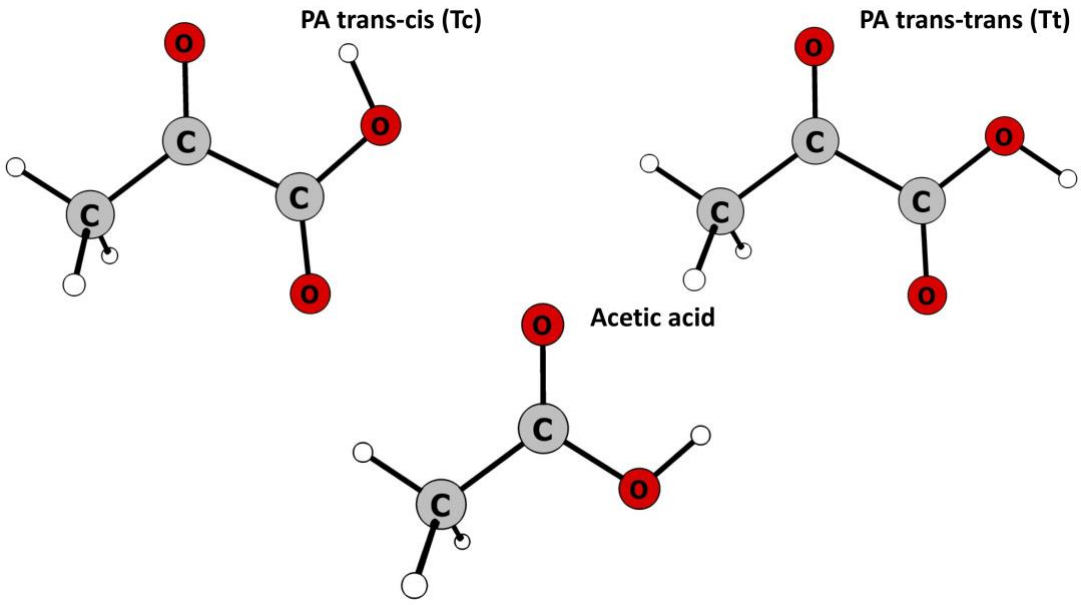

Figure 4.1 Stationary point structures for the trans-cis (Tc) and trans-trans (Tt) conformers of pyruvic acid as well as acetic acid. These structures were obtained using M11/cc-pVTZ.

The chemistry for both acetic acid and pyruvic acid were thought to be similar because each molecule has both methyl and carboxylic acid functional groups which can undergo abstractions by OH. Acetic acid also has multiple energetic values in the literature which the present methodology can be compared to. The methyl and carboxylic acid abstractions of acetic acid are labeled R1 and R2 respectively. The literature values used for comparison were taken from the papers of Rosado-Reyes *et al.*[139] and De Smedt *et al.*[140] and are presented in Table 1.

$$R1 - Acetic: CH_3COOH + OH \rightarrow CH_2COOH + H_2O \quad (4.1)$$

$$R2 - Acetic: CH_3COOH + OH \rightarrow CH_3COO + H_2O \quad (4.2)$$

Table 4.1 Energetics in for the reactions of Acetic acid + OH calculated using M11/CBS and CCSD(T)/CBS. The units of the reported energetics are in kcal/mol.

	CCSD(T)/CBS	M11/CBS	Rosado-Reyes *et al.*[139]	De Smedt *et al.*[140]
PRC1(AA)	-4.73	-4.89	-4.40	-5.10
PRC2(AA)	-6.18	-7.27	-6.50	-7.30
TS1(AA)	3.47	3.59	4.00	4.00
TS2(AA)	1.82	2.31	2.10	1.60

The results of Table 4.1 show that both the M11 functional as well as CCSD(T) give results that are in relatively good agreement with values found in literature for both the pre-reactive complex and adiabatic barrier for both the methyl and acid abstraction reactions of acetic acid. Compared to the literature values for the acetic acid abstraction reaction, the M11 functional predicted a higher adiabatic barrier than the literature values for the acetic acid abstraction reaction, with a 0.71 kcal/mol increase over the value reported by De Smedt *et al.* and a 0.21 kcal/mol increase of Rosado-Reyes *et al.*[139 140] The Minnesota functional also predicted an acid pre-reactive complex (PRC2) well depth closer to that of the value reported by De Smedt *et al.* CCSD(T) on the other hand predicated an adiabatic reaction barrier 0.28 kcal/mol lower than the value of

Rosado-Reyes *et al.* and 0.22 kcal/mol higher than De Smedt *et al.* as well as a well depth closer to the value reported by Rosado-Reyes *et al.* When comparing the methyl abstraction reaction energetics obtained using M11 and CCSD(T) to the previously reported literature values, both the Minnesota functional and CCSD(T) predict slightly lower reaction barriers when compared to the literature value of 4.00 kcal/mol reported by both Smedt and Rosado-Reyes with values of 3.47 kcal/mol and 3.59 kcal/mol respectively. For the pre-reactive complex near the methyl functional group (PRC1), both methods also predict a well depth between those of De Smedt *et al.* and Rosado-Reyes *et al.* with M11 predicting a slightly lower well depth than that of CCSD(T) with values of -4.89 kcal/mol to -4.73 kcal/mol respectively. For the acid and methyl abstraction reactions the M11 functional tends to predict higher reaction barriers and deeper wells for the pre-reactive complexes. Because neither the M11 functional or CCSD(T) appeared to have a clear advantage over the other method both were used to calculate the energetics of each reaction.

4.3 Results

4.3.1 Reaction Energetics of OH with Pyruvic Acid

The optimized transition state structures belonging to the reactions of pyruvic acid with OH were obtained using M11/cc-pVTZ and are shown in Figure 4.2. There are two transition state conformers per type of reaction with each resembling either the Tt or Tc conformer of pyruvic acid.

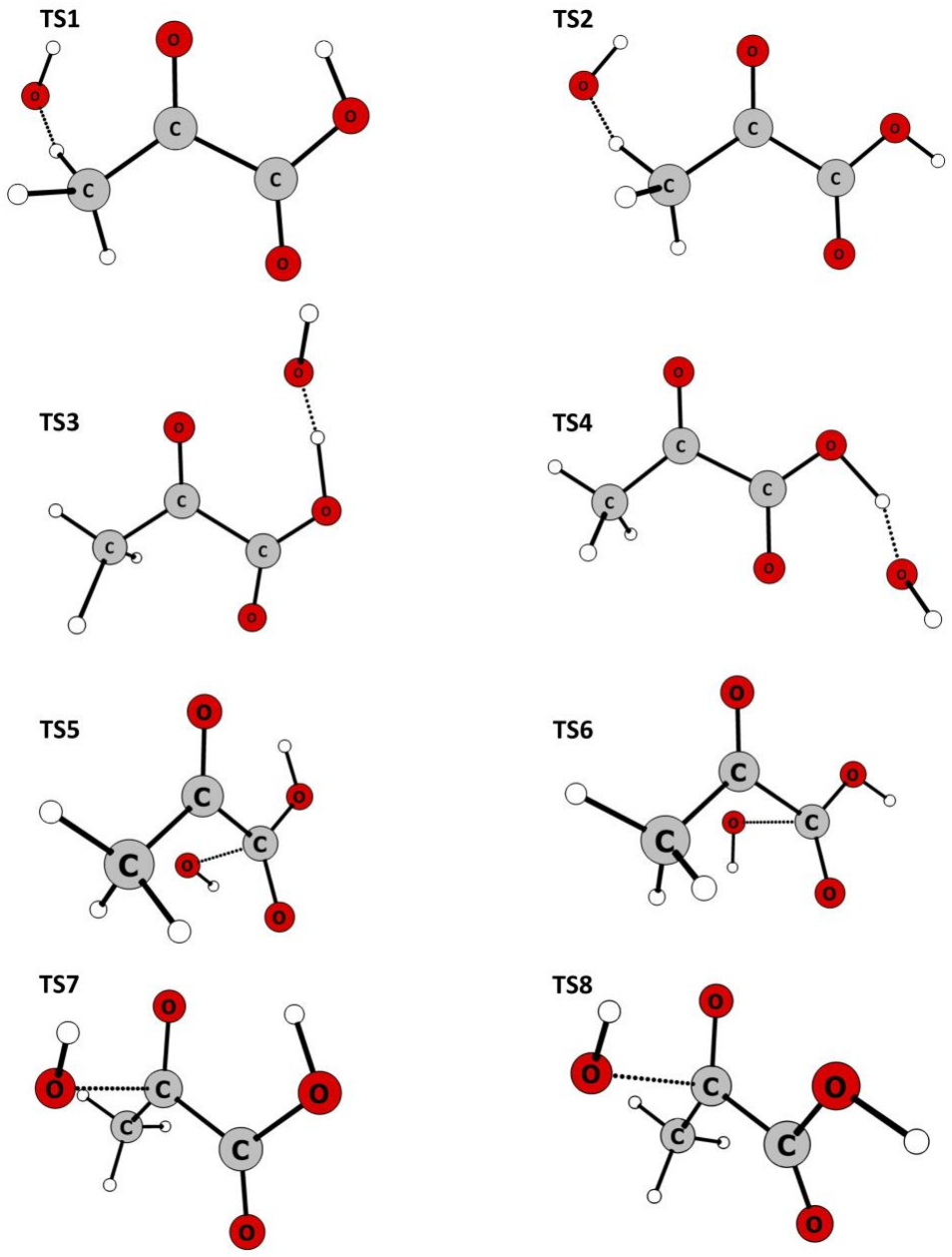

Figure 4.2 Transition state structures obtained using M11/cc-pVTZ for the OH+PA reactions. TS1, TS3, TS5, and TS7 originate from the Tc conformer of pyruvic acid and TS2, TS4, TS6, and TS8 originate from the Tt conformer of pyruvic acid.

Reactions 1 and 2 are hydrogen abstraction reactions of the methyl group. Reactions 3 and 4 correspond to the hydrogen abstraction of the carboxylic acid. Reactions 5 and 6 are OH additions to the carboxylic acid carbon and reactions 7 and 8 are OH additions to the central carbonyl carbon.

$$R1: CH_3COCOOH + OH \rightarrow (CH_2COCOOH)_{Tc} + H_2O \quad (4.3)$$

$$R2: CH_3COCOOH + OH \rightarrow (CH_2COCOOH)_{Tt} + H_2O \quad (4.4)$$

$$R3: CH_3COCOOH + OH \rightarrow (CH_3CO)_{Tc} + H_2O + CO_2 \quad (4.5)$$

$$R4: CH_3COCOOH + OH \rightarrow (CH_3CO)_{Tt} + H_2O + CO_2 \quad (4.6)$$

$$R5: CH_3COCOOH + OH \rightarrow (CH_3COCO(OH)_2)_{Tc} \quad (4.7)$$

$$R6: CH_3COCOOH + OH \rightarrow CH_3CO + H_2CO_3 \quad (4.8)$$

$$R7: CH_3COCOOH + OH \rightarrow CH_3COOH + HCOH \quad (4.9)$$

$$R8: CH_3COCOOH + OH \rightarrow (CH_3CO(OH)COOH)_{Tt} \quad (4.10)$$

The transition state structures for the odd numbered reactions have a similar structure to the Tc conformation of PA whereas the even numbered reactions correspond to a Tt conformation of the transition state. The Tc conformation of pyruvic acid was found to be lower in energy than the Tt conformation by 2.87 kcal/mol at the M11/CBS level and 2.64 kcal/mol at the CCSD(T)/CBS level. The energy difference between these two conformers is primarily caused by additional intramolecular hydrogen bonding between the hydrogen of the carboxylic acid and the central carbonyl oxygen found only in the Tc conformer.

When looking at the transition state structures for the abstraction reactions between OH and pyruvic acid, it was found that there are structural similarities to the abstraction reactions between hydroxyl radicals and acetic acid. In both acetic acid and pyruvic acid, the methyl abstraction transition state has additional hydrogen bonding with a nearby carbonyl oxygen. The transition state structures for the abstraction of the carboxylic acid also have structural similarities, in both cases the hydroxyl radical hydrogen points out of the molecular plane.

Optimized structures for the pre-reactive complexes were obtained in order to determine if there was any negative temperature dependence. The optimized structures are shown in Figure 4.3.

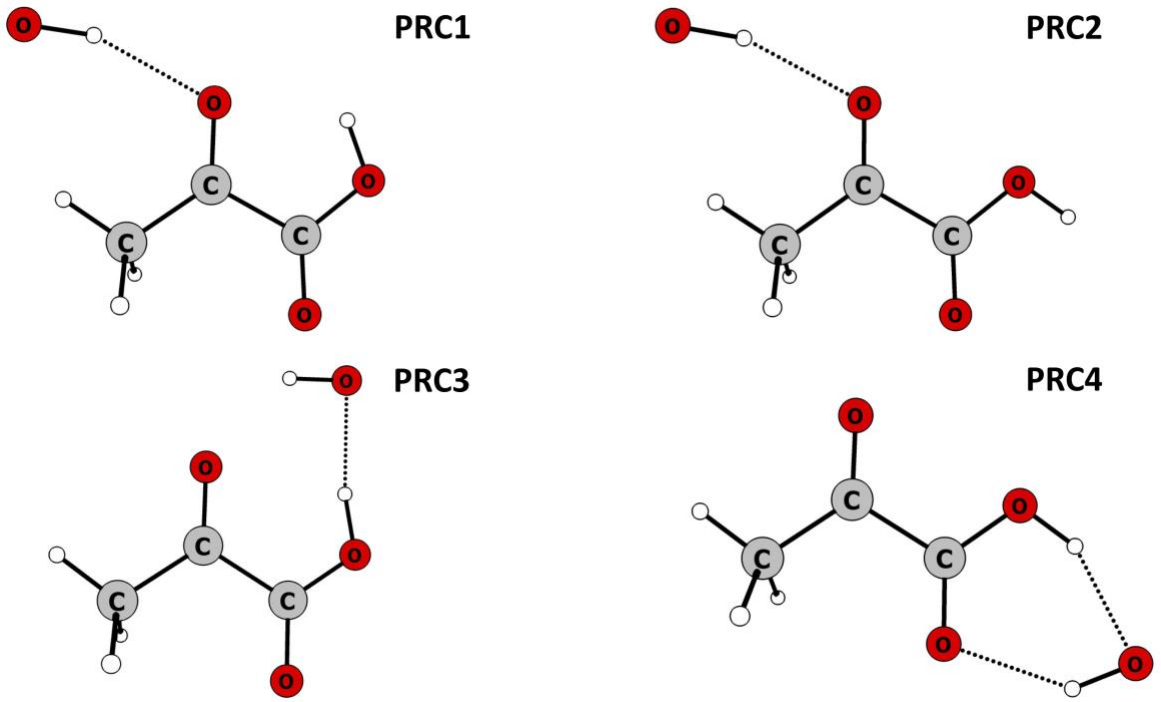

Figure 4.3 Pre-reactive complex structures obtained using M11/cc-pVTZ for the OH+PA reactions.

Two pre-reactive complexes near the methyl functional group, PRC1 and PRC2, only differ in the placement of the carboxylic acid hydrogen. In these structures the hydroxyl radical is hydrogen bound to the central carbonyl oxygen on the side of the methyl group. Both of these structures are very similar to the pre-reactive complex of acetic acid, as shown in the papers of Rosado-Reyes *et al.* and Smedt *et al.*[139 140]

In both PRC3 and PRC4, the hydroxyl radical forms a planar ring type structure between the carboxylic acid hydrogen and a carbonyl oxygen. The major difference between these two structures is which carbonyl oxygen is used in the ring formation. The pyruvic acid molecule in the PRC3 complex is in the Tc conformation, and thus the central carbonyl oxygen is used during

complex formation. On the other hand, the pyruvic acid molecule in the PRC4 complex is in the Tt conformation and thus the carbonyl oxygen of the carboxylic acid is used in complex formation.

When comparing the energetics of the pre-reactive complexes, PRC3 and PRC4 were found to have deeper wells than PRC1 and PRC2. The increased well depth can be ascribed to the stabilizing effect of ring formation. The complexes for R1 and R2 were found to have a similar well depth, with both DFT and CCSD(T) methods predicting less than a kcal/mol difference in energy. This makes sense due to the similarity between the two structures, with the only major structural change being the position of the acid hydrogen away from the reaction. The pre-reactive complexes of R3 and R4 on the other hand were found to have relatively large energetic differences. The ring formation in the R4 reaction was found to have a greater stabilizing effect than that of the R3 complex with M11/CBS predicting an energy difference of 2.14 kcal/mol and CCSD(T)/CBS predicting a difference of 2.22 kcal/mol.

One simple explanation for the difference in the stabilizing effect could be steric effects. The hydroxyl radical is constrained when trying to form a ring between the carboxylic acid and central carbonyl oxygen due to the shape of the Tc conformer of pyruvic acid and the size of the hydroxyl radical. On the other hand, the location of the hydrogen of the Tt conformer allows the hydroxyl radical to be less constrained in its interactions with the nearest carbonyl oxygen, which leads to more favorable interactions.

The products of each reaction were also optimized, and the structures are presented in Figure 4.4. It was found that the intramolecular hydrogen bonding found only in the Tc conformation of the transition state had an impact on the final product produced by each set of reactions. For example, when looking at the OH addition to the acid carbon in the R5 reaction, a single radical product is produced due to the hydrogen bonding between the acid and carbonyl

functional groups. Whereas the product of the R6 reaction falls apart and forms carbonic acid and an acetyl radical because of the lack of intramolecular hydrogen bonding. The same effect is seen in the other OH addition reaction, where R7 produces pyruvic acid and a hydroxylcarbonyl radical and R8 produces a single radical product. In this case a different product was formed because the location of the hydrogen in the Tc conformation leads to less favorable interactions with the added OH group.

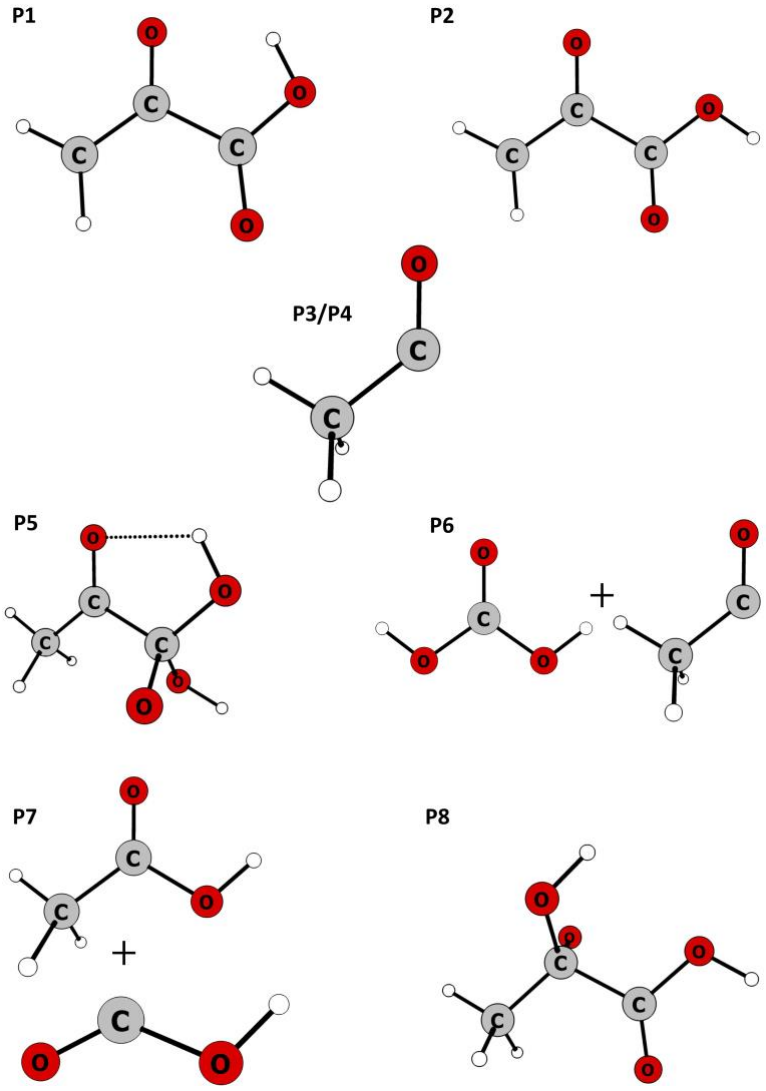

Figure 4.4 Product structures obtained using M11/cc-pVTZ for the OH+PA reactions. CO_2 and H_2O products are not shown in the figure.

A summary of the reaction energetics for each reaction relative to the Tc conformer are tabulated in Table 4.2 and the energetics for the pre-reactive complexes are presented in Table 4.3. In all cases except the R3 reaction, CCSD(T) predicts a lower adiabatic barrier than M11. Some of these changes are quite significant with R8 was lowered by nearly a factor of two, R5 was decreased by approximately 4 kcal/mol and R3 was increased by 2 kcal/mol. The CCSD(T)/CBS theory also predicts deeper wells for the methyl abstraction pre-reactive complexes and more shallow wells for the acid abstraction reactions.

Table 4.2 Energetics for the reactions of PA+OH relative to the Tc conformer, which were calculated using M11/CBS as well as CCSD(T)/CBS//M11/cc-pVTZ in kcal/mol. The energetics of the reaction barriers were determined from the reactants at infinite separation.

T=298K	ΔE_{TS}^{M11}	$\Delta E_{TS}^{CCSD(T)}$	ΔH_{rxn}^{M11}
R1	4.71	4.27	-24.37
R2	6.91	6.24	-21.26
R3	5.11	6.97	-40.26
R4	5.93	4.64	-40.26
R5	11.04	7.01	-3.24
R6	13.07	11.79	-32.96
R7	10.14	5.75	-30.46
R8	10.63	6.29	-15.14

Table 4.3 Energetics for the pre-reactive complex (PRC) energies of the reactions of PA+OH. These were calculated using M11/CBS as well as CCSD(T)/CBS//M11/cc-pVTZ in kcal/mol.

T=298K	ΔE_{TS}^{M11}	$\Delta E_{TS}^{CCSD(T)}$
PRC1	-2.23	-3.04
PRC2	-0.21	-0.87
PRC3	-4.52	-3.44
PRC4	-3.79	-3.01

Figures 4.5 and 4.6 are a graphical representation for the reaction energetics for the Tc and Tt conformers of the transition states respectively. The black lines are the M11/CBS energetics and the red lines for each barrier are from the CCSD(T) energy calculations.

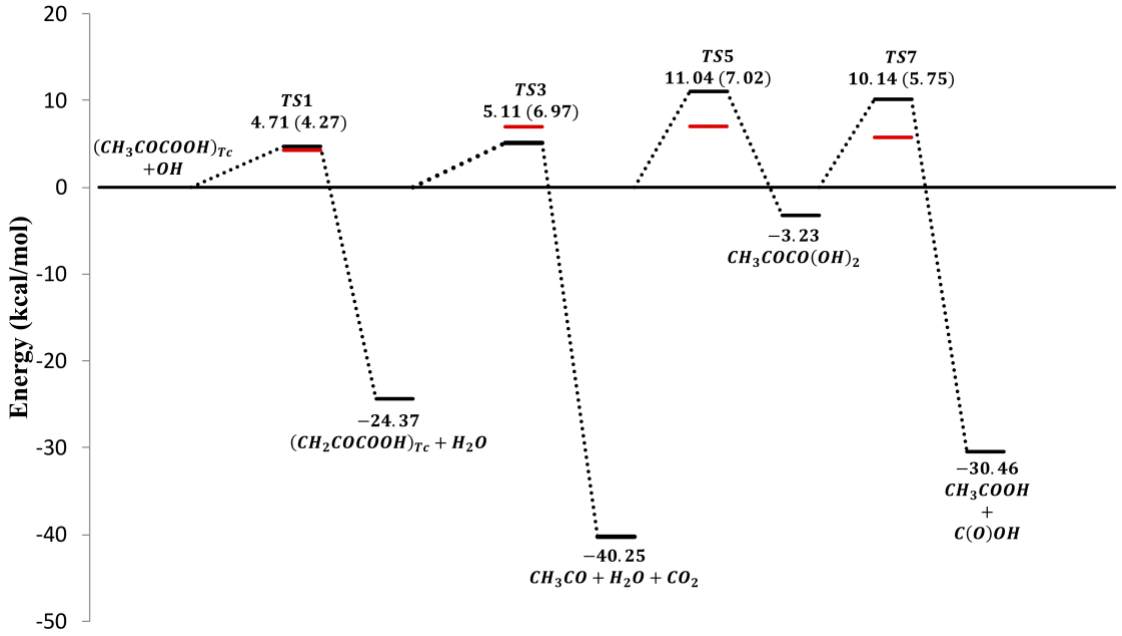

Figure 4.5 Reaction diagram between pyruvic acid and OH radicals with the transition states resembling the Tc conformer. The black lines indicate the energy at the M11/CBS level of theory and the red lines indicate the energetics that were calculated using CCSD(T)/CBS.

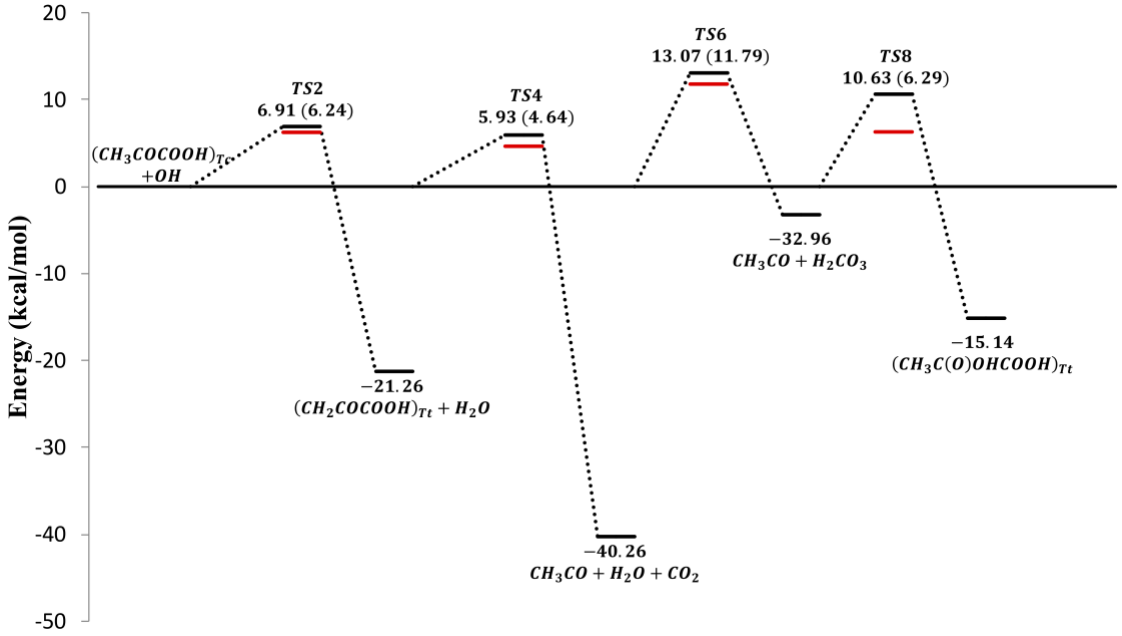

Figure 4.6 Reaction diagram between pyruvic acid and OH radicals with the transition states resembling the Tt conformer. The black lines indicate the energy at the M11/CBS level of theory and the red lines indicate the energetics that were calculated using CCSD(T)/CBS.

These figures show that CCSD(T) predicts lower adiabatic barriers for every reaction studied except for the R3 acid abstraction, which saw a 1.86 kcal/mol increase in barrier height. Both M11 and CCSD(T) predict the pre-reactive complexes of the acid abstractions to be more energetically stable than those of the methyl abstractions, which can be ascribed to the ring formation found in those complexes.

The relative abundance of each conformer at 298K were also determined based on the reaction exothermicity and the partition functions of the two conformers. There is a large energetic difference between the Tt and Tc conformers due to the additional intramolecular hydrogen bonding between the acid hydrogen and the central carbonyl group found in the Tc conformer. Because of the large change in exothermicity between these conformers it was found that the relative abundance of the Tt conformer at room temperature is less than 2% for both methods used in this study. Although CCSD(T) does indicate there is a slightly higher population of the Tt conformer, the exothermicity predicted by M11 and CCSD(T) are larger than those previously reported in literature. Reva *et al.* reported an endothermicity of 2.08 (±0.31) kcal/mol experimentally and 2.29 kcal/mol using theory.[141] It is worth noting that the previous experimental estimate for the endothermicity by Schellenberger *et al.* was 2.34 (±0.32) kcal/mol, which is in much better agreement with the present results.[142]

Table 4.4 Relative abundance of each conformer of pyruvic acid at T=298K. The abundance of each conformer was calculated from the ratio of their partition functions and the change in exothermicity. Units for the reaction enthalpy are kcal/mol.

$$K_{EQ} = \frac{PA(Tt)}{PA(Tc)} = \frac{Q_{Tt}}{Q_{Tc}} e^{\frac{-\Delta H_{rxn}}{k_B T}}$$

T=298K	ΔH_{rxn}	$\%PA(Tc)$	$\%PA(Tt)$
M11	2.87	98.69	1.31
CCSD(T)	2.64	98.09	1.91

4.3.2 Reaction Kinetics of OH with Pyruvic Acid

Next the results of the M11/CBS and CCSD(T)/CBS calculations were used to calculate the rate coefficients of pyruvic acid with OH from 200K to 400K. The reaction path degeneracy and chirality for each transition state and the small curvature tunneling coefficient at T=298K are presented in Table 4.5. Each methyl abstraction reaction has a reaction path degeneracy of three and every transition state structure studied for the OH reactions had a non-superimposable mirror image, thus a factor of two was also applied. It was found that the small-curvature tunneling coefficient for most reactions is approximately between 2-3 at room temperature with the exception being the acid abstraction reactions where the tunneling factor is found to be quite large with a value of 16.65 for R3 and 10.26 for R4. The larger transmission coefficients for R3/R4 reactions can be explained by the width of the reaction barriers for these reactions. The R3 and R4 reactions had imaginary frequencies of 1870i cm^{-1} and 1720i cm^{-1}, which were much larger than the barrier frequencies of the other reactions. The threshold energy of the SCT tunneling calculation was assumed to be that of the pre-reactive complexes. The pre-reactive complexes are thought to be in thermal equilibrium with the reactants due to a larger dissociation rate from the PRC to the reactants. The thermal rate constant itself was calculated from an equilibrium constant determined using the partition functions of the complexes and reactants and energy difference between them as well as a conventional transition state theory expression for the transition state barriers between the complexes and adiabatic reaction barriers as shown below.

$$K_c = \frac{[PRC]}{[OH][PA]} \tag{4.11}$$

$$k_{eff} = K_C K_2 \tag{4.12}$$

Table 4.5 Factors for the reaction path degeneracy (n), chirality of the transition state structures (m) and small-curvature tunneling coefficient for OH+PA at T=298K used in calculating the reaction rate constants for the reactions of PA+OH.

T=298K	n	m	κ^{SCT}
R1	3	2	2.02
R2	3	2	2.07
R3	1	2	16.65
R4	1	2	10.26
R5	1	2	2.03
R6	1	2	2.86
R7	1	2	1.86
R8	1	2	1.91

The rate constants for each pair of transition state conformers were calculated using the equation for multi-path transition state theory given in Equation 2.9. The resulting rate constants for M11/CBS and CCSD(T)/CBS at several different temperatures are presented in Tables 4.6 and 4.7 respectively. The effective rate constant is simply a sum of the other rate constants for each reaction.

Table 4.6 Rate constants for each transition state conformer pair studied for OH+PA calculated with the M11/CBS energetics at T=200K, 250K, 298K and 350K as well as the effective overall rate constant. Units for these rate constants are molecule cm^3 s^{-1}.

$T(K)$	k_{R1+R2}	k_{R3+R4}	k_{R5+R6}	k_{R7+R8}	$k_{effective}$
200	$6.73\text{x}10^{-17}$	$1.58\text{x}10^{-16}$	$4.39\text{x}10^{-25}$	$4.07\text{x}10^{-24}$	$2.25\text{x}10^{-16}$
250	$3.53\text{x}10^{-16}$	$3.17\text{x}10^{-16}$	$5.11\text{x}10^{-23}$	$3.41\text{x}10^{-22}$	$6.70\text{x}10^{-16}$
298	$1.21\text{x}10^{-15}$	$6.16\text{x}10^{-16}$	$1.30\text{x}10^{-21}$	$6.74\text{x}10^{-21}$	$1.83\text{x}10^{-15}$
350	$3.49\text{x}10^{-15}$	$1.19\text{x}10^{-15}$	$1.79\text{x}10^{-20}$	$7.33\text{x}10^{-20}$	$4.67\text{x}10^{-15}$

Table 4.7 Rate constants for each transition state conformer pair studied for PA+OH calculated with the CCSD(T)/CBS energetics at T=200K, 250K, 298K and 350K as well as the effective overall rate constant. Units for these rate constants are molecule cm^3 s^{-1}.

$T(K)$	k_{R1+R2}	k_{R3+R4}	k_{R5+R6}	k_{R7+R8}	$k_{effective}$
200	$2.00\text{x}10^{-16}$	$2.32\text{x}10^{-16}$	$1.07\text{x}10^{-20}$	$2.48\text{x}10^{-19}$	$4.33\text{x}10^{-16}$
250	$8.52\text{x}10^{-16}$	$5.08\text{x}10^{-16}$	$1.56\text{x}10^{-19}$	$2.27\text{x}10^{-18}$	$1.36\text{x}10^{-15}$
298	$2.55\text{x}10^{-15}$	$9.86\text{x}10^{-16}$	$1.04\text{x}10^{-18}$	$1.08\text{x}10^{-17}$	$3.55\text{x}10^{-15}$
350	$6.63\text{x}10^{-15}$	$1.82\text{x}10^{-15}$	$4.87\text{x}10^{-18}$	$3.90\text{x}10^{-17}$	$8.49\text{x}10^{-15}$

The CCSD(T) method predicts larger effective rate constants over the temperature range examined. CCSD(T) also predicts an increase in the rate constant of each conformer pair. Both M11 and CCSD(T) predict that the OH addition reactions play an insignificant role in the overall rate constant. Both theories also suggest the R3/R4 conformer pair is the largest contributor to the effective rate constant at low temperatures which can be explained by the large tunneling coefficients. At higher temperatures where tunneling is less important, the R1/R2 pair becomes the largest contributor to the overall rate constant. The effective rate constants using CCSD(T) energetics were also compared to the gas phase rate constants reported by Mellouki and Mu and the results are presented in Figure 4.7.[40]

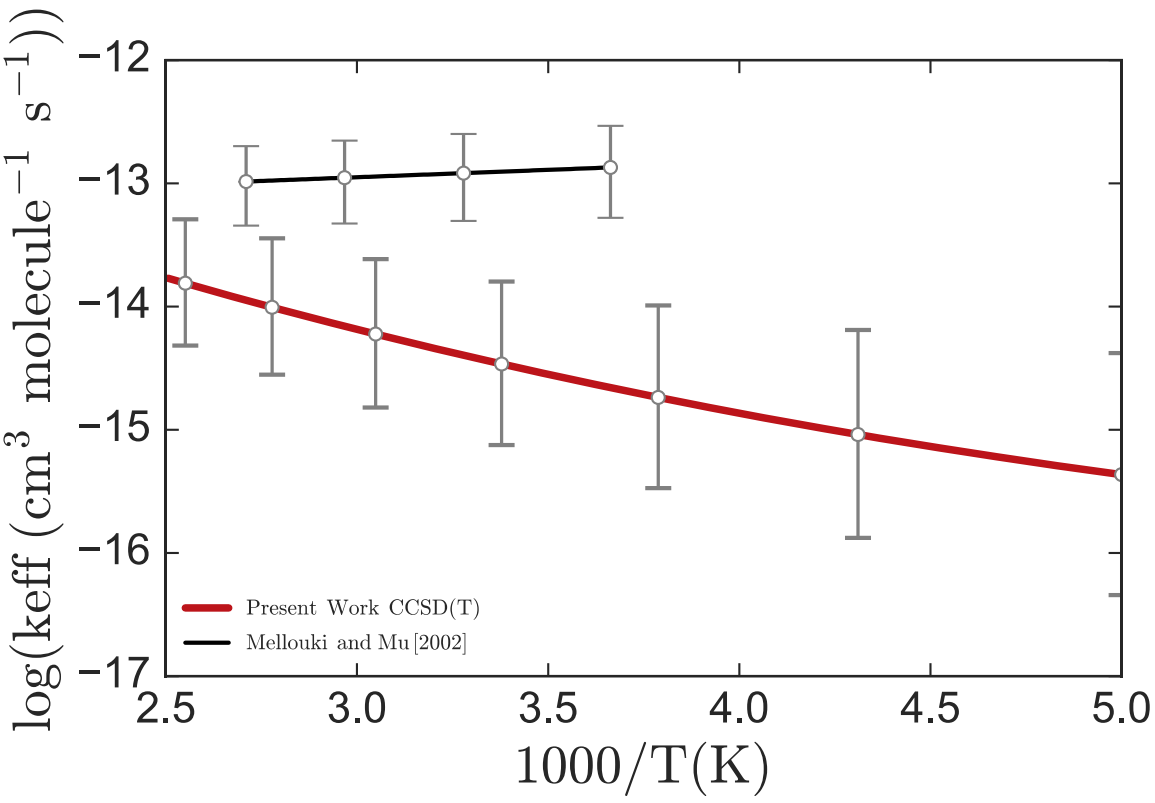

Figure 4.7 Effective rate constants for OH+PA using CCSD(T)/CBS in red, as well as the effective rate constant from the fit reported by Mellouki and Mu with error bars. [40]

It was found that at all temperatures studied the theoretical rate coefficents were much lower than the previously reported experimental values from Mellouki and Mu Neither theoretical method predicted the negative temperature dependence observed by Mellouki and Mu.[40] At 298K they report a rate constant of 1.2(±0.4)x10^{-13} cm^3 s^{-1} taken from their series of measurements at that temperature. This is much larger than our CCSD(T) value of 3.55x10^{-15} cm^3 s^{-1}. The present results are instead much closer to an older value by Grosjean.[143] who reported a single estimated rate constant of less than 5.0x10^{-14} cm^3 s^{-1} at 298K. Upper and lower limits for the values in the present work are obtained by taking a ±20% error in the barrier heights. Only at higher temperatures does the lower limit of the experimental values and upper limit of the present work agree.

There could be both experimental and theoretical reasons for the discrepancies between the rate constants predicted by theory and those determined experimentally. The rate constants reported by Mellouki and Mu may have had errors steming from their pyruvic acid concentrations. Pyruvic acid is a highly oxidized molecule which has a tendancy to have significant interactions with the walls of reaction chambers. [41] [144] These interactions can cause the actual concentrations in the gas phase to be much lower than what would be expected. The authors attempted to take the error from the concentration into account by adding an additional 15% into their uncertainty. However, more accurate measurements could be made by monitoring the concetration during the experiment by use of FTIR spectra.[38] [144] [145] Because of its high reactivity, OH radical loss to byproducts or walls is another significant source of error which can produce errors in the experimental rate constant. [146] On the theoretical side, any errors in the stationary point structure energetics or vibrational frequencies could have large effects in both the magnitude of the rate constant as well as the temperature dependence.

A fit of the theoretical rate constants determined for each method are also reported using a double expontential modified Ahrenius form and are presented in Table 4.8.

Table 4.8 Double exponential Ahrenius fit of the effective rate constants for PA+OH from the two different methods used in this study. These are fit with the form $k = A_1\ T^{n_1}\ e^{-\frac{B_1}{k_B T}} + A_2\ T^{n_2}\ e^{-\frac{B_2}{k_B T}}$. Units for these fits are are molecule cm^3 s^{-1} and kcal/mol.

$T(K)$	A_1	n_1	B_1	A_2	n_2	B_2
M11	3.97x10^{-22}	3.26	2.17	3.16x10^{-32}	6.17	-1.40
CCSD(T)	4.52x10^{-22}	3.25	1.82	6.13x10^{-28}	4.79	-0.60

The individual rate constants of the four abstraction reactions were also calculated separately using conventional transition state theory to observe if any of these reactions had negative temperature dependence similar to those of acetic acid. Although the overall rate constant for PA+OH was

found to have no negative temperature dependence, if one assumes that the R1 and R3 reactions originate from the Tc conformer and the R2 and R4 originate from the Tt conformer, it was found that the individual rate constant of the R4 reaction increased inversely with temperature. The Tt conformer of pyruvic acid and the abstraction process itself for the R4 reaction closely resembles that of acetic acid and its rate coefficients behave similarly with negative temperature dependence and a larger magnitude than the other three abstraction reactions. Although the R4 rate coefficients had larger magnitudes and showed the expected temperature dependence observed by Mellouki and Mu the large difference in exothermicity between the two conformers of pyruvic acid reduces the amount the R4 reaction contributes to the overall effective rate constant.[40]

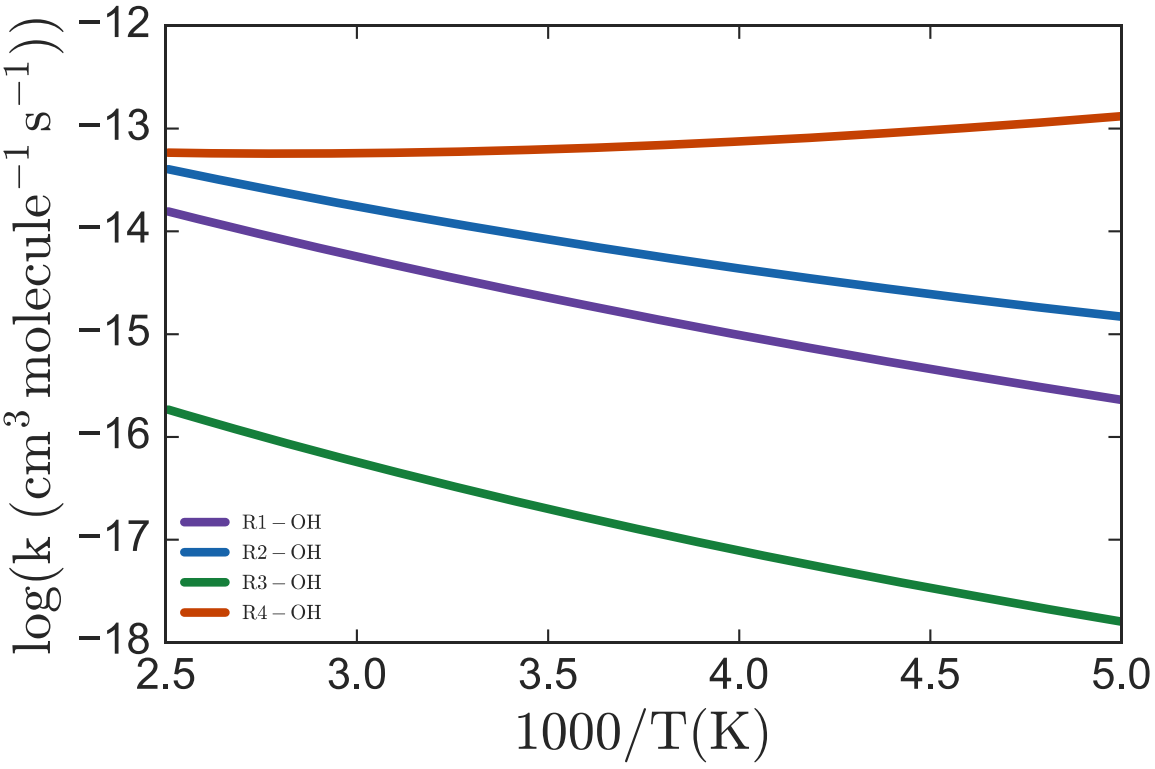

Figure 4.8 Individual rate constants for the the four OH+PA abstraction reactions which were calculated with CCSD(T)/CBS energetics and a conventional rate constant expression.

4.3.3 Reaction Energetics of HO_2 with Pyruvic Acid

Hydroperoxy radicals are another chemical species found in the troposphere which can play roles in chemical reactions. Although less reactive than OH, the decreased reactivity of these radicals leads to higher concentrations in the troposphere. For comparison with the OH results presented in Section 4.2 the reactions of several HO_2 radical reactions with pyruvic acid were examined. Using the previous study of HO_2 with hydrogen halides as a guide, similar reactions where HO_2 could act as a double hydrogen exchange mediator were found. [147] [148] Once again, M11/cc-pVTZ was used to optimize all stationary point structures involving HO_2 as well as to determine the molecular normal modes. The optimized transition state structures for the reactions studied are shown in Figure 4.8.

$$R1 - HO_2: CH_3COCOOH + HO_2 \rightarrow (CH_2COCOOH)_{Tc} + H_2O_2 \quad (4.13)$$

$$R2 - HO_2: CH_3COCOOH + HO_2 \rightarrow CH_3CO + H_2O_2 + CO_2 \quad (4.14)$$

$$R3 - HO_2: CH_3COCOOH + HO_2 \rightarrow (CH_2COHCOOH)^a_{Tt} + HO_2 \quad (4.15)$$

$$R4 - HO_2: (CH_3COCOOH)^b_{Tc} + HO_2 \rightarrow CH_3COH + CO_2 + HO_2 \quad (4.16)$$

$$R5 - HO_2: CH_3COCOOH + HO_2 \rightarrow CH_3COH + CO_2 + HO_2 \quad (4.17)$$

$$R6 - HO_2: CH_3COCOOH + HO_2 \rightarrow CH_3COHCOO + HO_2 \quad (4.18)$$

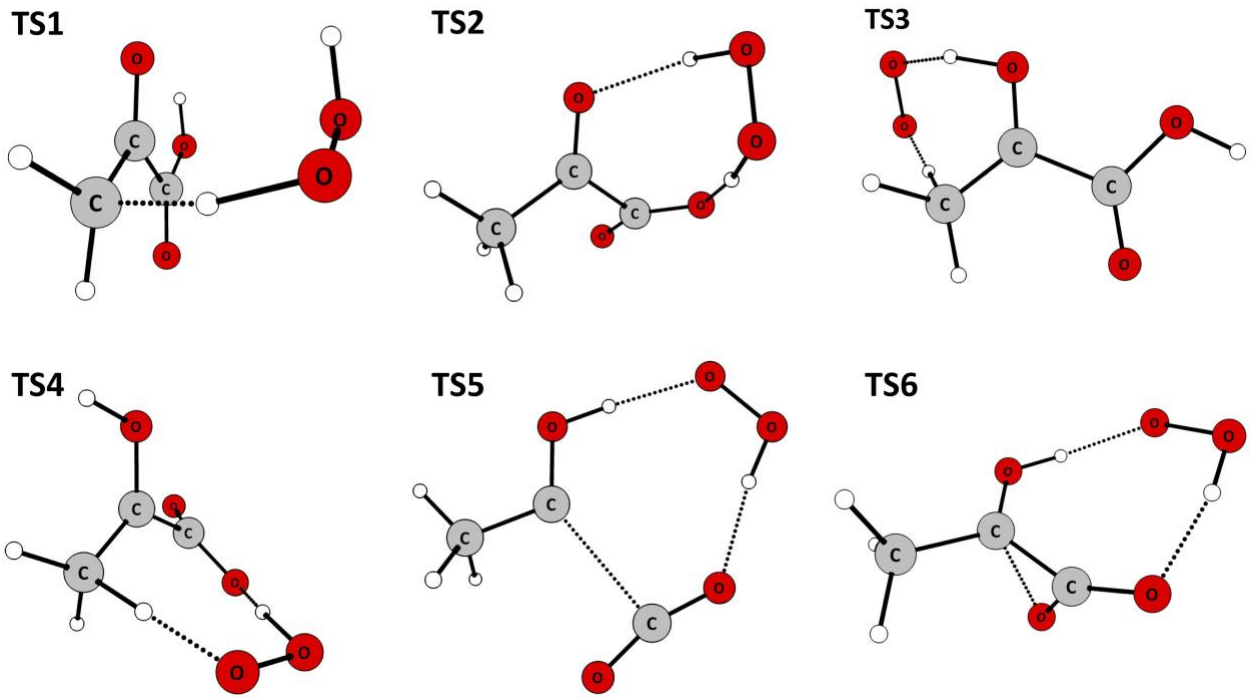

Figure 4.9 Transition state structures obtained using M11/cc-pVTZ for the HO_2+PA reactions. TS1, TS2, TS5, and TS6 originate from the trans-cis conformer of pyruvic acid and TS3, TS4, originate from the trans-trans conformer of pyruvic acid.

Similar to the reactions of pyruvic acid with OH, an abstraction reaction for both the methyl (R1-HO_2) and the carboxylic acid (R2-HO_2) were found. There were also several double hydrogen exchange reactions located, namely R3-HO_2 through R6-HO_2. Reactions 4 and 5 lead to the same carbene product produced from the direct photolysis of the pyruvic acid molecule. The R6-HO_2 reaction yields an alpha lactone product where one oxygen of the carboxylic acid is bound to the central carbonyl carbon. The various products produced by these reactions are presented in Figure 4.10.

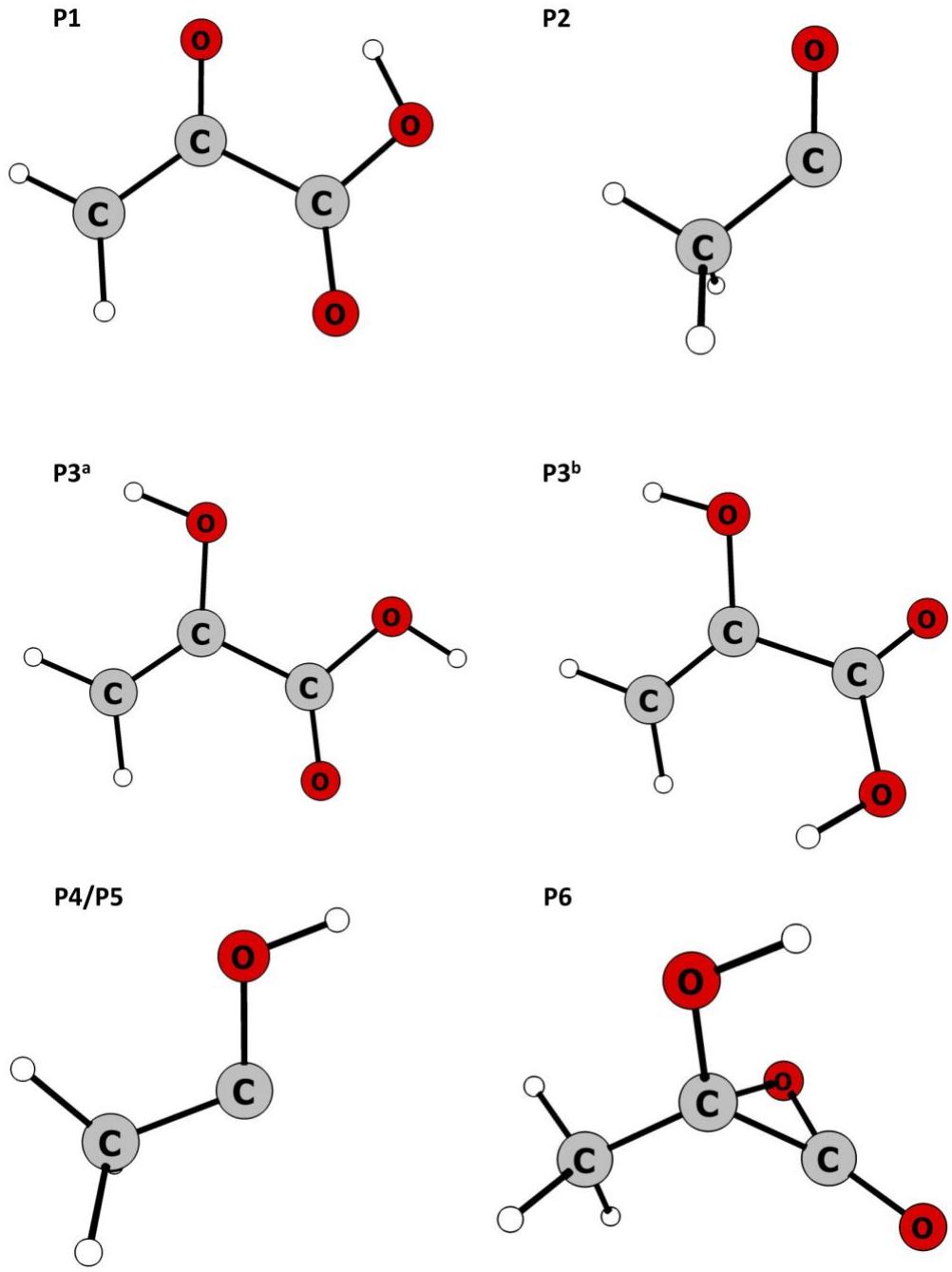

Figure 4.10 Product structures obtained using M11/cc-pVTZ for the HO_2+PA reactions. The products H_2O_2, HO_2 and CO_2 are not shown.

Reactions 1 and 2 yield similar products to the reactions of pyruvic acid with hydroxyl radicals. However, because H_2O_2 is a higher energy product, the overall enthalpy change of these reactions are much higher than those of OH with pyruvic acid. The relative exo/endo-thermicties between

HO_2 and OH were 9.35 compared to -24.37 kcal/mol for the methyl abstraction and -6.54 compared to -40.25 kcal/mol for the acid abstraction. A schematic showing the energetics of the various pathways is shown in Figure 4.11 and the results are tabulated in Table 4.9.

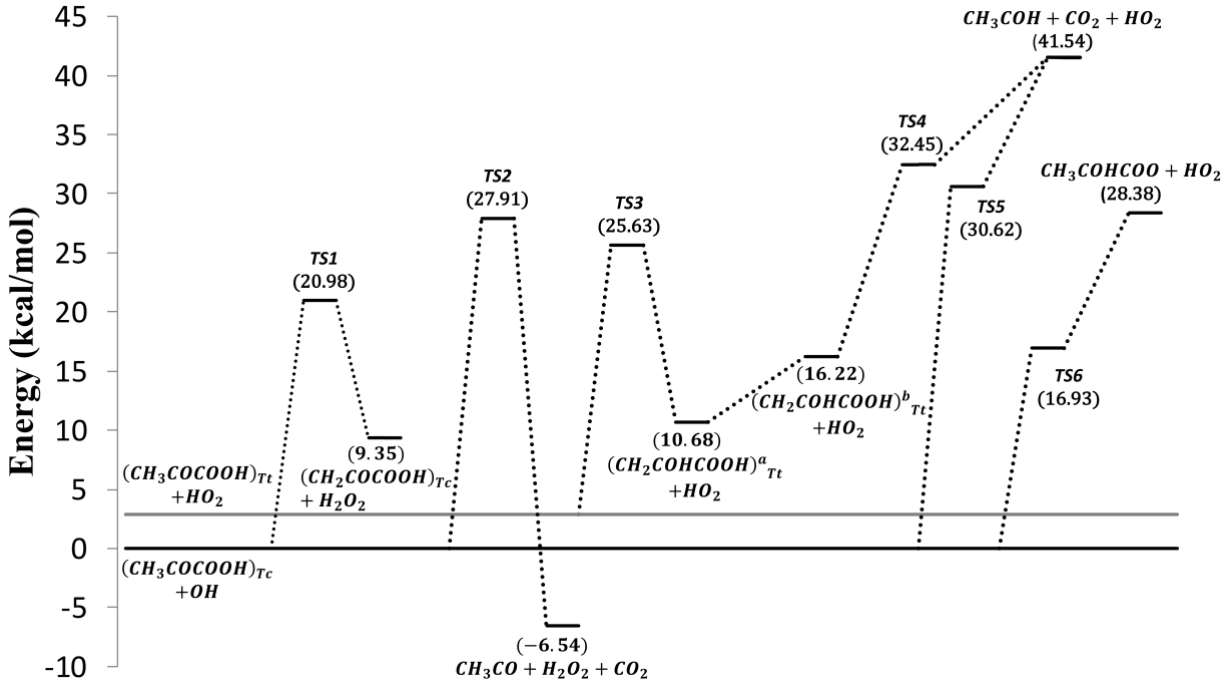

Figure 4.11 Energetics for the reactions of PA+HO_2 calculated using M11/CBS in kcal/mol.

The R3-HO_2 reaction is a hydrogen transfer reaction between the methyl and central carbonyl oxygen. This channel leads to the same methylhydroxycarbene product as the R5-HO_2 reaction. However, the R3-HO_2 reaction is a two-step process which must first proceed through a conformational change with a rearrangement of the carboxlic acid. This new conformer can then donate a hydrogen back to the methyl group and the transition state of this process is TS4. R5-HO_2 is a more direct path to the carbene and is a transfer reaction between the acid functional group and the central carbonyl oxygen. The R6-HO_2 lactone reaction is also a hydrogen transfer between the acid and central carbonyl but instead of undergoing decarboxylation, an oxygen of the acid group binds to the central carbon.

Table 4.9 Energetics for the reactions of PA+HO_2 calculated using M11/CBS in kcal/mol.

	ΔE_{TS}^{M11}	ΔH_{rxn}^{M11}
R1-HO_2	20.98	9.35
R2-HO_2	27.91	-6.54
R3-HO_2	25.63	10.68
R4-HO_2	32.45	41.54
R5-HO_2	30.65	41.54
R6-HO_2	16.93	28.38

It was found that many of the reactions of pyruvic acid with HO_2 are largely endothermic. Only the R2-HO_2 reaction was exothermic with a modest value of -6.54 kcal/mol. This is in stark contrast to the OH reactions, all of which who were exothermic by over 15 kcal/mol or more.

In order to observe how well HO_2 mediates hydrogen atom exchange with pyruvic acid, the values in this study were compared to literature values of the unimolecular process. In Table 4.10 the literature values of the enthalpy change and adiabatic barriers for the unimolecular decomposition of pyruvic acid reported by Takahashi et al and as well as da Silva are presented for comparison.[137 138]

Table 4.10 Energetics for the reactions of unimolecular decomposition of PA in kcal/mol reported by da Silva (a) and Takahashi (b) *et al.* [137 138] Units for the reported energetics are in kcal/mol.

	ΔE_{TS}	ΔH_{rxn}
R3[a]	50.70	N/A
R4[a]	60.00	43.00
R5[a]	40.60	43.00
R5[b]	38.28	40.63
R6[a]	35.60	28.70

The energy change predicated by M11/CBS are in good agreement with both literature sources. The endothermicity of the R5-HO_2 reaction and the value reported by da Silva had the greatest difference at 1.46 kcal/mol. All other reactions studied had a difference less than 1 kcal/mol. When comparing the barriers of the present work with the unimolecular barriers it becomes clear that

similar to the hydrogen halide study, HO_2 is able to act as a hydrogen transfer meditator and have a barrier lowering effect on the exchange reactions. This is especially true in reactions R3-HO_2, R4-HO_2, and R6-HO_2 where each reaction barrier decreased approximately by a factor of 2 when HO_2 was present. Reaction 5 on the other hand saw a much smaller catalytic effect, only decreasing 40.6 to 30.65 kcal/mol.

Although HO_2 was seen to have a catalytic effect for these reactions, this effect is offset by the fact that each of these reactions are still largely endothermic. The two major products of the exchange reactions had endothermicities of 41.54 kcal/mol and 28.38 kcal/mol. Because of the relatively unstable products formed by these reactions, the catalytic effect of HO_2 simply created submerged barriers in many of these reactions which will diminish any significant effect this barrier lowering would have on the thermal rate constants of these reactions.

4.3.4 Reaction Kinetics of HO_2 with Pyruvic Acid

Similar to the OH reactions, the HO_2 rate constants were obtained using multi-path transition state theory given in Equation 2.9. However, unlike the reactions involving OH, there was only a single conformer of the transition state for each reaction. The reaction path degeneracy and transition state chirality are again considered for each reaction when determining the rate constants, which are tabulated in Table 4.11.

Table 4.11 Factors for the reaction path degeneracy (n), transition state chirality (m) and small-curvature tunneling coefficient for HO_2+PA at T=298K used when determining the rate coefficients.

T=298K	n	m	κ^{SCT}
R1-HO_2	3	2	51.11
R2-HO_2	1	2	12603.35
R3-HO_2	3	2	95.67
R5-HO_2	1	1	1.01
R6-HO_2	1	2	1.00

The R1-HO_2, R2-HO_2 and R3-HO_2 reactions were all found to have significant tunneling at T=298K. Each of these reactions possessed very narrow barriers and large barrier frequencies for example R1/R3-HO_2 had barrier frequencies of 2334.2 cm^{-1} and 1557.00 cm^{-1} respectively. The R2-HO_2 reaction had an extremely large transmission coefficient due to its narrow barrier at 298K. It was found that the R2-HO_2 reaction had a large barrier frequency of 4896.9 cm^{-1}. The rate constants calculated using the M11/CBS energetics are presented in Table 4.12. The only rate coefficients that contribute significantly to the overall rate constant are reactions R1-HO_2 and R6-HO_2. Both of these reactions had the lowest reaction barriers for the reaction studied. All the other reactions studied were orders of magnitude smaller than that of the R1/R6-HO_2 reactions and played virtually no role in the rate constant. It's worth noting that the rate constants for the R6-HO_2 reaction were obtained from a submerged barrier, which causes the reported effective rate constant to be an upper limit.

Table 4.12 Rate constants for each reaction of HO_2+PA studied calculated with the M11/CBS energetics at T=200K, 250K, 298K and 350K as well as the effective overall rate constant. Units for these rate constants are molecule cm^3 s^{-1}.

$T(K)$	k_{R1}	k_{R2}	k_{R3}	k_{R4}	k_{k6}	$k_{effective}$
200	$1.20\text{x}10^{-33}$	$2.36\text{x}10^{-37}$	$1.04\text{x}10^{-38}$	$2.03\text{x}10^{-46}$	$1.94\text{x}10^{-33}$	$3.14\text{x}10^{-33}$
250	$4.61\text{x}10^{-30}$	$2.76\text{x}10^{-33}$	$1.50\text{x}10^{-34}$	$1.57\text{x}10^{-40}$	$1.05\text{x}10^{-29}$	$1.51\text{x}10^{-29}$
298	$1.18\text{x}10^{-27}$	$1.40\text{x}10^{-30}$	$8.70\text{x}10^{-32}$	$4.78\text{x}10^{-36}$	$2.83\text{x}10^{-27}$	$4.02\text{x}10^{-27}$
350	$1.03\text{x}10^{-25}$	$2.05\text{x}10^{-28}$	$1.44\text{x}10^{-29}$	$1.52\text{x}10^{-32}$	$2.23\text{x}10^{-25}$	$3.27\ \text{x}10^{-25}$

Similar to the OH+PA reaction, a fit was generated from these upper limit estimates of the rate coefficients with a double exponential Ahrenius form, which is presented in Table 4.13.

Table 4.13 Double exponential Ahrenius fit of the effective rate constants for PA+HO_2 using M11/CBS. These are fit with the form $k = A_1\ T^{n_1}\ e^{-\frac{B_1}{k_B T}} + A_2\ T^{n_2}\ e^{-\frac{B_2}{k_B T}}$. Units for this fit are molecule cm^3 s^{-1} and kcal/mol.

$T(K)$	A_1	n_1	B_1	A_2	n_2	B_2
M11	$1.14\text{x}10^{-23}$	3.20	$7.80\text{x}10^{3}$	$2.49\text{x}10^{-20}$	$9.72\text{x}10^{-3}$	$6.63\text{x}10^{3}$

The effective overall rate coefficients of the HO_2+PA reaction are presented graphically in Figure 4.12 with a comparison to the previously determined effective rate constants from the OH reactions using both CCSD(T)/CBS and M11/CBS.

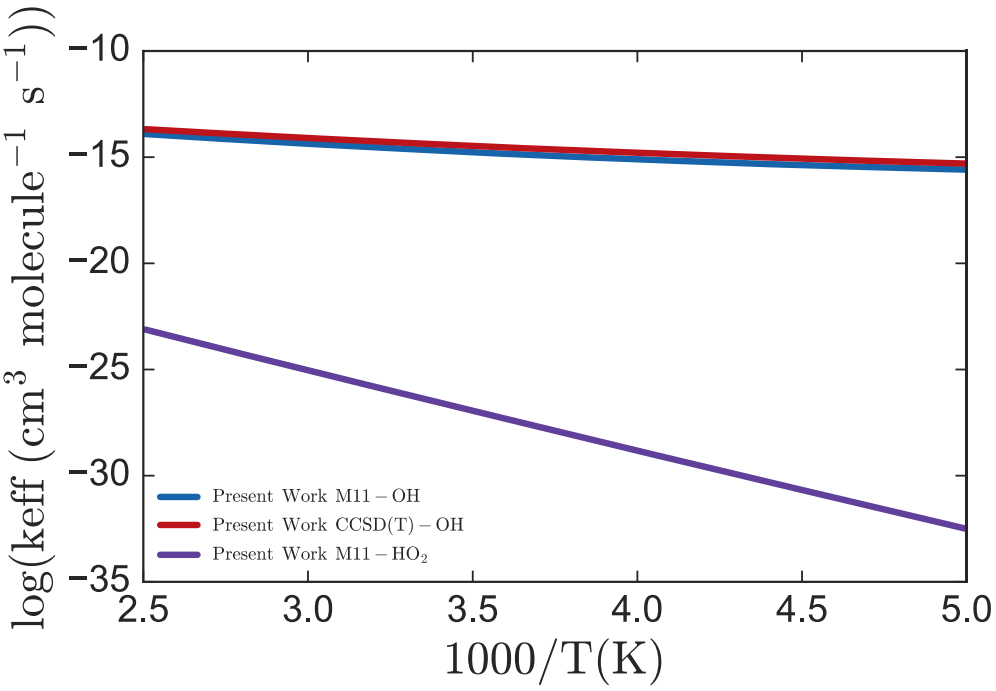

Figure 4.12 Effective rate constants for the reaction of PA+HO_2 from the results with M11/CBS, as well as the rate constants of OH with pyruvic from both methods used.

Despite the catalytic effect HO_2 plays on the reaction barriers with pyruvic acid, the effective overall rate constant is much smaller than that of pyruvic acid with hydroxyl radicals. This can be explained by the large adiabatic barriers of the HO_2 reactions compared to those of the OH reactions. The individual rate constants for each reaction are presented in Figure 4.13, however as mentioned earlier, the rate constants of the submerged reactions R5 and R6 should only be considered as upper limits, because it is the rate constant for going into a post-reactive complex.

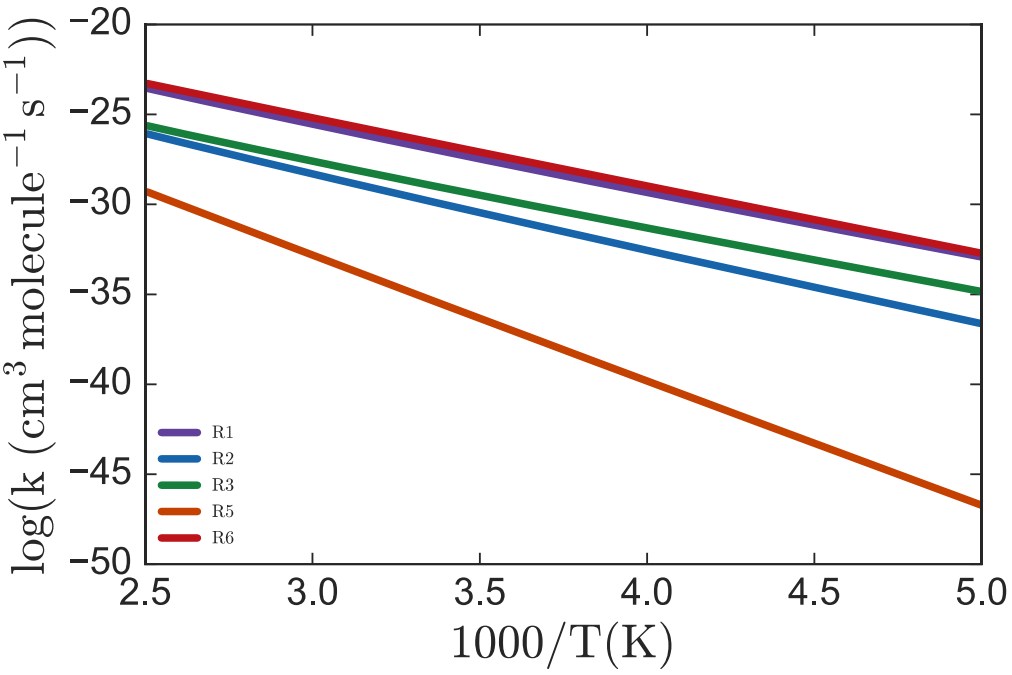

Figure 4.13 Individual rate constants for the reactions of PA+HO_2 calculated using M11/CBS. Again the fastest reactions were the methyl abstraction reaction R1-HO_2 and the lactone reaction R6-HO_2.

4.3.5 Comparison of Photolysis of PA to that of OH Oxidation

Photolysis has been known to be the primary source of removal for pyruvic acid in the atmosphere, with hydroxyl radical reactions only playing a role as secondary sinks.[40 144] Photolysis is the dominant degradation pathway due to the slow oxidation by hydroxyl radicals and the ability to absorb in the UV-vis region. [40 143] Reed Harris *et al.* have performed photolysis experiments on gas phase pyruvic acid and have reported gas phase photolysis rate constants as a function of bath pressure.[38]

The last thing presented is a comparison between the gas phase photolysis rate constants of pyruvic acid at various bath pressures taken from the work by Reed Harris *et al.* and psuedo first order rate constants obtained from the CCSD(T) fit. The pseudo first order rate were

determined from approximate OH concentrations calculated from mixing ratios at various atmospheric pressures taken from *Aeronomy of the Middle Atmosphere* by Guy Brasseur and Susan Soloman. [149] The gas phase photolysis rate constants reported by Reed Harris *et al.* were obtained from two pressures of pyruvic acid at various bath pressures of air. This comparison is presented graphically in Figure 4.14, with the data used to create this figure tabulated in Tables 4.12 and 4.13.

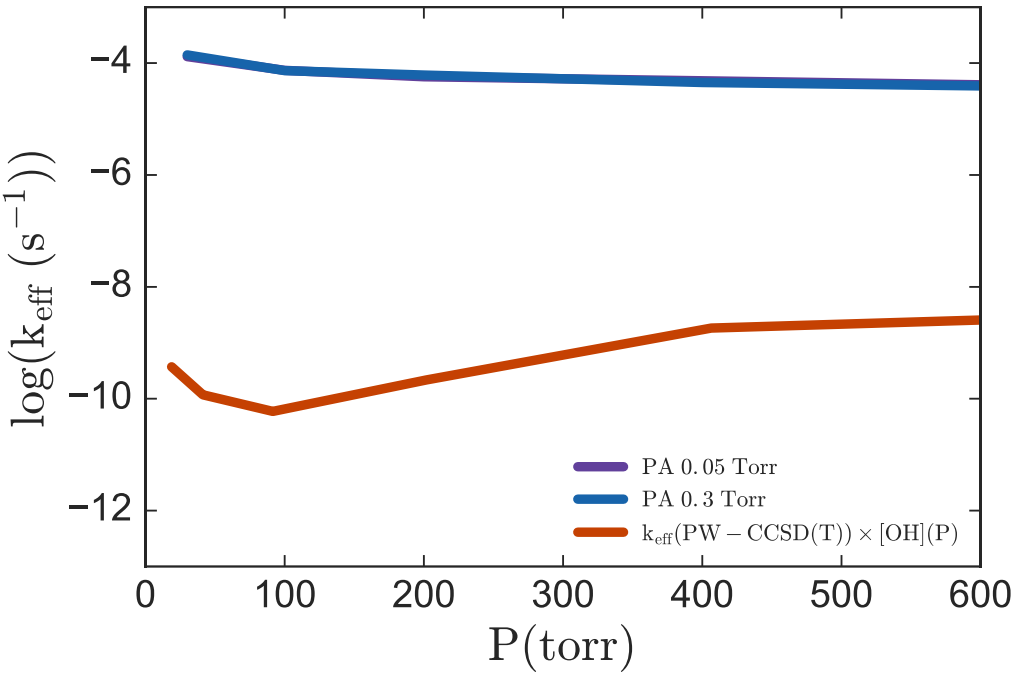

Figure 4.14 Gas phase photolysis rate constants at various pressures compared to pseudo first order rate constants for OH+PA. The photolysis rate constants were obtained for pyruvic acid with pressures of 0.05 torr and 0.3 torr, taken from the work by Reed Harris *et al.* The pseudo first order rate constants were calculated from OH concentrations reported in Aeronomy of the Middle Atmosphere and the rate constants determined from the CCSD(T) fit.[38] [149]

Table 4.14 Pseudo first order rate constants for PA+OH. These were obtained from OH concentrations reported in Aeronomy of the Middle Atmosphere and the rate constants determined from the CCSD(T) energetics.[149]

P (Torr)	T (K)	OH (molecule cm^{-3})	$k(T)$ (cm^3 s^{-1})	$k(P)$ (s^{-1})
759.80	288.0	1500000	$3.51x10^{-15}$	$5.26x10^{-9}$
406.53	259.3	1500000	$1.65x10^{-15}$	$2.47x10^{-9}$
201.77	229.7	348500	$8.63x10^{-16}$	$3.01x10^{-10}$
91.51	212.6	147000	$5.81x10^{-16}$	$8.55x10^{-11}$
41.25	215.5	270000	$6.22x10^{-16}$	$1.68x10^{-10}$
18.75	218.6	788500	$6.69x10^{-16}$	$5.27x10^{-10}$

Table 4.15 Photolysis rate constants of pyruvic acid obtained from the work by Reed Harris *et al.* [38] The gas phase photolysis rate coefficients have units of s^{-1}.

Pressure (Torr)	J_{PA} (0.05 Torr)	J_{PA} (0.1 Torr)
30	$1.30x10^{-4}$	$1.40x10^{-4}$
100	$7.40x10^{-5}$	$7.30x10^{-5}$
200	$5.70x10^{-5}$	$6.10x10^{-5}$
400	N/A	$4.50x10^{-5}$
600	$4.10x10^{-5}$	$3.90x10^{-5}$

It was found that at every appreciable pressure the gas phase photolysis rate constants are much larger than those the OH+PA reactions. Even at higher pressures when photolysis is slowest the values reported by Reed Harris are approximately 4 orders of magnitude larger than that of the OH reaction. This result is in agreement with previous estimates of a slow oxidation rate of pyruvic acid with OH in the atmosphere, and the primary source of destruction for the molecule in the Earth's atmosphere being photolysis.

4.4 Conclusion

In this work the CCSD(T) theoretical rate constant for the OH+PA reaction determined using transition state theory with small-curvature tunneling was found to be approximately 34 times smaller than the value reported by Mellouki and Mu at room temperature. It is possible that this discrepancy may be either theoretical or experimental in nature. In order to rule out major errors produced by the methodology used in this study, the same methods were used to obtain the

energetics of the acid abstraction reaction of acetic acid which were then compared to literature. It was found that the acetic acid values calculated using the methodology in this study compared well to literature with the CCSD(T) energetics falling between the two theoretical values reported in literature. It is worth noting that the R4 acid abstraction energetics were also found to be similar to those of the acetic acid abstraction, and the individual R4 rate constant displayed similar negative temperature dependence.

Hydroperoxy radical reactions with pyruvic acid were also studied and compared to those of OH. The R2-HO_2 acid abstraction reaction was found to have larger tunneling coefficients than that of the R1-HO_2 reaction, which is consistent with the abstraction reactions of OH. However, the R2-HO_2 reaction was found to have a very large tunneling coefficient, with a value of approximately 13000 at T=298K. This extremely large tunneling factor can be ascribed to the extremely narrow width of the reaction barrier. The transition state structure was found to have a large imaginary frequency of 4896 cm^{-1} from the M11/cc-pVTZ calculation. Despite the larger tunneling coefficients for the R1/R2 reactions, the rate coefficients for these abstractions by HO_2 were much smaller than those with OH due to an increased in the height of the reaction barriers. The HO_2 radical was found to have a barrier lowering effect when compared to the unimolecular reaction barriers. Due to the large exothermicity of these reactions the barrier lowering effect created submerged barriers and any rate constant created from these barriers could only be an estimated upper limit. The upper limit for the HO_2+PA rate constant was also found to be approximately 10 orders of magnitude smaller than that of the OH+PA rate constant. Thus even though HO_2 can be found in much greater abundance in the troposphere, any reactions with pyruvic acid would be negligible when compared to both photolysis and OH oxidation.

Chapter 5

Conclusion

In this thesis both the abstraction and exchange reactions of HO_2 radicals with hydrogen halides as well as the abstraction reactions of HO_2 and OH with pyruvic acid. The abstraction and exchange reactions of the HO_2 with HX (X=F, Cl, Br, I) provided a simple model system to study the catalytic effect HO_2 can have when acting as a hydrogen transfer mediator. For each halide studied, the exchange reactions for the halogen series were found to have lower adiabatic barriers than the corresponding abstraction reaction. The lower reaction barrier can be explained by the stability of the highly structured transition state, which can be characterized as a five membered planar ring. Although this ring formation can lower the adiabatic barrier, the highly structured transition state was found to have a higher entropy of activation than that of the abstraction reaction. This competition between entropic and enthalpic effects lead to the abstraction reaction dominating at high temperatures and the exchange reaction to dominating at low temperatures.

Both the abstraction and exchange reaction barriers were also found to decrease with increasing halogen size. The abstraction reaction transition state energies can be explained by simply looking at the relative bond strength of the HX bond, where weaker hydrogen halide bonds lead to lower abstraction barriers. The exchange energetics were not as easily explained due to the fact that an HX bond is both broken and formed when passing through the saddlepoint. Similarly, when looking at the ring structures of the R2 transition states, the H···X···H bond angles were found to become more strained with an increase in size of the halogen. Typically, a larger amount of ring strain would result in less stable structures and thus higher reaction barriers, which was the opposite from the observed trend. To explain this discrepancy QTAIM was used to calculate the delocalization index of the transition state structures for both the abstraction and exchange

reactions. It was found that for each halide the delocalization of the exchange reaction was greater than that of the corresponding abstraction reaction. When comparing the R2 series, the electron delocalization of the ring structures was found to be greatest for the heavier halogens. This helped explain the trend in the barrier heights where despite the more acute H···X···H bond angle, the increased delocalization stabilizes the ring structure leading to lower reaction barriers.

In the second study of this work the reactions of pyruvic acid with HO_2 and OH radicals were examined and compared. Pyruvic acid is a keto-acid intermediate found in the troposphere and is formed at part of the oxidation pathway of isoprene. Many volatile organics in the troposphere, such as isoprene, are decomposed primarily from reactions with OH. Pyruvic acid is slightly unique because it is primarily decomposed from direct photolysis, with OH reactions only acting as a secondary sink. This is caused by slow OH oxidation reactions, as well as the ability of the molecule to absorb well in the UV-vis region. The work performed by Reed Harris *et al.* have suggested that the primary pathway during photolysis was a decarboxylation reaction forming CO_2 and methyhydroxycarbene. This reaction is initiated by hydrogen transfer between the carboxylic acid and the central carbonyl oxygen. Similar to the work in the first study, HO_2 was examined as a potential hydrogen transfer mediator for this reaction on the ground state surface. The DFT energetic calculations did predict a catalytic effect for hydrogen transfer by HO_2 with some of the reaction barriers being decreased by approximately a factor of two. However, unlike the exchange reactions of the first study many of the exchange reactions involving pyruvic acid were largely endothermic due to unstable product formation. These high energy products made the catalytic effect on any potential rate constant negligible.

The rate coefficients for the reactions of OH with pyruvic acid were also calculated for comparison to the experimental values reported by Mellouki and Mu as well as the HO_2 reactions.

Although slow compared to photolysis, the rate coefficients for the reactions of OH with pyruvic acid were found orders of magnitude greater than the reactions with HO_2. Once again this can be ascribed to the high energy products produced from the HO_2 reactions. When comparing our predicted rate constants for the OH reactions to experimental values reported by Mellouki and Mu it was found that both the M11 functional as well as CCSD(T) predicted lower rate coefficients than the experimental values. The experimental values by Mellouki and Mu also showed a negative temperature dependence which was not predicted by either DFT or CCSD(T). Possible causes for the discrepancy could be ascribed to errors in the predicted barrier heights, although the validity of each theoretical method was tested using acetic acid which has similar chemical properties to that of pyruvic. The gas phase photolysis rate constants reported by Reed Harris *et al.* were also compared to the effective rate constants predicted by theory as a function of bath pressure. As expected, it was confirmed that photolysis dominated the reaction with OH at all pressures and temperatures studied in this work, which were modeled after tropospheric conditions.

Bibliography

[1] Heard, D. E.; Pilling, M. J. Measurement of OH and HO2 in the Troposphere. *Chemical Reviews* **2003**, *103* (12), 5163–5198.

[2] Stone, D.; Whalley, L. K.; Heard, D. E. Tropospheric OH and HO 2 Radicals: Field Measurements and Model Comparisons. *Chemical Society Reviews* **2012**, *41* (19), 6348–6404.

[3] Monks, P. S. Gas-Phase Radical Chemistry in the Troposphere. *Chemical Society Reviews* **2005**, *34* (5), 376–395.

[4] Isaksen, I. S. A.; Dalsøren, S. B. Getting a Better Estimate of an Atmospheric Radical. *Science* **2011**, *331* (6013), 38–39.

[5] Salem, M. Z.; Almuzaini, R. F.; Kishawi, Y. S. The Impact of Road Transport on CO 2 Atmospheric Concentrations in Gaza City (Palestine), and Urban Vegetation as a Mitigation Measure. *Polish Journal of Environmental Studies* **2017**, *26* (5).

[6] Brune, W. H.; Tan, D.; Faloona, I. F.; Jaeglé, L.; Jacob, D. J.; Heikes, B. G.; Snow, J.; Kondo, Y.; Shetter, R.; Sachse, G. W. OH and HO2 Chemistry in the North Atlantic Free Troposphere. *Geophysical Research Letters* **1999**, *26* (20), 3077–3080.

[7] Zheng, J.; Meana-Pañeda, R.; Truhlar, D. G. Prediction of Experimentally Unavailable Product Branching Ratios for Biofuel Combustion: The Role of Anharmonicity in the Reaction of Isobutanol with OH. *Journal of the American Chemical Society* **2014**, *136* (13), 5150–5160.

[8] Zhou, D. D.; Han, K.; Zhang, P.; Harding, L. B.; Davis, M. J.; Skodje, R. T. Theoretical Determination of the Rate Coefficient for the HO2+ HO2→ H2O2+ O2 Reaction: Adiabatic Treatment of Anharmonic Torsional Effects. *The Journal of Physical Chemistry A* **2012**, *116* (9), 2089–2100.

[9] Zhou, D. D.; Davis, M. J.; Skodje, R. T. Multitarget Global Sensitivity Analysis of N-Butanol Combustion. *The Journal of Physical Chemistry A* **2013**, *117* (17), 3569–3584.

[10] Som, S.; Liu, W.; Zhou, D. D.; Magnotti, G. M.; Sivaramakrishnan, R.; Longman, D. E.; Skodje, R. T.; Davis, M. J. Quantum Tunneling Affects Engine Performance. *The journal of physical chemistry letters* **2013**, *4* (12), 2021–2025.

[11] Walravens, B.; Battin-Leclerc, F.; Côme, G. M.; Baronnet, F. Inhibiting Effect of Brominated Compounds on Oxidation Reactions. *Combustion and flame* **1995**, *103* (4).

[12] Seshadri, K. Chemical Inhibition of Nonpremixed Methane Flames by CF3Br. *Combustion science and technology* **2005**, *177* (5–6), 871–906.

[13] Montzka, S. A.; Reimann, S.; Engel, A.; Kruger, K.; Sturges, W. T.; Blake, D.; Dorf, M.; Fraser, P.; Froidevaux, L.; Jucks, K. Scientific Assessment of Ozone Depletion: 2010. *Global Ozone Research and Monitoring Project-Report No. 51* **2011**.

[14] Morokuma, K.; Muguruma, C. Ab Initio Molecular Orbital Study of the Mechanism of the Gas Phase Reaction SO3+ H2O: Importance of the Second Water Molecule. *J. Am. Chem. Soc* **1994**, *116* (22), 10316–10317.

[15] Kolb, C. E.; Jayne, J. T.; Worsnop, D. R.; Molina, M. J.; Meads, R. F.; Viggiano, A. A. Gas Phase Reaction of Sulfur Trioxide with Water Vapor. *J. Am. Chem. Soc* **1994**, *116* (22), 10314–10315.

[16] Jayne, J. T.; Pöschl, U.; Chen, Y.; Dai, D.; Molina, L. T.; Worsnop, D. R.; Kolb, C. E.; Molina, M. J. Pressure and Temperature Dependence of the Gas-Phase Reaction of SO3 with H2O and the Heterogeneous Reaction of SO3 with H2O/H2SO4 Surfaces. *J. Phys. Chem. A* **1997**, *101* (51), 10000–10011.

[17] Lovejoy, E. R.; Hanson, D. R.; Huey, L. G. Kinetics and Products of the Gas-Phase Reaction of SO3 with Water. *J. Phys. Chem.* **1996**, *100* (51), 19911–19916.

[18] Takahashi, K.; Kramer, Z. C.; Vaida, V.; Skodje, R. T. Vibrational Overtone Induced Elimination Reactions within Hydrogen-Bonded Molecular Clusters: The Dynamics of Water Catalyzed Reactions in CH 2 FOH·(H 2 O) N. *Phys. Chem. Chem. Phys* **2007**, *9* (29), 3864–3871.

[19] Kramer, Z. C.; Takahashi, K.; Skodje, R. T. Water Catalysis and Anticatalysis in Photochemical Reactions: Observation of a Delayed Threshold Effect in the Reaction Quantum Yield. *J. Am. Chem. Soc* **2010**, *132* (43), 15154–15157.

[20] Vereecken, L.; Francisco, J. S. Theoretical Studies of Atmospheric Reaction Mechanisms in the Troposphere. *Chem. Soc. Rev* **2012**, *41* (19), 6259–6293.

[21] M Kumar, M.; Sinha, A.; Francisco, J. S. Role of Double Hydrogen Atom Transfer Reactions in Atmospheric Chemistry. *Acc. Chem. Res* **2016**, *49* (5), 877–883.

[22] Kent IV, D. R.; Widicus, S. L.; Blake, G. A.; Goddard III, W. A. A Theoretical Study of the Conversion of Gas Phase Methanediol to Formaldehyde. *J. Chem. Phys* **2003**, *119* (10), 5117–5120.

[23] Zhu, R.; Lin, M. C. Ab Initio Study of the Catalytic Effect of H2O on the Self-Reaction of HO2. *Chem. Phys. Lett* **2002**, *354* (3–4), 217–226.

[24] Deng, C.; Wu, X.-P.; Sun, X.-M.; Ren, Y.; Sheng, Y.-H. Neutral Hydrolyses of Carbon Disulfide: An Ab Initio Study of Water Catalysis. *J. Comput. Chem* **2009**, *30* (2), 285–294.

[25] M Staikova, M.; Donaldson, D. J. Water Complexes as Catalysts in Atmospheric Reactions. *Physics and Chemistry of the Earth, Part C: Solar, Terrestrial & Planetary Science* **2001**, *26* (7), 473–478.

[26] Long, B.; Zhang, W.; Tan, X.; Long, Z.; Wang, Y.; Ren, D. Theoretical Study on the Gas Phase Reaction of Sulfuric Acid with Hydroxyl Radical in the Presence of Water. *J. Phys. Chem. A* **2011**, *115* (8), 1350–1357.

[27] Jørgensen, S.; Kjaergaard, H. G. Effect of Hydration on the Hydrogen Abstraction Reaction by HO in DMS and Its Oxidation Products. *J. Phys. Chem. A* **2010**, *114* (14), 4857–4863.

[28] Karton, A. Inorganic Acid-Catalyzed Tautomerization of Vinyl Alcohol to Acetaldehyde. *Chem. Phys. Lett* **2014**, *592*, 330–333.

[29] da Silva, G. Kinetics and Mechanism of the Glyoxal+ HO2 Reaction: Conversion of HO2 to OH by Carbonyls. *J. Phys. Chem. A* **2010**, *115* (3), 291–297.

[30] da Silva, G. Carboxylic Acid Catalyzed Keto-Enol Tautomerizations in the Gas Phase. *Angew. Chem. Int. Ed* **2010**, *49* (41), 7523–7525.

[31] Nguyen, T. B.; Bateman, A. P.; Bones, D. L.; Nizkorodov, S. A.; Laskin, J.; Laskin, A. High-Resolution Mass Spectrometry Analysis of Secondary Organic Aerosol Generated by Ozonolysis of Isoprene. *Atmospheric Environment* **2010**, *44* (8), 1032–1042.

[32] Carlton, A. G.; Turpin, B. J.; Lim, H.-J.; Altieri, K. E.; Seitzinger, S. Link between Isoprene and Secondary Organic Aerosol (SOA): Pyruvic Acid Oxidation Yields Low Volatility Organic Acids in Clouds. *Geophysical Research Letters* **2006**, *33* (6).

[33] Chebbi, A.; Carlier, P. Carboxylic Acids in the Troposphere, Occurrence, Sources, and Sinks: A Review. *Atmospheric Environment* **1996**, *30* (24), 4233–4249.

[34] Veres, P.; Roberts, J. M.; Burling, I. R.; Warneke, C.; de Gouw, J.; Yokelson, R. J. Measurements of Gas-phase Inorganic and Organic Acids from Biomass Fires by Negative-ion Proton-transfer Chemical-ionization Mass Spectrometry. *Journal of Geophysical Research: Atmospheres* **2010**, *115* (D23).

[35] Veres, P. R.; Roberts, J. M.; Cochran, A. K.; Gilman, J. B.; Kuster, W. C.; Holloway, J. S.; Graus, M.; Flynn, J.; Lefer, B.; Warneke, C. Evidence of Rapid Production of Organic Acids in an Urban Air Mass. *Geophysical Research Letters* **2011**, *38* (17).

[36] Andreae, M. O.; Talbot, R. W.; Li, S.-M. Atmospheric Measurements of Pyruvic and Formic Acid. *Journal of Geophysical Research: Atmospheres* **1987**, *92* (D6), 6635–6641.

[37] Talbot, R. W.; Mosher, B. W.; Heikes, B. G.; Jacob, D. J.; Munger, J. W.; Daube, B. C.; Keene, W. C.; Maben, J. R.; Artz, R. S. Carboxylic Acids in the Rural Continental Atmosphere over the Eastern United States during the Shenandoah Cloud and Photochemistry Experiment. *Journal of Geophysical Research: Atmospheres* **1995**, *100* (D5), 9335–9343.

[38] Reed Harris, A. E.; Doussin, J.-F.; Carpenter, B. K.; Vaida, V. Gas-Phase Photolysis of Pyruvic Acid: The Effect of Pressure on Reaction Rates and Products. *The Journal of Physical Chemistry A* **2016**, *120* (51), 10123–10133.

[39] Reed Harris, A. E.; Ervens, B.; Shoemaker, R. K.; Kroll, J. A.; Rapf, R. J.; Griffith, E. C.; Monod, A.; Vaida, V. Photochemical Kinetics of Pyruvic Acid in Aqueous Solution. *The Journal of Physical Chemistry A* **2014**, *118* (37), 8505–8516.

[40] Mellouki, A.; Mu, Y. On the Atmospheric Degradation of Pyruvic Acid in the Gas Phase. *Journal of Photochemistry and Photobiology A: Chemistry* **2003**, *157* (2–3), 295–300.

[41] Reed Harris, A. E.; Cazaunau, M.; Gratien, A.; Pangui, E.; Doussin, J.-F.; Vaida, V. Atmospheric Simulation Chamber Studies of the Gas-Phase Photolysis of Pyruvic Acid. *The Journal of Physical Chemistry A* **2017**, *121* (44), 8348–8358.

[42] Hohenberg, P.; Kohn, W. Inhomogeneous Electron Gas. *Physical review* **1964**, *136* (3B), B864.

[43] Kohn, W.; Sham, L. J. Self-Consistent Equations Including Exchange and Correlation Effects. *Physical review* **1965**, *140* (4A), A1133.

[44] Walker, M.; Harvey, A. J.; Sen, A.; Dessent, C. E. Performance of M06, M06-2X, and M06-HF Density Functionals for Conformationally Flexible Anionic Clusters: M06 Functionals Perform Better than B3LYP for a Model System with Dispersion and Ionic Hydrogen-Bonding Interactions. *The Journal of Physical Chemistry A* **2013**, *117* (47), 12590–12600.

[45] Kozuch, S.; Martin, J. M. Halogen Bonds: Benchmarks and Theoretical Analysis. *Journal of chemical theory and computation* **2013**, *9* (4), 1918–1931.

[46] Grimme, S. Semiempirical GGA-type Density Functional Constructed with a Long-range Dispersion Correction. *Journal of computational chemistry* **2006**, *27* (15), 1787–1799.

[47] Peverati, R.; Truhlar, D. G. Improving the Accuracy of Hybrid Meta-GGA Density Functionals by Range Separation. *The Journal of Physical Chemistry Letters* **2011**, *2* (21), 2810–2817.

[48] McKechnie, S.; Booth, G. H.; Cohen, A. J.; Cole, J. M. On the Accuracy of Density Functional Theory and Wave Function Methods for Calculating Vertical Ionization Energies. *The Journal of chemical physics* **2015**, *142* (19), 194114.

[49] Wu, T.; Kalugina, Y. N.; Thakkar, A. J. Choosing a Density Functional for Static Molecular Polarizabilities. *Chemical Physics Letters* **2015**, *635*, 257–261.

[50] Xu, P.; Zhang, C.-R.; Wang, W.; Gong, J.-J.; Liu, Z.-J.; Chen, H.-S. Assessment of Ab Initio and Density Functional Theory Methods for the Excitations of Donor-Acceptor Complexes: The Case of the Benzene-Tetracyanoethylene Model. *International journal of molecular sciences* **2018**, *19* (4), 1134.

[51] Yu, L.-J.; Sarrami, F.; O'Reilly, R. J.; Karton, A. Reaction Barrier Heights for Cycloreversion of Heterocyclic Rings: An Achilles' Heel for DFT and Standard Ab Initio Procedures. *Chemical Physics* **2015**, *458*, 1–8.

[52] Friedrich, J.; Yu, H.; Leverentz, H. R.; Bai, P.; Siepmann, J. I.; Truhlar, D. G. Water 26-Mers Drawn from Bulk Simulations: Benchmark Binding Energies for Unprecedentedly Large Water Clusters and Assessment of the Electrostatically Embedded Three-Body and Pairwise Additive Approximations. *The journal of physical chemistry letters* **2014**, *5* (4), 666–670.

[53] Ramabhadran, R. O.; Raghavachari, K. Extrapolation to the Gold-Standard in Quantum Chemistry: Computationally Efficient and Accurate CCSD (T) Energies for Large Molecules Using an Automated Thermochemical Hierarchy. *Journal of chemical theory and computation* **2013**, *9* (9), 3986–3994.

[54] Valeev, E. F.; Daniel Crawford, T. Simple Coupled-Cluster Singles and Doubles Method with Perturbative Inclusion of Triples and Explicitly Correlated Geminals: The CCSD (T) R 12 Model. *The Journal of chemical physics* **2008**, *128* (24), 244113.

[55] Řezáč, J.; Hobza, P. Describing Noncovalent Interactions beyond the Common Approximations: How Accurate Is the "Gold Standard," CCSD (T) at the Complete Basis Set Limit? *Journal of chemical theory and computation* **2013**, *9* (5), 2151–2155.

[56] Dunning, T. H. A Road Map for the Calculation of Molecular Binding Energies. *The Journal of Physical Chemistry A* **2000**, *104* (40), 9062–9080.

[57] Schuurman, M. S.; Muir, S. R.; Allen, W. D.; Schaefer III, H. F. Toward Subchemical Accuracy in Computational Thermochemistry: Focal Point Analysis of the Heat of Formation of NCO and [H, N, C, O] Isomers. *The Journal of chemical physics* **2004**, *120* (24), 11586–11599.

[58] Martin, J. M. Ab Initio Total Atomization Energies of Small Molecules—towards the Basis Set Limit. *Chemical physics letters* **1996**, *259* (5–6), 669–678.

[59] Klopper, W.; Bak, K. L.; Jørgensen, P.; Olsen, J.; Helgaker, T. Highly Accurate Calculations of Molecular Electronic Structure. *Journal of Physics B: Atomic, Molecular and Optical Physics* **1999**, *32* (13), R103.

[60] Ditchfield, R.; Hehre, W. J.; Pople, J. A. Self-consistent Molecular-orbital Methods. IX. An Extended Gaussian-type Basis for Molecular-orbital Studies of Organic Molecules. *The Journal of Chemical Physics* **1971**, *54* (2), 724–728.

[61] Hehre, W. J.; Ditchfield, R.; Pople, J. A. Self—Consistent Molecular Orbital Methods. XII. Further Extensions of Gaussian—Type Basis Sets for Use in Molecular Orbital Studies of Organic Molecules. *The Journal of Chemical Physics* **1972**, *56* (5), 2257–2261.

[62] Dunning Jr, T. H. Gaussian Basis Sets for Use in Correlated Molecular Calculations. I. The Atoms Boron through Neon and Hydrogen. *The Journal of chemical physics* **1989**, *90* (2), 1007–1023.

[63] Peterson, K. A.; Kendall, R. A.; Dunning Jr, T. H. Benchmark Calculations with Correlated Molecular Wave Functions. II. Configuration Interaction Calculations on First Row Diatomic Hydrides. *The Journal of chemical physics* **1993**, *99* (3), 1930–1944.

[64] Woon, D. E.; Dunning Jr, T. H. Gaussian Basis Sets for Use in Correlated Molecular Calculations. III. The Atoms Aluminum through Argon. *The Journal of chemical physics* **1993**, *98* (2), 1358–1371.

[65] Wilson, A. K.; van Mourik, T.; Dunning Jr, T. H. Gaussian Basis Sets for Use in Correlated Molecular Calculations. VI. Sextuple Zeta Correlation Consistent Basis Sets for Boron through Neon. *Journal of Molecular Structure: THEOCHEM* **1996**, *388*, 339–349

[66] Peterson, K. A.; Dunning Jr, T. H. Accurate Correlation Consistent Basis Sets for Molecular Core–Valence Correlation Effects: The Second Row Atoms Al–Ar, and the First Row Atoms B–Ne Revisited. *The Journal of chemical physics* **2002**, *117* (23), 10548–10560.

[67] Møller, K. H.; Otkjær, R. V.; Hyttinen, N.; Kurtén, T.; Kjaergaard, H. G. Cost-Effective Implementation of Multiconformer Transition State Theory for Peroxy Radical Hydrogen Shift Reactions. *The Journal of Physical Chemistry A* **2016**, *120* (51), 10072–10087.

[68] Zheng, J.; Truhlar, D. G. Multi-Path Variational Transition State Theory for Chemical Reaction Rates of Complex Polyatomic Species: Ethanol+ OH Reactions. *Faraday discussions* **2012**, *157*, 59–88.

[69] Yu, T.; Zheng, J.; Truhlar, D. G. Multipath Variational Transition State Theory: Rate Constant of the 1, 4-Hydrogen Shift Isomerization of the 2-Cyclohexylethyl Radical. *The Journal of Physical Chemistry A* **2011**, *116* (1), 297–308.

[70] Chase Jr, M. W. JANAF Thermochemical Table. *J. Phys. Chem. Ref. Data* **1985**, *14*, Supplement No. 1.

[71] Taghikhani, M.; Parsafar, G. A.; Sabzyan, H. Theoretical Investigation of the Hydrogen Abstraction Reaction of the OH Radical with CH3CHF2 (HFC152-a): A Dual Level Direct Density Functional Theory Dynamics Study. *The Journal of Physical Chemistry A* **2005**, *109* (36), 8158–8167.

[72] Gour, N. K.; Mishra, B. K.; Singh, H. J. Theoretical Study on Mechanism, Kinetics, and Thermochemistry of the Gas Phase Reaction of 2, 2, 2-Trifluoroethyl Butyrate with OH Radicals at 298 K. *Journal of Chemical Sciences* **2015**, *127* (6), 1015–1023.

[73] Fukui, K. Formulation of the Reaction Coordinate. *The Journal of Physical Chemistry* **1970**, *74* (23), 4161–4163

[74] Hratchian, H. P.; Kraka, E. Improved Predictor–Corrector Integrators For Evaluating Reaction Path Curvature. *Journal of chemical theory and computation* **2013**, *9* (3), 1481–1488.

[75] Hratchian, H. P. Using Efficient Predictor-Corrector Reaction Path Integrators for Studies Involving Projected Frequencies. *Journal of chemical theory and computation* **2012**, *8* (12), 5013–5019.

[76] Hratchian, H. P.; Schlegel, H. B. Using Hessian Updating to Increase the Efficiency of a Hessian Based Predictor-Corrector Reaction Path Following Method. *Journal of chemical theory and computation* **2005**, *1* (1), 61–69.

[77] Gonzalez, C.; Schlegel, H. B. Reaction Path Following in Mass-Weighted Internal Coordinates. *J. Phys. Chem.* **1990**, *94* (14), 5523–5527.

[78] Qiu, Y. Pushing the Ab Initio Limits for the Accurate Characterization of Small Molecular Systems, University of Georgia, 2015.

[79] Filarowski, A.; Majerz, I. AIM Analysis of Intramolecular Hydrogen Bonding in O-Hydroxy Aryl Schiff Bases. *The Journal of Physical Chemistry A* **2008**, *112* (14), 3119–3126.

[80] Palusiak, M.; Krygowski, T. M. Application of AIM Parameters at Ring Critical Points for Estimation of Π-Electron Delocalization in Six-Membered Aromatic and Quasi-Aromatic Rings. *Chemistry–A European Journal* **2007**, *13* (28), 7996–8006.

[81] Fradera, X.; Austen, M. A.; Bader, R. F. The Lewis Model and Beyond. *The Journal of Physical Chemistry A* **1999**, *103* (2), 304–314.

[82] Poater, J.; Solà, M.; Duran, M.; Fradera, X. New Insights in Chemical Reactivity by Means of Electron Pairing Analysis. *The Journal of Physical Chemistry A* **2001**, *105* (10), 2052–2063.
[83] Fradera, X.; Poater, J.; Simon, S.; Duran, M.; Solà, M. Electron-Pairing Analysis from Localization and Delocalization Indices in the Framework of the Atoms-in-Molecules Theory. *Theoretical Chemistry Accounts* **2002**, *108* (4), 214–224.

[84] Poater, J.; Solà, M.; Duran, M.; Fradera, X. Effects of Solvation on the Pairing of Electrons in a Series of Simple Molecules and in the Menshutkin Reaction. *The Journal of Physical Chemistry A* **2001**, *105* (25), 6249–6257.

[85] Matta, C. F.; Hernández-Trujillo, J. Bonding in Polycyclic Aromatic Hydrocarbons in Terms of the Electron Density and of Electron Delocalization. *The Journal of Physical Chemistry A* **2003**, *107* (38), 7496–7504.

[86] Matito, E.; Duran, M.; Sola, M. The Aromatic Fluctuation Index (FLU): A New Aromaticity Index Based on Electron Delocalization. *The Journal of chemical physics* **2005**, *122* (1), 014109.

[87] Molavian, M. R.; Abdolmaleki, A.; Eskandari, K. Strain or Electronic Effects? MP2 and DFT Aromaticity Investigation in Small Ring Annulated Benzene. *Computational and Theoretical Chemistry* **2017**, *1099*, 102–108.

[88] Poater, J.; Fradera, X.; Duran, M.; Sola, M. The Delocalization Index as an Electronic Aromaticity Criterion: Application to a Series of Planar Polycyclic Aromatic Hydrocarbons. *Chemistry–A European Journal* **2003**, *9* (2), 400–406.

[89] Matito, E.; Solà, M.; Salvador, P.; Duran, M. Electron Sharing Indexes at the Correlated Level. Application to Aromaticity Calculations. *Faraday discussions* **2007**, *135*, 325–345.

[90] Fradera, X.; Solà, M. Electron Localization and Delocalization in Open-shell Molecules. *Journal of computational chemistry* **2002**, *23* (14), 1347–1356

[91] Keith, T. A. AIMAll (Version 13.11. 04). *TK Gristmill Software, Overland Park KS, USA* **2013**.

[92] Westbrook, C. K. Inhibition of Hydrocarbon Oxidation in Laminar Flames and Detonations by Halogenated Compounds. In *Symposium (International) on Combustion*; Elsevier, 1982; Vol. 19, pp 127–141.

[93] Dixon-Lewis, G. Mechanism of Inhibition of Hydrogen-Air Flames by Hydrogen Bromide and Its Relevance to the General Problem of Flame Inhibition. *Combustion and Flame* **1979**, *36*, 1–14.

[94] Saiz-Lopez, A.; Fernandez, R. P.; Ordóñez, C.; Kinnison, D. E.; Gómez Martín, J. C.; Lamarque, J.-F.; Tilmes, S. Iodine Chemistry in the Troposphere and Its Effect on Ozone. *Atmospheric Chemistry and Physics* **2014**, *14* (23), 13119–13143.

[95] Raso, A. R.; Custard, K. D.; May, N. W.; Tanner, D.; Newburn, M. K.; Walker, L.; Moore, R. J.; Huey, L. G.; Alexander, L.; Shepson, P. B. Active Molecular Iodine Photochemistry in the Arctic. *Proceedings of the National Academy of Sciences* **2017**, *114* (38), 10053–10058.

[96] Atkinson, R.; Baulch, D. L.; Cox, R. A.; Crowley, J. N.; Hampson, R. F.; Hynes, R. G.; Jenkin, M. E.; Rossi, M. J.; Troe, J. Evaluated Kinetic and Photochemical Data for Atmospheric Chemistry: Volume III Reactions of Inorganic Halogens. *Atmospheric Chemistry and Physics Discussions* **2006**, *6* (2), 2281–2702.

[97] Mellouki, A.; Talukdar, R. K.; Howard, C. J. Kinetics of the Reactions of HBr with O3 and HO2: The Yield of HBr from HO2+ BrO. *Journal of Geophysical Research: Atmospheres* **1994**, *99* (D11), 22949–22954.

[98] Leu, M.-T. Upper Limits for the Rate Constant for the Reaction Br+ H2O2 Yields HB2+ HO2. **1980**.

[99] Posey, J.; Sherwell, J.; Kaufman, M. Kinetics of the Reactions of Atomic Bromine with HO2 and H2O2. *Chemical Physics Letters* **1981**, *77* (3), 476–479.

[100] Toohey, D. W.; Brune, W. H.; Anderson, J. G. Mechanism and Kinetics of Br+ HO2. Fwdarw. HBr+ O2 and Br+ H2O2. Fwdarw. Products over the Temperature Range 260-390 K. *Journal of Physical Chemistry* **1987**, *91* (5), 1215–1222.

[101] Heneghan, S. P.; Benson, S. W. Kinetic Study of the Reactions of Cl and Br with H2O2. *International journal of chemical kinetics* **1983**, *15* (12), 1311–1319.

[102] Clark, D. R.; Simmons, R. F.; Smith, D. A. Inhibition of the Second Limit of the Hydrogen+ Oxygen Reaction by Hydrogen Bromide. *Transactions of the Faraday Society* **1970**, *66*, 1423–1435.

[103] Dixon-Lewis, G.; Marshall, P.; Ruscic, B.; Burcat, A.; Goos, E.; Cuoci, A.; Frassoldati, A.; Faravelli, T.; Glarborg, P. Inhibition of Hydrogen Oxidation by HBr and Br2. *Combustion and Flame* **2012**, *159* (2), 528–540.

[104] Bell, R. L.; Truong, T. N. Direct Ab Initio Dynamics Studies of Proton Transfer in Hydrogen-bond Systems. *The Journal of chemical physics* **1994**, *101* (12), 10442–10451.

[105] Zhang, F.; Dibble, T. S. Impact of Tunneling on Hydrogen-Migration of the n-Propylperoxy Radical. *Physical Chemistry Chemical Physics* **2011**, *13* (40), 17969–17977.

[106] Garrett, B. C.; Truhlar, D. G. Accuracy of Tunneling Corrections to Transition State Theory for Thermal Rate Constants of Atom Transfer Reactions. *Journal of Physical Chemistry* **1979**, *83* (1), 200–203.

[107] Keyser, L. F. Absolute Rate Constant of the Reaction between Chlorine (2P) Atoms and Hydrogen Peroxide from 298 to 424 K. *The Journal of Physical Chemistry* **1980**, *84* (1), 11–14.

[108] Poulet, G.; Le Bras, G.; Combourieu, J. Kinetic Study of the Reactions of Cl Atoms with HNO3, H2O2, and HO2. *The Journal of Chemical Physics* **1978**, *69* (2), 767–773.

[109] Michael, J. V.; Whytock, D. A.; Lee, J. H.; Payne, W. A.; Stief, L. J. Absolute Rate Constant for the Reaction of Atomic Chlorine with Hydrogen Peroxide Vapor over the Temperature Range 265–400 K. *The Journal of Chemical Physics* **1977**, *67* (8), 3533–3536.

[110] Marouani, S.; Koussa, H.; Bahri, M.; Hochlaf, M.; Batis, H. Ab Initio Calculation on the Rate Constants of the Reaction H2O2+ Cl. *Journal of Molecular Structure: THEOCHEM* **2009**, *905* (1–3), 70–75.

[111] Walther, C.-D.; Wagner, H. G. Über Die Reaktionen von F-Atomen Mit H2O, H2O2 Und NH3. *Berichte der Bunsengesellschaft für physikalische Chemie* **1983**, *87* (5), 403–409.

[112] Smith, D. J.; Setser, D. W.; Kim, K. C.; Bogan, D. J. HF Infrared Chemiluminescence. Relative Rate Constants for Hydrogen Abstraction from Hydrocarbons, Substituted Methanes, and Inorganic Hydrides. *The Journal of Physical Chemistry* **1977**, *81* (9), 898–905.

[113] Chase, M. W., Jr., Ed. NIST-JANAF Thermochemical Tables 4th edn. J. Phys. Chem. Ref. Data **1998**, 1952.

[114] Aguilera-Iparraguirre, J.; Curran, H. J.; Klopper, W.; Simmie, J. M. Calculation of Reaction Rates for Hydrogen Abstraction by the Hydroperoxyl Radical from C1 through C4 Hydrocarbons. *Proc. Euro. Comb. Meet*.

[115] B. Ruscic and D. H. Bross, Active Thermochemical Tables (ATcT) values based on ver.1.122d of the Thermochemical Network (2018); available at ATcT.anl.gov

[116] Ito, A.; Sillman, S.; Penner, J. E. Effects of Additional Nonmethane Volatile Organic Compounds, Organic Nitrates, and Direct Emissions of Oxygenated Organic Species on Global Tropospheric Chemistry. *Journal of Geophysical Research: Atmospheres* **2007**, *112* (D6).

[117] Poisson, N.; Kanakidou, M.; Crutzen, P. J. Impact of Non-Methane Hydrocarbons on Tropospheric Chemistry and the Oxidizing Power of the Global Troposphere: 3-Dimensional Modelling Results. *Journal of Atmospheric Chemistry* **2000**, *36* (2), 157–230.

[118] Atkinson, R. Atmospheric Chemistry of VOCs and NOx. *Atmospheric environment* **2000**, *34* (12–14), 2063–2101.

[119] Noziere, B.; Kalberer, M.; Claeys, M.; Allan, J.; D'Anna, B.; Decesari, S.; Finessi, E.; Glasius, M.; Grgic, I.; Hamilton, J. F. The Molecular Identification of Organic Compounds in the Atmosphere: State of the Art and Challenges. *Chemical reviews* **2015**, *115* (10), 3919–3983.

[120] Mellouki, A.; Wallington, T. J.; Chen, J. Atmospheric Chemistry of Oxygenated Volatile Organic Compounds: Impacts on Air Quality and Climate. *Chemical reviews* **2015**, *115* (10), 3984–4014.

[121] Harrison, R. M.; Yin, J. Particulate Matter in the Atmosphere: Which Particle Properties Are Important for Its Effects on Health? *Science of the total environment* **2000**, *249* (1–3), 85–101.

[122] Perraud, V.; Bruns, E. A.; Ezell, M. J.; Johnson, S. N.; Yu, Y.; Alexander, M. L.; Zelenyuk, A.; Imre, D.; Chang, W. L.; Dabdub, D. Nonequilibrium Atmospheric Secondary Organic Aerosol Formation and Growth. *Proceedings of the National Academy of Sciences* **2012**, *109* (8), 2836–2841.

[123] Epstein, S. A.; Nizkorodov, S. A. A Comparison of the Chemical Sinks of Atmospheric Organics in the Gas and Aqueous Phase. *Atmospheric Chemistry and Physics* **2012**, *12* (17), 8205–8222.

[124] Moortgat, G. K. Important Photochemical Processes in the Atmosphere. *Pure and Applied Chemistry* **2001**, *73* (3), 487–490.

[125] Atkinson, R. Kinetics and Mechanisms of the Gas-Phase Reactions of the Hydroxyl Radical with Organic Compounds under Atmospheric Conditions. *Chemical Reviews* **1986**, *86* (1), 69–201.

[126] Karl, M.; Dorn, H.-P.; Holland, F.; Koppmann, R.; Poppe, D.; Rupp, L.; Schaub, A.; Wahner, A. Product Study of the Reaction of OH Radicals with Isoprene in the Atmosphere Simulation Chamber SAPHIR. *Journal of atmospheric chemistry* **2006**, *55* (2), 167–187.

[127] Goldstein, A. H.; Galbally, I. E. *Known and Unexplored Organic Constituents in the Earth's Atmosphere*; ACS Publications, 2007.

[128] Guenther, A. B.; Jiang, X.; Heald, C. L.; Sakulyanontvittaya, T.; Duhl, T.; Emmons, L. K.; Wang, X. The Model of Emissions of Gases and Aerosols from Nature Version 2.1 (MEGAN2. 1): An Extended and Updated Framework for Modeling Biogenic Emissions. **2012**.

[129] Sindelarova, K.; Granier, C.; Bouarar, I.; Guenther, A.; Tilmes, S.; Stavrakou, T.; Müller, J.-F.; Kuhn, U.; Stefani, P.; Knorr, W. Global Data Set of Biogenic VOC Emissions Calculated by the MEGAN Model over the Last 30 Years. *Atmospheric Chemistry and Physics* **2014**, *14* (17), 9317–9341.

[130] Bardouki, H.; Liakakou, H.; Economou, C.; Sciare, J.; Smolık, J.; Ždímal, V.; Eleftheriadis, K.; Lazaridis, M.; Dye, C.; Mihalopoulos, N. Chemical Composition of Size-Resolved Atmospheric Aerosols in the Eastern Mediterranean during Summer and Winter. *Atmospheric Environment* **2003**, *37* (2), 195–208.

[131] Bao, L.; Matsumoto, M.; Kubota, T.; Sekiguchi, K.; Wang, Q.; Sakamoto, K. Gas/Particle Partitioning of Low-Molecular-Weight Dicarboxylic Acids at a Suburban Site in Saitama, Japan. *Atmospheric environment* **2012**, *47*, 546–553.

[132] Ho, K. F.; Lee, S. C.; Cao, J. J.; Kawamura, K.; Watanabe, T.; Cheng, Y.; Chow, J. C. Dicarboxylic Acids, Ketocarboxylic Acids and Dicarbonyls in the Urban Roadside Area of Hong Kong. *Atmospheric Environment* **2006**, *40* (17), 3030–3040.

[133] Baboukas, E. D.; Kanakidou, M.; Mihalopoulos, N. Carboxylic Acids in Gas and Particulate Phase above the Atlantic Ocean. *Journal of Geophysical Research: Atmospheres* **2000**, *105* (D11), 14459–14471.

[134] Khwaja, H. A. Atmospheric Concentrations of Carboxylic Acids and Related Compounds at a Semiurban Site. *Atmospheric Environment* **1995**, *29* (1), 127–139.

[135] Limbeck, A.; Puxbaum, H.; Otter, L.; Scholes, M. C. Semivolatile Behavior of Dicarboxylic Acids and Other Polar Organic Species at a Rural Background Site (Nylsvley, RSA). *Atmospheric Environment* **2001**, *35* (10), 1853–1862.

[136] Kawamura, K.; Tachibana, E.; Okuzawa, K.; Aggarwal, S. G.; Kanaya, Y.; Wang, Z. F. High Abundances of Water-Soluble Dicarboxylic Acids, Ketocarboxylic Acids and α-Dicarbonyls in the Mountaintop Aerosols over the North China Plain during Wheat Burning Season. *Atmospheric chemistry and physics* **2013**, *13* (16), 8285–8302.

[137] Takahashi, K.; Plath, K. L.; Skodje, R. T.; Vaida, V. Dynamics of Vibrational Overtone Excited Pyruvic Acid in the Gas Phase: Line Broadening through Hydrogen-Atom Chattering. *The Journal of Physical Chemistry A* **2008**, *112* (32), 7321–7331.

[138] da Silva, G. Decomposition of Pyruvic Acid on the Ground-State Potential Energy Surface. *The Journal of Physical Chemistry A* **2015**, *120* (2), 276–283.

[139] Rosado-Reyes, C. M.; Francisco, J. S. Atmospheric Oxidation Pathways of Acetic Acid. *The Journal of Physical Chemistry A* **2006**, *110* (13), 4419–4433.

[140] De Smedt, F.; Bui, X. V.; Nguyen, T. L.; Peeters, J.; Vereecken, L. Theoretical and Experimental Study of the Product Branching in the Reaction of Acetic Acid with OH Radicals. *The Journal of Physical Chemistry A* **2005**, *109* (10), 2401–2409.

[141] Reva, I. D.; Stepanian, S. G.; Adamowicz, L.; Fausto, R. Combined FTIR Matrix Isolation and Ab Initio Studies of Pyruvic Acid: Proof for Existence of the Second Conformer. *The Journal of Physical Chemistry A* **2001**, *105* (19), 4773–4780.

[142] Schellenberger, A.; Beer, W.; Oehme, G. Untersuchungen zur theorie der α-ketosäuren—XI. IR-spektroskopische untersuchungen an α-ketosäuren im gaszustand. *Spectrochimica Acta* **1965**, *21* (7), 1345–1351.

[143] Grosjean, D. Atmospheric Reactions of Pyruvic Acid. *Atmospheric Environment (1967)* **1983**, *17* (11), 2379–2382.

[144] Harris, A. R. A Kinetic and Mechanistic Study of the Photochemistry of Pyruvic Acid: Implications for the Atmosphere. **2017**.

[145] Plath, K. L.; Takahashi, K.; Skodje, R. T.; Vaida, V. Fundamental and Overtone Vibrational Spectra of Gas-Phase Pyruvic Acid. *The Journal of Physical Chemistry A* **2009**, *113* (26), 7294–7303.

[146] Faloona, I. C.; Tan, D.; Lesher, R. L.; Hazen, N. L.; Frame, C. L.; Simpas, J. B.; Harder, H.; Martinez, M.; Di Carlo, P.; Ren, X. A Laser-Induced Fluorescence Instrument for Detecting Tropospheric OH and HO 2: Characteristics and Calibration. *Journal of Atmospheric Chemistry* **2004**, *47* (2), 139–167.

[147] Church, J. R.; Skodje, R. T. Reaction Kinetics of HBr with HO2: A New Channel for Isotope Scrambling Reactions. *The Journal of Physical Chemistry A* **2016**, *120* (43), 8503–8511.

[148] Church, J. R.; Skodje, R. T. Double Hydrogen-Atom Exchange Reactions of HX (X= F, Cl, Br, I) with HO2. *The Journal of Physical Chemistry A* **2018**, *122* (24), 5251–5260.

[149] Brasseur, G. P.; Solomon, S. *Aeronomy of the Middle Atmosphere: Chemistry and Physics of the Stratosphere and Mesosphere*; Springer Science & Business Media, 2006; Vol. 32.

Appendix A

A.1 Hydrogen Halide with HO_2

A.1.1 M11/cc-pVQZ-PP and M11/cc-pVQZ Stationary Point Structures

HO_2

O	-6.4685080345	4.5063745743	0.3206236584
H	-5.5206127040	4.5967157962	0.5012099459
O	-6.5658860405	3.8052029970	-0.7755478186

H_2O_2

O	-6.0520594317	2.4500899137	0.1461284320
H	-5.7473860194	2.3612603950	1.0535417207
O	-4.8913841903	2.0943114202	-0.5879027833
H	-4.6636950961	2.9257641346	-1.0132927263

HF

H	-1.5022166238	-0.6349206300	0.0000000000
F	-2.4215927562	-0.6349206300	0.0000000000

HCl

H	-1.3217999598	-0.6349206300	0.0000000000
Cl	-2.6020094202	-0.6349206300	0.0000000000

HBr

H	-1.2504938167	-0.6349206300	0.0000000000
Br	-2.6733155633	-0.6349206300	0.0000000000

HI

H	-1.1561272170	-0.6349206300	0.0000000000
I	-2.7676821630	-0.6349206300	0.0000000000

Intermediate (F)

O	1.6233619118	0.4827674302	0.2742217450
H	2.5562975243	0.7558036116	0.3925101465
O	1.6676967455	-0.7323710005	-0.1819806639
H	3.4549072744	-0.8310094269	-0.1892405775
F	4.1687966917	-0.2622237868	0.0368868882

Intermediate (Cl)

O	1.5102026166	0.5287712382	0.2896814945
H	2.4504028547	0.7786866962	0.3993174507
O	1.5068711805	-0.6862812346	-0.1674390336
H	3.4662289007	-0.9448203853	-0.2314581651
Cl	4.5373545952	-0.2633894869	0.0422957917

Intermediate (Br)

O	1.4781180216	0.5351122006	0.2913862706
H	2.4186914024	0.7851596973	0.4015252828
O	1.4722853220	-0.6793856277	-0.1656926786
H	3.4345851921	-0.9617862384	-0.2378054982
Br	4.6673802095	-0.2661332042	0.0429841617

Intermediate (I)

O	1.4172117966	0.5632559998	0.3033897687
H	2.3631515410	0.7896317316	0.4060185789
O	1.3746221088	-0.6493975539	-0.1590983964
H	3.4618266577	-1.0336654206	-0.2691259500
I	4.8542480437	-0.2568579293	0.0512135370

TS1 (Cl)

O	-2.3996197608	1.0284724485	0.3178436399
H	-2.7849492431	0.8350026697	-0.5462832188
O	-1.5421996704	0.0011809904	0.5209431973
H	-0.6133963099	0.4447814643	0.7660841450
Cl	0.8114739841	0.9482024271	0.0669922366

TS1 (Br)

O	-2.4523684333	1.0211067541	0.3255088332
H	-2.8279966611	0.8313278589	-0.5458486918
O	-1.6237978012	0.0037006435	0.5638955428
H	-0.5571972974	0.4384804545	0.6649629096
Br	0.9326691929	0.9630242890	0.1170614062

TS1 (I)

O	-2.5406811698	1.0009257037	0.3421515973
H	-2.8348466336	0.8472846053	-0.5678773321
O	-1.7237085117	-0.0036502050	0.6206447059
H	-0.5222568558	0.4176507318	0.5928313329
I	1.0928021707	0.9954291642	0.1378296960

TS2 (F)

O	1.7667036916	0.4343720250	0.2721341717
H	2.8974850762	0.5897544654	0.3419743540
O	1.8492603818	-0.7697706385	-0.1933269124
H	2.9924715365	-0.7961279398	-0.1937136351
F	3.9651394614	-0.0452610846	0.1053295601

TS2 (Cl)

O	1.6947382028	0.4249236459	0.2677889239
H	2.7766263211	0.6568474076	0.3669495310
O	1.7761563115	-0.7679698507	-0.1933238556
H	2.8812824699	-0.8764650962	-0.2257303765
Cl	4.3422568423	-0.0243692791	0.1167133154

TS2 (Br)

O	1.6678680668	0.4224185776	0.2665588636
H	2.7371376734	0.6734873325	0.3730706447
O	1.7488682010	-0.7686743215	-0.1938569953
H	2.8424483121	-0.8984183403	-0.2345475337
Br	4.4747378943	-0.0158464208	0.1211725589

TS2 (I)

O	1.5966372305	0.4223649228	0.2658230672
H	2.5844394046	0.7315371958	0.3938537195
O	1.7169980617	-0.7652036926	-0.1924800381
H	2.9142170172	-0.8724039838	-0.2238031103
I	4.6587684336	-0.1033276147	0.0890038999

C_{2v} intermediate

O	1.6512532091	0.4175418398	0.2646291698
H	2.7155130202	0.6577088821	0.3666902516
O	1.6927158232	-0.7732307228	-0.1959090149
H	2.7712438297	-0.9547456318	-0.2569202730
I	4.6537489142	-0.0954795602	0.0920904774

A.1.2 M11/cc-pVTZ-PP and M11/cc-pVTZ Stationary Point Structures

HO_2

O	-6.4697119641	4.5072956095	0.3220075188
H	-5.5196814935	4.5965233406	0.5009493743
O	-6.5656133214	3.8044744174	-0.7766711074

HCl

H	-1.3215017355	-0.6349206300	0.0000000000
Cl	-2.6023076445	-0.6349206300	0.0000000000

HBr

H	-1.2504959619	-0.6349206300	0.0000000000
Br	-2.6733134181	-0.6349206300	0.0000000000

HI

H	-1.1551520905	-0.6349206300	0.0000000000
I	-2.7686572895	-0.6349206300	0.0000000000

TS1 (Cl)

O	-2.4006499395	1.0284189673	0.3200332362
H	-2.7784696985	0.8374454891	-0.5496971148
O	-1.5388025769	-0.0024169673	0.5192711646
H	-0.6185073681	0.4444608947	0.7764753745
Cl	0.8077385830	0.9497316161	0.0594973394

TS1 (Br)

O	-2.4483362796	1.0244561202	0.3241072460
H	-2.8311933154	0.8293241742	-0.5448362269
O	-1.6186822208	0.0023487430	0.5578452961
H	-0.5626867065	0.4392426977	0.6744643978
Br	0.9322075222	0.9622682649	0.1139992871

TS1 (I)

O	-2.5364034442	1.0046011290	0.3410821131
H	-2.8401898253	0.8449784995	-0.5666815379
O	-1.7200757045	-0.0049137236	0.6160227619
H	-0.5253807201	0.4178218695	0.5973167460
I	1.0933586940	0.9951522257	0.1378399169

TS2 (F)

O	1.7619619340	0.4353749411	0.2724706203
H	2.9052494026	0.5860219313	0.3406092688
O	1.8446955555	-0.7713007332	-0.1939531195
H	2.9996858046	-0.7915306723	-0.1918730666
F	3.9594674508	-0.0455986394	0.1051438352

TS2 (Cl)

O	1.6927880805	0.4258040921	0.2681073454
H	2.7804773926	0.6554406120	0.3664472525
O	1.7743392492	-0.7690725499	-0.1937661558
H	2.8849240752	-0.8746396186	-0.2249876601
Cl	4.3385313501	-0.0245657080	0.1165967561

TS2 (Br)

O	1.6665144105	0.4233563151	0.2669048918
H	2.7381117774	0.6732268028	0.3729860640
O	1.7479575039	-0.7696530048	-0.1942459164
H	2.8450429852	-0.8971825684	-0.2340409795
Br	4.4734334706	-0.0167807171	0.1207934783

TS2 (I)

O	1.5979306065	0.4232861644	0.2663333298
H	2.5906126116	0.7289779051	0.3931331503
O	1.7158351761	-0.7662182276	-0.1930563989
H	2.9102917250	-0.8741784171	-0.2247188285
I	4.6563900284	-0.0989005974	0.0907062854

A.1.3 M06-2X/DZP Stationary Point Structures

TS1 (Cl)

O	-2.4037839224	1.0333115568	0.3231980888
H	-2.7965519769	0.8309014201	-0.5489273266
O	-1.5370828126	-0.0026590542	0.5100276425
H	-0.6158830349	0.4523644922	0.7741837346
Cl	0.8246107467	0.9437215851	0.0670978606

TS1 (Br)

O	-2.4457147051	1.0293800873	0.3270599036
H	-2.8386590823	0.8269165000	-0.5470166244
O	-1.6127322146	-0.0009212038	0.5512997030
H	-0.5529892032	0.4460747520	0.6761647317
Br	0.9214042052	0.9561898644	0.1180722861

TS1 (I)

O	-2.5283320988	1.0130674630	0.3348154990
H	-2.8837081207	0.8362553954	-0.5620107174
O	-1.7132773801	-0.0079125003	0.5811698656
H	-0.4954468650	0.4361609325	0.6306513031
I	1.0920734644	0.9800687094	0.1409540496

TS2 (F)

O	1.7599572453	0.4370378495	0.2731131386
H	2.9158302354	0.5801508768	0.3384231843
O	1.8429372958	-0.7731573137	-0.1947190760
H	3.0094006055	-0.7845369822	-0.1890450816
F	3.9429347655	-0.0465276029	0.1046253728

TS2 (Cl)

O	1.6880869490	0.4266598558	0.2684017927
H	2.7914937093	0.6552041042	0.3664437214
O	1.7697973192	-0.7704289509	-0.1943312643
H	2.8959070798	-0.8731258973	-0.2243105468
Cl	4.3257750903	-0.0253422843	0.1161938353

TS2 (Br)

O	1.6608546722	0.4241107515	0.2671787866
H	2.7486519049	0.6795528687	0.3754839868
O	1.7423977100	-0.7709984283	-0.1948051269
H	2.8565121811	-0.9022816974	-0.2359424181
Br	4.4626436793	-0.0174166670	0.1204823098

TS2 (I)

O	1.6431827295	0.4190854983	0.2651800013
H	2.7355152090	0.6628014641	0.3687984751
O	1.6843137181	-0.7753621707	-0.1967853306
H	2.7890715028	-0.9598117560	-0.2587617618
I	4.6323916369	-0.0949182285	0.0921492269

A.2 Pyruvic Acid with OH and HO_2

A.2.1 M11/cc-pVTZ Stationary Point Structures

Pyruvic Tc

O	-7.4171756547	3.6308370738	0.0627590448
C	-6.2854358284	3.9549140548	0.2631553398
C	-5.5117647498	3.5369042851	1.5393389477
O	-5.5480941741	4.6975046100	-0.5527965856
C	-6.2580159127	2.6988433023	2.5187194669
O	-4.3729137409	3.9147377657	1.6490876477
H	-4.6752466560	4.8008752618	-0.1373159851
H	-7.1610697064	3.2313080827	2.8265517510
H	-5.6273333129	2.4662704066	3.3732552236
H	-6.5988502643	1.7884851571	2.0197051491

Pyruvic Tt

O	-7.3212778587	4.2104856937	0.7501268297
C	-6.1640441834	3.9957019723	0.5190487672
C	-5.3123398470	3.0197670683	1.3664112083
O	-5.4716398584	4.5523679041	-0.4717488310
C	-6.0598005364	2.3710375195	2.4908943046
O	-4.1604865818	2.8405797913	1.0965837454
H	-6.9159852133	1.8241023934	2.0896116383
H	-6.4684059302	3.1420265651	3.1479474760
H	-5.3937596048	1.7066021515	3.0360581594
H	-6.0651003861	5.1443389409	-0.9523232979

HO2

O	-7.9326186490	4.1390193675	-0.0142449704
O	-6.6273235565	4.2092115394	0.0248247072
H	-8.2560377945	4.8233890931	0.5936802632

OH

H	-10.0538643661	4.4156700000	0.0000000000
O	-9.0822356339	4.4156700000	0.0000000000

H2O2

H	-3.1350235978	4.8236904559	1.0958536006
O	-3.2285273478	3.3100182073	-0.0003463994
O	-2.6800326657	4.5918793347	0.2792744727
H	-3.7270863888	3.4838120021	-0.8058116739

H2O

O	-6.5206146622	0.7016656493	-0.0094960259
H	-5.5629215781	0.6879393910	0.0197578260
H	-6.8093637597	0.3135549598	0.8176581999

CO2

C	-8.7514965771	5.2097140269	0.0000000000
O	-7.6025773059	5.0832787365	0.0000000000
O	-9.9004161169	5.3361472366	-0.0000000000

P1

O	-4.4274147983	3.4525541219	0.0072643842
C	-4.5163876175	3.5849124296	1.1915500595
C	-5.8328172060	3.3606856649	1.9662387288
O	-3.5217732172	3.9353996519	1.9952186490
C	-6.9732478899	2.9798937208	1.2045003813
O	-5.8180165737	3.5221313915	3.1779228632
H	-3.8803520786	3.9644932557	2.8989841125
H	-7.9116840290	2.8147720136	1.7167022323
H	-6.8846544898	2.8623830600	0.1329257493

P2

O	-4.4867442317	3.4460061941	-0.0487936380
C	-4.5333944827	3.5894779407	1.1419848951
C	-5.8172121507	3.3696965278	1.9671586241
O	-3.5020117256	3.9513960634	1.8996926795
C	-6.9627329921	2.9784206804	1.2076571174
O	-5.8105484065	3.5284126136	3.1708958949
H	-2.7376348749	4.0709195273	1.3210206784
H	-7.8917329666	2.8102918310	1.7355913243
H	-6.8939270494	2.8561524416	0.1356406942

P3/P4

C	-5.5300596636	3.7870603101	1.7928104515
C	-6.1919123287	2.5829360226	2.4184245944
O	-4.6675970000	4.4551890585	2.2250190403
H	-7.2599393053	2.7852822802	2.5044237391
H	-5.7555407324	2.3701258364	3.3962109731
H	-6.0685809699	1.7350464921	1.7440012016

P5

C	1.2201464300	0.9709028816	1.8258037883
C	1.0057707463	-0.2557061413	1.0031727726
C	0.9499440688	-0.0593008152	-0.5331399689
O	0.8458761477	-1.3689255671	1.4316653640
O	-0.1904177016	0.6545379632	-0.8858688919
O	0.8065424303	-1.2708989613	-1.1628274009
H	0.4822129037	1.7251205126	1.5399044241
H	2.2056170640	1.3796504615	1.5912379406
H	1.1403793360	0.7337325409	2.8840635088
H	0.6994635353	-1.9353245662	-0.4610701370
H	2.0789328848	0.7321137487	-1.8631835102
O	2.0832337547	0.6379252025	-0.9038610394

P6

C	0.8892274779	0.0952143658	-1.0894979772
O	0.1800252321	1.0577309050	-0.9911680858
O	0.4710883463	-1.1513157103	-1.3138262070
H	-0.4895634865	-1.1203448808	-1.3790196844
H	2.4856640245	1.0155765410	-0.8301469069
O	2.2194394257	0.1039586293	-0.9917111287

P7

C	0.1701925370	-1.5561175530	0.8701305901
O	-0.6062209631	-2.2759275514	1.3724080240
O	1.2232303480	-1.8909504419	0.1210710605
H	1.6830106880	-1.0925501336	-0.1567373347

P7 (acetic)

C	1.0680562406	-0.9031861628	-0.0000027826
C	0.0013001752	0.1518289183	0.0000071864
O	0.1790414513	1.3379488951	0.0000517217
O	-1.2379694048	-0.3877730531	-0.0000348977
H	2.0456119185	-0.4287541113	-0.0000372460
H	0.9501435908	-1.5358657563	0.8807856189
H	0.9500951527	-1.5359135428	-0.8807505198
H	-1.8670501243	0.3446538129	-0.0000190808

P6

C	1.0868302636	0.6174508317	-0.6300358181
C	0.7299212461	-0.6196573603	0.2619722843
O	1.9495900445	0.1157069414	-1.5357080813
O	-0.3038518545	-1.2107106177	0.2459682934
O	1.7696425126	-0.9211276510	1.0545597398
H	1.5302053355	-1.6876007986	1.5919936802
H	2.4502272498	1.3367679972	0.5380764565
O	1.6111441965	1.6363466448	0.1740128543
C	-0.1745500806	1.1361193802	-1.3177934407
H	-0.6444291650	0.3270554449	-1.8716342067
H	0.1088925580	1.9497645265	-1.9837537710
H	-0.8516145265	1.5056916610	-0.5486156908

PRC1

C	1.9079966494	-0.0459001499	-1.3758434127
C	1.2023540665	0.1642129360	-0.0859217436
C	-0.3240227385	-0.1017291799	-0.0786689120
O	1.7051431258	0.5218772352	0.9553254202
O	-0.9102173375	-0.4569475924	-1.0552152023
O	-0.8754847004	0.1084005260	1.1091933341
H	2.9700555574	0.1674055261	-1.2735736797
H	1.4433896151	0.5890463023	-2.1346596368
H	1.7361474033	-1.0745178468	-1.7033874697
H	-0.1734465927	0.3892196483	1.7183795865
H	3.6569810863	0.8524794987	0.9176411411
O	4.5650135949	0.9176522087	0.5602132377

PRC2

C	1.8982732725	-0.0258970819	-1.4160787044
C	1.2305316854	0.0741878594	-0.0845421512
C	-0.2767172897	-0.2722335298	-0.0895724223
O	1.7583831546	0.3915137905	0.9479064097
O	-0.8563065110	-0.5933621615	-1.0879111856
O	-0.8264341835	-0.1707975902	1.1165467510
H	2.9515792692	0.2327642315	-1.3281895122
H	1.3860954862	0.6330757936	-2.1213488600
H	1.7705173187	-1.0398971694	-1.8027508663
H	-1.7622617311	-0.3996885188	1.0405110408
H	3.6554965948	0.8102913982	0.8683490058
O	4.5588030989	0.9494064933	0.5161547599

PRC3

C	-1.1133873545	-1.4706988969	1.3894928073
C	-0.1735852275	-0.6802443882	0.5447073600
C	-0.8218320981	0.4809914980	-0.2553747856
O	1.0115248495	-0.8873604950	0.4545933433
O	-1.9975133124	0.6861698905	-0.1650076951
O	-0.0019562077	1.1891867407	-1.0085943525
H	-0.5749512969	-2.2574484407	1.9121728055
H	-1.9014248675	-1.8823314392	0.7546271382
H	-1.6140197239	-0.7980118695	2.0896673565
H	0.9278549039	0.8902263214	-0.9695569877
H	2.6426202887	-0.1520640670	-0.5002957916
O	2.7866082347	0.5829627221	-1.1287475666

PRC4

C	1.8982732725	-0.0258970819	-1.4160787044
C	1.2305316854	0.0741878594	-0.0845421512
C	-0.2767172897	-0.2722335298	-0.0895724223
O	1.7583831546	0.3915137905	0.9479064097
O	-0.8563065110	-0.5933621615	-1.0879111856
O	-0.8264341835	-0.1707975902	1.1165467510
H	2.9515792692	0.2327642315	-1.3281895122
H	1.3860954862	0.6330757936	-2.1213488600
H	1.7705173187	-1.0398971694	-1.8027508663
H	-1.7622617311	-0.3996885188	1.0405110408
H	3.6554965948	0.8102913982	0.8683490058
O	4.5588030989	0.9494064933	0.5161547599

TS1-OH

C	1.9934433597	0.1390248443	-1.2242512679
C	1.1248008050	0.3937565276	-0.0534461495
C	-0.2246609613	-0.3648674585	0.0251589403
O	1.3976499989	1.1461064217	0.8524282512
O	-0.5735360070	-1.1416652852	-0.8105730786
O	-0.9180228911	-0.0456581285	1.1091100333
H	3.1095225493	-0.0097979976	-0.7623221911
H	2.0905370861	1.0263566166	-1.8493641299
H	1.7240184089	-0.7498987410	-1.7880940010
H	-0.3965415583	0.5994500925	1.6147531238
H	3.7173753178	0.8614987666	0.6083884193
O	4.1297030821	0.2121183316	0.0150589700

TS2-OH

C	2.0198469199	0.1019823055	-1.2097596081
C	1.1699511440	0.3036890777	-0.0026165285
C	-0.2123128834	-0.3906233646	-0.0382195814
O	1.4900511582	0.9512245701	0.9557070470
O	-0.5576258653	-1.0957782173	-0.9434612388
O	-0.9434435999	-0.1104216771	1.0355546175
H	3.1729490294	0.0921916575	-0.8018410772
H	1.9800943100	0.9686958108	-1.8703438804
H	1.8224635036	-0.8248802621	-1.7419496695
H	-1.7879600218	-0.5729707636	0.9528283188
H	3.6979578856	0.8780825608	0.6236371939
O	4.1808736397	0.3879902122	-0.0627302432

TS3-OH

C	-1.0637381210	-1.4280696629	1.3793962956
C	-0.1033847239	-0.6586259727	0.5322576920
C	-0.7743294600	0.5289622797	-0.3368417182
O	1.0672327564	-0.9215285224	0.4823460954
O	-1.9704609128	0.6076215937	-0.2164780201
O	0.0482210690	1.1886285320	-1.0302393027
H	-0.5522063895	-2.2076755963	1.9377811986
H	-1.8362178262	-1.8327454330	0.7225494468
H	-1.5698748277	-0.7169523222	2.0355541845
H	1.2409684260	0.9024259608	-0.8797516156
H	2.5580248207	-0.1880601748	-1.1543559030
O	2.3032485190	0.5590412081	-0.5990260733

TS4-OH

C	-1.0965904673	-1.3741378245	1.3216794859
C	0.0449450790	-0.7366440965	0.5922234277
C	-0.3587518812	0.2714453006	-0.5324560179
O	1.2046116668	-0.9318648741	0.7909654319
O	-1.5729572879	0.3769861372	-0.8004125901
O	0.5464935587	0.9193559645	-1.1136056693
H	-0.7139948962	-2.0507435677	2.0821818588
H	-1.7285231135	-1.9058767982	0.6066123530
H	-1.7195588240	-0.5957580369	1.7685921527
H	-0.1785344787	1.5545060043	-1.8508611334
H	-1.6273437828	1.3072390227	-2.8847490733
O	-1.2604253931	1.9343715887	-2.2480898060

TS5-OH

C	1.1277099457	0.9718041032	1.8258064577
C	1.0097200877	-0.2725481833	1.0166299189
C	0.6903703975	-0.0797184120	-0.4915341728
O	1.1307373171	-1.4017290807	1.4107049409
O	0.2176627546	0.9906564361	-0.9223423147
O	0.4781562430	-1.2327433742	-1.1210296218
H	0.1716308432	1.5002530217	1.7966548352
H	1.8622995133	1.6258070408	1.3513595987
H	1.4077590041	0.7302251981	2.8482213238
H	0.7401950333	-1.9428404831	-0.5120169475
H	2.1992078940	0.7041451217	-1.8677828974
O	2.3292412364	0.5046634317	-0.9270728911

TS6-OH

C	1.1381396536	1.0080617839	1.6981153951
C	1.0949881856	-0.2635906801	0.9081589829
C	0.5976901344	-0.0349798392	-0.6297112295
O	1.2412282813	-1.3702443691	1.2894450013
O	0.1472543004	1.0335038542	-0.9669943135
O	0.3420838113	-1.1959415785	-1.2254638813
H	0.1124838381	1.3572490631	1.8371089758
H	1.6751225562	1.7700122188	1.1365802742
H	1.6060884057	0.8138692029	2.6606954168
H	-0.1435363393	-1.0116363587	-2.0391175912
H	2.4983629775	1.0676995957	-1.1239853704
O	2.5336488251	0.1588893168	-0.7877580803

TS7-OH

C	0.9778368268	0.4304686384	-0.7963012308
C	0.7025413164	-0.6136735747	0.3148310394
O	2.0918283930	0.3594919201	-1.3619381633
O	-0.3616188135	-0.7550805427	0.8310682909
O	1.7944372716	-1.3162300688	0.6194676022
H	2.4837554917	-1.0661160679	-0.0184371762
H	2.4495094958	1.4749958652	0.5781636170
O	1.5853258747	1.7837698333	0.2581849906
C	-0.2228165445	1.0669823018	-1.4188145715
H	-0.6868740092	0.3301425485	-2.0791134197
H	0.0897747450	1.9340247493	-1.9972018036
H	-0.9406890979	1.3373824977	-0.6465959150

TS8-OH

C	0.9865200445	0.3977641816	-0.8142656631
C	0.6825660380	-0.6314250533	0.2923282854
O	2.0644265517	0.3095123474	-1.4221396433
O	-0.4205880313	-1.0118776893	0.5560103803
O	1.7965725668	-1.0562262154	0.9007973424
H	1.5414666355	-1.7023438600	1.5718193936
H	2.5210593253	1.2864550791	0.5380839621
O	1.6955645060	1.7150730928	0.2539138495
C	-0.2245792552	1.0753342459	-1.3842227951
H	-0.7678618369	0.3446586205	-1.9876899021
H	0.1005519846	1.9052743245	-2.0080900223
H	-0.8827092990	1.4140509362	-0.5857491075

$P3^{a}$-HO_2

O	-7.3581444454	3.9205070385	0.2449362862
C	-6.1742306212	3.9556428156	0.4388492862
C	-5.4723998558	3.1330229336	1.4783001807
O	-5.3367532114	4.7379020264	-0.2537995329
C	-6.1776079970	2.3122154286	2.2411556364
O	-4.1338586086	3.3352047442	1.5179461352
H	-7.2468707051	2.2583370627	2.0913760513
H	-5.7120927781	1.6993480878	3.0044590853
H	-3.7423496085	2.7833696779	2.1996163160
H	-5.8708594488	5.2258894047	-0.8932587443

P3^{b}-HO_2

C	0.7782804957	-0.0756797878	-0.0326958674
C	-0.7336864045	-0.0566499911	0.0195789666
O	1.3549554916	1.1134217912	-0.2960965503
H	0.6911401296	1.7520347034	-0.5733493174
O	1.4178887599	-1.0593873947	0.1625484444
O	-1.2420675211	-1.2650353532	-0.2830107394
C	-1.4271235279	1.0181260309	0.3779604511
H	-2.5087713307	0.9957704976	0.4478004658
H	-0.9273961614	1.9305711172	0.6741693375
H	-2.1931987914	-1.2715796536	-0.1461536009

P5-HO_2

C	-0.8875152161	-0.0347619111	0.0100008405
O	-1.9534994040	0.1880172900	-0.7226782297
C	-1.3367914082	-0.3146632089	1.4032188428
H	-0.8334377495	0.4014133037	2.0599054082
H	-2.4202464933	-0.2818232971	1.5516227117
H	-1.6739653889	0.3700004315	-1.6263984005
H	-0.9365943400	-1.2933826082	1.6851788271

P6-HO_2

C	-7.7502652290	4.1903153202	0.7217822119
C	-6.3425501479	3.6933260098	0.6914633378
C	-5.3616930482	3.9403481823	1.7321179475
O	-5.9912962176	3.2073014003	-0.5248094420
O	-5.9790189501	2.7814570420	1.8793200024
O	-4.4987119562	4.5542951469	2.2638487528
H	-5.0426271720	3.0625648439	-0.5863409016
H	-7.8405111640	5.0511195884	0.0582861380
H	-8.0340289293	4.4758816211	1.7327856812
H	-8.4087364998	3.3979919791	0.3613385408

TS1-HO_2

O	-4.3224488055	2.9643504776	0.2706314156
C	-4.5106756697	3.4226383402	1.3568721930
C	-5.8988957059	3.4174001283	2.0368785366
O	-3.5841694255	3.9899554433	2.1173310836
C	-6.9726762627	2.7519663155	1.3268378311
O	-5.9904248592	3.9018294088	3.1492493593
H	-4.0175129446	4.2682167157	2.9413917809
H	-7.9781697602	3.0070348025	1.6436925513
H	-6.8219435582	1.5300872563	1.9320798195
H	-6.7982986691	2.5237523950	0.2810540183
O	-6.6515537174	0.6519149373	2.6710375621
O	-5.5288797637	0.9940015339	3.3696143849
H	-5.8665600883	1.4242263354	4.1684913738

TS2-HO_2

O	-7.4474078260	4.3397033262	0.4923062883
C	-6.2695944065	4.2044243547	0.2832263193
C	-5.5265082031	3.7532469895	1.7206655914
O	-5.5057735259	4.3783467189	-0.6819466911
C	-6.2001781863	2.6159761624	2.4216434935
O	-4.6559251509	4.4352510976	2.1662369080
H	-3.4391917156	4.9944504682	0.8809366632
O	-3.3153350079	3.4407459539	-0.1413690222
O	-2.7293721214	4.5383726960	0.3748577461
H	-4.2756912391	3.7809924885	-0.4468370968
H	-7.2612577805	2.8546051222	2.5014276498
H	-5.7438704777	2.4601925551	3.3970478538
H	-6.1067350892	1.7230118269	1.7992043466

TS3-HO_2

O	-7.3531525411	4.0253250235	0.3667697736
C	-6.1600950597	3.9907768424	0.4436699628
C	-5.4335131874	3.1674947418	1.5038365401
O	-5.3182113365	4.6423177622	-0.3528883222
C	-6.1649399270	2.3453353142	2.3619482257
O	-4.1834208817	3.3601736914	1.5995828896
H	-7.2338299102	2.3193716945	2.1990811390
H	-5.7026134675	2.8193410679	3.5043839833
H	-5.6849562731	1.3896306407	2.5759140427
O	-3.6705819014	2.5845304905	3.8605909458
O	-4.7586564700	2.9681961387	4.4508235760
H	-3.8345200818	2.8978452002	2.5385092974
H	-5.8381786425	5.1358116222	-1.0010819239

TS4-HO_2

C	0.8299703649	0.0215799518	0.0359153113
C	-0.7075821396	-0.0298404919	0.0042683982
O	1.3394394070	1.0342101600	-0.5379028122
H	0.6493067159	1.7524026417	-1.2914975022
O	1.3406991698	-0.8776445300	0.6595488183
O	-1.2073529578	-1.1032293902	-0.5092518478
C	-1.4715768337	1.0487808244	0.4659119311
H	-2.5284454489	0.8699874476	0.6541189035
H	-0.9632060183	1.6656503003	1.2034335633
H	-2.1720281867	-1.1357285310	-0.4394218130
O	0.0778192437	2.4475776560	-2.0486785080
O	-1.1480549002	2.6363258891	-1.6810364466
H	-1.3733706060	1.7827460820	-0.5431350558

TS5-HO_2

C	1.5648055819	-0.1959505781	-0.1155360310
C	-0.8719081617	-0.0801656807	-0.0820428792
O	1.6525963928	-0.3566258451	1.0292032042
O	1.8234794806	-0.0535862855	-1.2518431676
O	-1.8586611783	0.0803753719	-0.8952512782
C	-1.3487437993	-0.2481927261	1.3138110696
H	-0.8647533243	0.5207191640	1.9246169793
H	-2.4347567367	-0.2106789661	1.4210802579
H	-1.5205894975	0.1898084304	-1.8134907526
H	-0.9468538332	-1.1942338516	1.6905792237
O	-0.8260755482	0.3717982555	-3.3953259090
O	0.4576602657	0.3319158570	-3.5786048339
H	0.8824635483	0.1905758344	-2.6998929333

TS6-HO_2

C	-7.7766910874	4.1057179926	0.6675813481
C	-6.3284879729	3.7887065731	0.6175974982
C	-5.4280344295	3.8743822717	1.7777770502
O	-5.8704682367	3.3408475204	-0.5100598855
O	-5.9520237420	2.7787108002	2.1076384133
O	-4.5189582030	4.5741692409	2.1825354450
H	-3.3330191881	4.8100114738	1.1185978036
O	-3.2376999110	3.9311706753	-0.5040733174
O	-2.6868786375	4.7329835138	0.3517845911
H	-4.8829553681	3.4144544917	-0.5340374351
H	-7.9401225707	5.0165091347	0.0856310931
H	-8.1073487451	4.2573207310	1.6916753540
H	-8.3384211079	3.2956794307	0.2002560614

Appendix B

B.1 CBS Energetics for HO_2+HX

Table B.1 Energetics of Reactants and Products for HO_2+HX. These were calculated from M11/cc-pVXZ where X=D,T,Q as well as the CBS energies determined from a power fit.

M11/cc-pVXZ	cc-pVDZ	cc-pVTZ	cc-pVQZ	CBS
F	-99.699370	-99.745437	-99.752471	-99.761834
Cl	-460.117998	-460.141965	-460.146519	-460.151138
Br	-416.863216	-416.891403	-416.893562	-416.899897
I	-295.545024	-295.558608	-295.561723	-295.564190
HO_2	-150.856613	-150.922488	-150.934028	-150.947000
H_2O_2	-151.495247	-151.567690	-151.581747	-151.595626
HF	-100.411896	-100.468262	-100.480966	-100.491266
HCl	-460.780720	-460.811001	-460.816929	-460.822716
HBr	-417.506849	-417.538698	-417.541693	-417.548694
HI	-296.166842	-296.183951	-296.188122	-296.191159

Table B.2 Energetics of Pre-Reactive Complexes HO_2+HX. These were calculated from M11/cc-pVXZ where X=D,T,Q as well as the CBS energies determined from a power fit.

M11/cc-pVXZ	cc-pVDZ	cc-pVTZ	cc-pVQZ	CBS
Intermediate (F)	-251.291044	-251.406753	-251.429181	-251.451355
Intermediate (Cl)	-611.650269	-611.742859	-611.759900	-611.777900
Intermediate (Br)	-568.374949	-568.469809	-568.483921	-568.503307
Intermediate (I)	-447.032747	-447.113658	-447.128508	-447.144249

Table B.3 Energetics of Transition State Structures HO_2+HX. These were calculated from M11/cc-pVXZ where X=D,T,Q as well as the CBS energies determined from a power fit.

M11/pVXZ	cc-pVDZ	cc-pVTZ	cc-pVQZ	CBS
TS1 (Cl)	-611.614526	-611.706163	-611.723207	-611.740971
TS1 (Br)	-568.352095	-568.446625	-568.460444	-568.479831
TS1 (I)	-447.017825	-447.098446	-447.112902	-447.128683
TS2 (F)	-251.272726	-251.383448	-251.405120	-251.426279
TS2 (Cl)	-611.639526	-611.727476	-611.744024	-611.761020
TS2 (Br)	-568.368735	-568.460386	-568.473785	-568.492582
TS2 (I)	-447.029085	-447.106450	-447.120492	-447.135587
C2V (I)	-447.029120	-447.106708	-447.120823	-447.135953

B.2 CBS Energetics for HO_2+PA and OH+PA

B.2.1 M11/CBS

B.2.1.1 PA+OH

Table B.4 Energetics of Reactants and Products of PA+OH Reactions using M11/cc-pVXZ. Here X=D,T,Q as well as the CBS energies determined from a power fit.

M11/cc-pVXZ	cc-pVDZ	cc-pVTZ	cc-pVQZ	CBS
Pyruvic Tc	-342.277101	-342.410035	-342.438282	-342.463056
Pyruvic Tt	-342.272515	-342.405301	-342.433291	-342.458102
OH	-75.700976	-75.738395	-75.745247	-75.752531
H_2O	-76.392270	-76.436922	-76.447129	-76.455248
CO_2	-188.525342	-188.601646	-188.615492	-188.630381
P1	-341.616883	-341.747445	-341.774971	-341.799365
P2	-341.611892	-341.742229	-341.769490	-341.793903
P3/P4	-153.105009	-153.166370	-153.178660	-153.190307
P5	-417.997520	-418.160744	-418.194757	-418.225366
P6	-264.927924	-265.037255	-265.060034	-265.080538
P7	-189.033474	-189.110605	-189.125937	-189.140611
P7 (acetic)	-228.994860	-229.088824	-229.108566	-229.126141
P8	-418.015395	-418.179700	-418.214001	-418.244795

Table B.5 Energetics of Pre-Reactive Complexes of PA+OH Reactions using M11/cc-pVXZ. Here X=D,T,Q as well as the CBS energies determined from a power fit.

M11/cc-pVXZ	cc-pVDZ	cc-pVTZ	cc-pVQZ	CBS
PRC1	-417.991011	-418.156149	-418.190667	-418.221605
PRC2	-417.987855	-418.152843	-418.187210	-418.218153
PRC3	-417.994393	-418.159475	-418.193628	-418.224655
PRC4	-417.996217	-418.159777	-418.193303	-418.224133

Table B.6 Energetics of Transition State Structures of PA+OH Reactions using M11/cc-pVXZ. Here X=D,T,Q as well as the CBS energies determined from a power fit.

M11/cc-pVXZ	cc-pVDZ	cc-pVTZ	cc-pVQZ	CBS
TS1	-417.973088	-418.140103	-418.174691	-418.206072
TS2	-417.969579	-418.136284	-418.170781	-418.202111
TS3	-417.975491	-418.140765	-418.174637	-418.205792
TS4	-417.978437	-418.141661	-418.174543	-418.205472
TS5	-417.970475	-418.135636	-418.169598	-418.200699
TS6	-417.962676	-418.130186	-418.164656	-418.196192
TS7	-417.971367	-418.137266	-418.171387	-418.202624
TS8	-417.970811	-418.136548	-418.170414	-418.201684

B.2.1.2 PA+HO_2

Table B.7 Energetics of Reactants and Products of PA+HO_2 Reactions. This table neglects any reactants and products that were also produced by PA+OH. These were calculated from M11/cc-pVXZ where X=D,T,Q as well as the CBS energies determined from a power fit.

M11/cc-pVXZ	cc-pVDZ	cc-pVTZ	cc-pVQZ	CBS
HO_2	-150.856648	-150.922499	-150.934018	-150.946989
H_2O_2	-151.495316	-151.567704	-151.581733	-151.595606
$P3^a$-HO_2	-342.258237	-342.392802	-342.421519	-342.446562
$P3^b$-HO_2	-342.247125	-342.383175	-342.412330	-342.437616
P4/P5-HO_2	-153.673339	-153.736279	-153.750209	-153.761782
P6-HO_2	-342.229370	-342.364028	-342.392012	-342.417286

Table B.8 Energetics of Transition State Structures of PA+HO_2 Reactions. These were calculated from M11/cc-pVXZ where X=D,T,Q as well as the CBS energies determined from a power fit.

M11/cc-pVXZ	cc-pVDZ	cc-pVTZ	cc-pVQZ	CBS
TS1-HO2	-493.101401	-493.297078	-493.336380	-493.373491
TS2-HO2	-493.090756	-493.286108	-493.324804	-493.362006
TS3-HO2	-493.102138	-493.291872	-493.330100	-493.366050
TS4-HO2	-493.083829	-493.278062	-493.317261	-493.354046
TS5-HO2	-493.089043	-493.284925	-493.322899	-493.360435
TS6-HO2	-493.114273	-493.309076	-493.347772	-493.384839

B.2.2 CCSD(T)/CBS

Table B.9 Energetics of Reactants and Products of PA+OH Reactions Using CCSD(T). These were calculated from CCSD(T)/cc-pVXZ//M11/cc-pVTZ where X=D,T,Q as well as the CBS energies determined from a power fit.

CCSD(T)/cc-pVXZ	cc-pVDZ	cc-pVTZ	cc-pVQZ	CBS
pyruvic Tc	-341.563309	-341.905005	-342.010520	-342.064906
pyruvic Tt	-341.559959	-341.900760	-342.006104	-342.060318
OH	-75.559271	-75.637684	-75.661590	-75.674158

Table B.9 Energetics of Pre-Reactive Complexes of PA+OH Reactions Using CCSD(T). These were calculated from CCSD(T)/cc-pVXZ//M11/cc-pVTZ where X=D,T,Q as well as the CBS energies determined from a power fit.

CCSD(T)/cc-pVXZ	cc-pVDZ	cc-pVTZ	cc-pVQZ	CBS
PRC1	-417.130695	-417.549828	-417.679813	-417.746366
PRC2	-417.128535	-417.546970	-417.676038	-417.742679
PRC3	-417.125742	-417.545541	-417.681329	-417.746408
PRC4	-417.128147	-417.546352	-417.681504	-417.746370

Table B.10 Energetics of Transition State Structures of PA+OH Reactions Using CCSD(T). These were calculated from CCSD(T)/cc-pVXZ//M11/cc-pVTZ where X=D,T,Q as well as the CBS energies determined from a power fit.

CCSD(T)/cc-pVXZ	cc-pVDZ	cc-pVTZ	cc-pVQZ	CBS
TS1	-417.111068	-417.533196	-417.662853	-417.730237
TS2	-417.108523	-417.529866	-417.659441	-417.726655
TS3	-417.107658	-417.528991	-417.659300	-417.726305
TS4	-417.114942	-417.534265	-417.664460	-417.731001
TS5	-417.111071	-417.533399	-417.663197	-417.730591
TS6	-417.102769	-417.524494	-417.654537	-417.721714
TS7	-417.113766	-417.536072	-417.665643	-417.733096
TS8	-417.114076	-417.535382	-417.664841	-417.732079

Appendix C

C.1 Vibrational Frequencies for HO_2+HX

Table C.1 Harmonic Frequncies of HO_2+HF systems determined from the M11/cc-pVQZ stationary point structure.

HF	3976.8								
DF	2883.0								
Intermediate ($HF+HO_2$)	215.2	275.3	526.9	601.1	743.5	1252.7	1482.9	3442.1	3561.2*i*
Intermediate ($HF+DO_2$)	208.4	269.6	388.7	599.6	743.0	1098.6	1256.4	2514.9	3548.7*i*
Intermediate ($DF+HO_2$)	214.4	262.7	435.1	529.3	554.3	1252.6	1480.2	2573.0	3456.4*i*
Intermediate ($DF+DO_2$)	207.8	257.7	388.6	435.9	552.9	1095.1	1256.4	2505.5	2584.0*i*
TS2($HF+HO_2$)	657.6	744.8	1103.6	1120.8	1292.3	1654.0	1852.9	2164.8	1403.7*i*
TS2($HF+DO_2$)	656.0	743.6	809.2	1112.9	1279.5	1395.2	1437.9	2036.0	1184.3*i*
TS2($DF+HO_2$)	656.0	743.6	809.7	1112.3	1279.5	1394.0	1438.5	2037.6	1183.9*i*
TS2($DF+DO_2$)	654.1	742.5	796.8	822.8	1168.1	1316.3	1333.1	1542.5	1007.0*i*

Table C.2 Harmonic Frequncies of HO_2+HCl systems determined from the M11/cc-pVQZ stationary point structure.

HCl	2877.0								
DCl	2063.4								
Intermediate ($HCl+HO_2$)	152.9	214.2	379.9	423.8	487.6	1247.6	1464.1	2657.0	3438.4
Intermediate ($HCl+DO_2$)	150.8	205.4	311.0	380.6	486.5	1083.4	1250.9	2499.0	2662.3
Intermediate ($DCl+HO_2$)	151.9	202.4	276.5	368.9	423.7	1247.4	1463.2	1907.0	3437.6
Intermediate ($DCl+DO_2$)	149.9	195.2	274.8	313.1	365.6	1082.6	1250.8	1906.2	2504.0
TS1($HCl+HO_2$)	153.1	294.1	371.9	1059.2	1216.6	1427.5	1683.0	3658.4	1120.2*i*
TS1($HCl+DO_2$)	146.6	279.8	295.5	1017.4	1060.6	1262.4	1679.8	2666.2	1118.4*i*
TS1($DCl+HO_2$)	137.2	275.8	348.5	620.6	816.1	1119.8	1410.8	3627.8	1369.1*i*
TS1($DCl+DO_2$)	144.5	275.8	287.1	876.5	970.6	1078.4	1298.7	2665.0	835.9*i*
TS2($HCl+HO_2$)	428.1	851.4	889.7	1026.2	1326.1	1599.3	1790.1	2069.9	503.5*i*
TS2($HCl+DO_2$)	425.1	661.6	844.8	962.8	1276.0	1327.3	1500.2	1938.1	433.9*i*
TS2($DCl+HO_2$)	425.1	662.3	844.9	961.7	1276.1	1327.3	1499.9	1937.8	434.0*i*
TS2($DCl+DO_2$)	421.5	611.3	759.3	823.9	1136.1	1290.5	1329.3	1498.7	385.1*i*

Table C.3 Harmonic Frequncies of HO_2+HBr systems determined from the M11/cc-pVQZ-PP stationary point structure.

HBr	2545.4								
DBr	1811.9								
Intermediate (HBr+HO_2)	119.2	197.1	346.0	405.6	462.6	1247.5	1458.8	2337.3	3426.5
Intermediate (HBr+DO_2)	117.7	188.1	292.5	352.9	460.9	1079.8	1250.7	2333.2	2499.8
Intermediate (DBr+HO_2)	118.7	185.3	252.5	350.9	403.7	1247.1	1457.6	1665.6	3425.9
Intermediate (DBr+DO_2)	117.3	178.2	248.8	301.1	347.0	1079.4	1250.3	1664.4	2495.5
TS1(HBR+HO)	139.6	297.5	350.1	821.8	1099.3	1144.4	1415.3	3628.2	1867.6*i*
TS1(HBR+DO_2)	133.9	257.1	303.9	820.7	1019.8	1126.6	1148.8	2643.4	1866.7*i*
TS1(DBr+HO_2)	137.2	275.8	348.5	620.6	816.1	1119.8	1410.8	3627.8	1369.1*i*
TS1(DBr+DO_2)	131.8	255.3	282.5	619.6	810.4	1048.4	1123.1	2642.8	1367.9*i*
TS2(HBr+HO_2)	337.8	776.3	994.7	1062.6	1331.2	1574.4	1780.7	2105.8	126.2*i*
TS2(HBr+DO_2)	334.6	611.7	920.4	950.3	1264.3	1331.1	1518.9	1961.6	113.3*i*
TS2(DBr+HO_2)	334.8	610.1	923.1	954.5	1261.9	1331.3	1520.0	1952.1	113.3*i*
TS2(DBr+DO_2)	331.0	556.4	737.5	915.7	1116.1	1281.8	1332.4	1529.3	103.6*i*

Table C.4 Harmonic Frequncies of HO_2+HI systems determined from the M11/cc-pVQZ-PP stationary point structure.

HI	2269.7								
DI	1611.8								
Intermediate (HI+HO_2)	98.1	170.9	249.6	333.1	344.2	1241.5	1445.0	2150.6	3442.9
Intermediate (HI+DO_2)	96.9	163.5	237.6	265.2	331.0	1069.4	1245.4	2149.7	2508.6
Intermediate (DI+HO_2)	97.9	153.7	183.9	262.4	343.3	1241.1	1443.7	1529.0	3442.6
Intermediate (DI+DO_2)	96.7	149.2	181.7	254.1	257.3	1069.2	1245.0	1527.7	2507.6
C_2v intermediate (HI+HO_2)	235.7	291.6	704.6	961.7	1212.2	1336.2	1532.2	1774.6	2138.1
C_2v intermediate (HI+DO_2)	216.4	288.8	560.3	882.8	1034.7	1260.0	1336.0	1517.2	1981.9
C_2v intermediate (DI+HO_2)	216.4	289.0	560.2	883.1	1035.9	1260.2	1336.0	1517.5	1978.9
C_2v intermediate (DI+DO_2)	201.6	285.0	505.1	714.6	1002.1	1085.4	1275.4	1336.2	1555.0
TS1(HI+HO_2)	122.6	276.7	352.7	570.9	931.4	1166.5	1409.4	3609.6	1536.3*i*
TS1(HI+DO_2)	118.2	228.8	318.1	570.1	929.2	1042.4	1172.1	2629.6	1535.4*i*
TS1(DI+HO_2)	120.1	242.7	339.5	467.6	686.5	1142.5	1408.6	3609.5	1137.2*i*
TS1(DI+DO_2)	116.0	219.5	279.7	467.0	685.4	1040.0	1148.3	2629.3	1136.0*i*
TS2(HI+HO_2)	293.2	495.2	671.4	918.2	1329.0	1492.9	1529.3	2512.6	649.6*i*
TS2(HI+DO_2)	289.6	481.2	519.0	871.5	1148.7	1330.9	1490.5	1849.9	619.8*i*
TS2(DI+HO_2)	284.2	484.6	553.7	809.0	1080.3	1329.0	1512.2	2496.2	486.8*i*
TS2(DI+DO_2)	280.4	471.3	482.6	680.7	1064.4	1148.0	1330.6	1826.7	468.9*i*

C.2 Vibrational Frequencies for HO_2+PA and OH+PA

Table C.5 Harmonic Frequncies of PA+OH Reactants and Products determined from the M11/cc-pVTZ stationary point structures.

OH	3767.36							
H2O	1600.51	3853.60	3955.13					
CO2	684.26	686.82	1401.86	2439.26				
Pyruvic Tc	100.98	130.19	260.17	397.57	400.14	532.55	613.37	706.68
	743.56	783.18	979.02	1038.68	1171.91	1251.40	1374.91	1415.53
	1443.33	1445.87	1839.00	1893.35	3062.93	3131.92	3188.57	3685.08
pyruvic Tt	55.04	143.46	251.14	380.39	388.40	521.77	598.07	620.69
	744.79	751.80	972.29	1041.44	1153.83	1221.47	1372.59	1413.77
	1447.04	1450.40	1846.65	1868.14	3062.98	3133.90	3186.57	3793.07
P1	109.27	276.86	379.62	404.80	456.64	537.56	612.56	724.72
	765.64	792.83	878.91	1011.02	1192.00	1281.50	1405.76	1466.44
	1688.77	1889.47	3179.12	3306.66	3675.63			
P2	61.41	266.48	371.64	399.02	439.57	526.92	592.31	637.90
	761.58	762.16	870.42	1005.97	1167.17	1249.63	1403.14	1461.14
	1702.68	1843.77	3180.66	3308.08	3794.54			
P3/P4	100.47	470.08	859.01	946.47	1047.41	1337.95	1446.80	1449.02
	1985.70	3053.72	3155.95	3156.85				
P5	67.00	124.64	216.66	255.71	259.40	327.72	395.64	478.47
	511.42	547.17	613.50	635.92	743.73	970.99	1010.32	1032.81
	1115.61	1186.90	1218.33	1295.38	1378.69	1443.53	1455.06	1463.62
	1847.73	3059.34	3132.28	3184.37	3666.85	3816.22		
P6	541.31	554.32	594.66	611.19	821.86	998.73	1162.52	1279.69
	1477.75	1859.76	3839.27	3843.51				
P7	546.28	634.20	1115.60	1232.82	1964.11	3851.47		
P7 (acetic)	78.32	421.03	544.34	592.64	670.78	872.41	998.17	1069.67
	1210.25	1336.29	1404.08	1462.15	1468.11	1858.71	3074.03	3150.32
	3193.13	3799.32						
P8	56.36	192.18	207.93	236.00	318.94	338.72	384.88	432.26
	522.11	570.43	621.81	731.25	780.13	896.79	946.55	1041.20
	1080.99	1157.15	1209.69	1328.53	1339.93	1377.85	1463.76	1472.99
	1874.13	3081.35	3175.85	3195.03	3790.13	3836.33		

Table C.6 Harmonic Frequncies of PA+OH Pre-Reactive Complexes determined from the M11/cc-pVTZ stationary point structures.

PRC1	37.46	86.33	98.94	132.42	144.13	272.74	375.19	408.91
	416.19	514.05	539.49	622.94	688.05	739.64	785.87	985.20
	1040.79	1178.93	1255.00	1376.80	1413.45	1444.09	1446.69	1818.12
	1896.28	3058.80	3127.43	3185.22	3655.33	3707.19		
PRC2	38.48	52.51	87.01	146.00	149.06	270.14	378.93	401.66
	428.95	529.51	545.72	610.89	622.40	746.16	757.76	980.69
	1043.65	1162.42	1228.32	1378.23	1418.83	1448.05	1452.24	1844.48
	1855.75	3059.70	3130.51	3183.84	3626.08	3791.72		
PRC3	55.07	83.69	132.46	143.26	164.57	261.47	268.58	389.57
	399.55	481.98	531.66	624.14	685.56	745.61	798.58	978.05
	1035.77	1178.32	1227.82	1366.13	1403.98	1440.85	1443.25	1834.32
	1870.64	3064.31	3134.10	3189.06	3555.79	3692.17		
PRC4	53.25	65.08	139.91	142.15	188.23	288.94	381.73	400.31
	409.30	529.21	615.62	633.57	707.93	787.04	791.67	974.92
	1042.38	1176.05	1300.86	1379.04	1446.13	1451.15	1456.73	1797.81
	1870.63	3063.02	3133.80	3186.93	3494.94	3582.45		

Table C.7 Harmonic Frequncies of PA+OH Transition States determined from the M11/cc-pVTZ stationary point structures.

TS1	25.85	90.62	134.44	245.07	292.82	329.44	390.94	422.16
	534.83	591.16	680.66	712.62	766.84	826.44	896.59	1013.54
	1044.81	1181.03	1208.63	1254.49	1398.36	1436.90	1490.87	1807.03
	1893.22	3115.01	3208.94	3698.02	3749.90	1533.60*i*		
TS2	23.13	50.54	140.03	234.38	275.61	367.07	374.72	401.38
	524.20	581.45	618.22	702.20	743.89	807.00	903.01	1019.05
	1026.94	1169.35	1197.80	1231.57	1399.79	1431.82	1488.58	1837.95
	1850.05	3109.55	3201.19	3738.61	3791.07	1566.92*i*		
TS3	67.13	94.89	143.64	248.16	292.79	395.60	398.21	459.14
	496.54	584.62	628.88	649.38	744.35	869.45	978.64	1016.18
	1153.41	1307.99	1360.26	1435.16	1438.82	1485.48	1505.36	1739.70
	1873.17	3069.72	3145.20	3197.04	3828.35	1870.58*i*		
TS4	39.80	108.96	151.05	193.16	331.66	380.68	429.87	493.18
	531.30	574.77	645.03	679.06	742.70	889.87	977.92	1043.14
	1183.92	1377.66	1420.64	1446.53	1448.75	1452.13	1707.89	1724.76
	1876.15	3061.13	3133.02	3185.87	3820.68	1720.18*i*		
TS5	92.10	133.15	199.37	246.34	274.31	310.64	397.00	465.42
	534.49	606.97	629.70	652.36	767.24	945.34	978.47	1038.48
	1157.62	1244.42	1366.77	1403.73	1445.05	1450.07	1549.82	1848.85
	3064.53	3138.17	3189.05	3694.46	3761.67	781.92*i*		
TS6	59.20	119.34	152.60	213.54	280.50	324.76	350.78	386.27
	468.37	534.45	563.76	595.09	683.44	800.65	959.01	1027.96
	1112.32	1159.42	1323.67	1368.57	1443.56	1451.83	1726.89	1904.74
	3073.80	3159.60	3195.80	3765.45	3803.44	1034.71*i*		
TS7	96.93	162.32	187.33	246.39	258.76	308.50	396.36	438.17
	548.33	605.29	721.16	753.74	782.49	905.31	975.50	1017.26
	1160.70	1244.17	1376.51	1397.88	1448.64	1457.14	1560.22	1905.27
	3069.16	3155.17	3192.04	3681.98	3751.95	704.77*i*		
TS8	67.40	175.43	196.94	241.69	278.76	369.18	381.88	412.41
	541.08	583.33	595.41	755.25	774.16	915.03	972.15	1016.88
	1146.11	1224.35	1373.31	1399.18	1448.39	1459.55	1588.24	1863.53
	3070.83	3155.87	3189.27	3742.71	3796.45	709.55*i*		

Table C.8 Harmonic Frequncies of PA+HO_2 Reactants and Products determined from the M11/cc-pVTZ stationary point structures. Any similar products formed from the PA+OH reaction are neglected.

HO2	1247.19	1449.23	3691.67					
H2O2	380.94	1034.80	1349.62	1460.53	3816.78	3818.58		
P3-HO2	70.09	282.28	371.04	411.98	429.30	532.27	587.90	636.75
	745.39	799.83	825.87	921.99	981.56	1163.92	1182.70	1322.61
	1416.62	1453.88	1739.81	1843.82	3171.28	3283.00	3801.39	3858.37
p3b-HO2	84.05	281.70	351.63	410.41	423.67	540.17	558.61	626.96
	738.18	805.87	815.19	887.31	993.46	1143.63	1192.92	1297.89
	1425.33	1445.71	1720.36	1900.19	3167.91	3264.69	3845.65	3854.04
P4/P5-HO2	56.23	519.19	738.22	918.89	969.13	1064.52	1323.49	1330.13
	1368.59	1438.41	1463.64	3022.83	3109.50	3120.68	3804.16	
P6-HO2	169.28	176.54	310.22	354.43	390.17	448.88	584.49	629.74
	720.13	808.25	1006.48	1040.86	1152.63	1218.77	1318.46	1378.70
	1426.28	1468.63	1480.67	2019.57	3069.38	3151.89	3176.27	3843.13

Table C.9 Harmonic Frequncies of PA+HO_2 Transition State Structures determined from the M11/cc-pVTZ stationary point structures.

TS1-HO2	27.33	70.95	84.95	132.93	248.14	276.87	402.07	415.29
	472.32	515.72	535.91	609.08	625.43	705.58	789.67	816.62
	995.55	1016.40	1061.81	1112.54	1187.12	1261.58	1400.56	1415.41
	1440.32	1454.20	1744.23	1892.98	3148.13	3262.10	3692.01	3747.27
	2334.24*i*							
TS2-HO2	39.27	55.40	91.52	154.85	189.41	203.10	248.58	278.01
	320.68	461.80	513.44	575.02	641.36	740.60	816.40	959.86
	1022.84	1129.84	1204.58	1222.94	1352.01	1443.02	1449.24	1471.23
	1577.65	1651.82	1823.82	1953.95	3065.94	3150.71	3187.76	3362.41
	4896.87*i*							
TS3-HO2	47.76	90.46	145.76	192.50	298.21	337.87	446.23	499.31
	536.75	601.35	635.96	653.02	726.37	776.95	832.49	937.17
	1044.57	1171.49	1198.31	1279.25	1290.17	1331.48	1376.08	1468.12
	1483.16	1640.10	1672.87	1826.14	1862.13	3108.15	3249.99	3791.69
	1556.98*i*							
TS4-HO2	29.97	73.95	108.03	188.56	257.49	262.19	368.57	455.77
	550.84	597.41	637.02	673.45	713.91	810.46	875.49	942.20
	1035.66	1161.03	1185.97	1301.79	1333.93	1373.96	1399.47	1441.95
	1491.04	1520.24	1646.08	1681.80	1846.22	3109.16	3204.41	3757.48
	1110.95*i*							
TS5-HO2	39.87	40.67	92.07	96.31	119.29	161.26	184.44	199.54
	255.30	293.07	532.70	550.13	587.26	680.85	851.50	932.89
	1075.28	1113.69	1322.15	1345.42	1352.39	1403.05	1435.30	1473.64
	1500.64	1535.55	2329.71	3032.86	3106.33	3138.31	3363.49	3465.34
	210.40*i*							
TS6-HO2	47.90	96.54	142.47	161.87	184.95	238.36	308.24	351.61
	381.67	492.19	612.93	742.49	763.11	857.15	902.83	999.38
	1046.01	1205.92	1332.40	1377.40	1389.61	1438.58	1468.63	1494.39
	1525.71	1605.46	1876.66	3037.70	3065.45	3141.80	3192.27	3301.75
	174.68*i*							